

**Fast Timing with $\text{LaBr}_3(\text{Ce})$ Scintillators
and the
Mirror Symmetric Centroid Difference Method**

Inaugural-Dissertation
zur
Erlangung des Doktorgrades
der Mathematisch-Naturwissenschaftlichen Fakultät
der Universität zu Köln

vorgelegt von
Jean-Marc Régis
aus Metz, Frankreich

Köln 2011

Gutachter:

Prof. Dr. Jan Jolie
Priv.-Doz. Dr. Alfred Dewald
Prof. Dr. Patrick H. Regan

Tag der mündlichen Prüfung:

16. Mai 2011

Zusammenfassung

Die Messung und Bestimmung der mittleren Lebensdauer eines angeregten Kernzustandes, bzw. eines radioaktiven Isotops, ist von grundlegender Bedeutung für die Untersuchung der Kernstruktur. Diese Arbeit beschäftigt sich eingehend mit der vor mehr als 50 Jahren entwickelten elektronischen “Methode der verzögerten Koinzidenz” (engl.: the fast timing technique). Diese Methode erfährt eine Renaissance aufgrund der rasanten Entwicklung von neuen szintillierenden (fluoreszierenden) Materialien im letzten Jahrzehnt. Szintillator-Detektoren haben eine um zwei bis drei Größenordnungen bessere Zeitauflösung als die weit verbreiteten Halbleiter-Detektoren für hochauflösende Energie-Messungen.

Nach einer kurzen Einführung, auch mit historischem Hintergrund, wird im 2. Kapitel die theoretische Grundlage der elektronischen Lebensdauerermessung aufgearbeitet. Dabei wird insbesondere auf die verwendeten typischen Komponenten eines “fast timing setups” eingegangen. Die hervorragende, ja revolutionierende Eigenschaft des mit Cer versetzten ultraschnellen Lanthan-Tribromid [LaBr₃(Ce)] Szintillators ist die sehr gute Energieauflösung von 2%-4% für γ -Strahlen mit Energien größer als 300 keV. Ein wichtiger Beitrag zum Verständnis der *fast timing technique* wird im Abschnitt 2.3 geliefert. Dieser befasst sich mit der Arbeitsweise des als Zeitmarker genutzten Constant Fraction Discriminators (CFD), wobei eine energieabhängige Funktion des “CFD Zeitstempels” erstmalig hergeleitet wird.

Die bekannten Verfahren zur Analyse der erhaltenen Zeitverteilungen werden im 3. Kapitel besprochen. Wichtig ist die “Centroid Shift” Methode (Verschiebung des Schwerpunktes einer Zeitverteilung), die auf Zeitdifferenzen im Pikosekunden Bereich empfindlich ist. Hierzu ist die adäquate Eichung der Zeitantwort des elektronischen Aufbaus, der oft genannten “prompten Kurve” von größter Bedeutung. Im Idealfall sollte die prompte Kurve mit dem energieabhängigen CFD-Zeitstempel übereinstimmen. In diesem Kapitel wird auch die von mir im Rahmen dieser Arbeit entwickelte und mit der Centroid Shift Methode verträgliche *Mirror Symmetric Centroid Difference Method*, die MSCD Methode, überarbeitet.

Im 4. Kapitel werden die theoretischen Vorhersagen aus den vorausgehenden Kapiteln überprüft. Mit Hilfe von Standardquellen für γ -Strahlung und der Methode der verzögerten $\gamma\gamma$ -Koinzidenzen werden die Theorien erfolgreich bestätigt und eine vollständige Charakterisierung des LaBr₃(Ce) Szintillator-Detektors geliefert. Es wird gezeigt, daß die MSCD Methode eben aufgrund der zwingenden Spiegelsymmetrie des kombinierten Zeitverhaltens empfindlicher ist als die Centroid Shift Methode im Bezug auf einen Detektor. Es wird auch erstmalig gezeigt, dass das Zeitverhalten eines Aufbaus für fast timing mit Szintillatoren mit dem Zeitverhalten des CFD übereinstimmt. Neben der Einführung einer zuverlässigen Prozedur zur Eichung der linear kombinierten $\gamma\gamma$ Zeitantwort, die “Prompt Response Difference”, wird insbesondere auch auf mögliche systematische Fehler hingewiesen. Es wird ebenfalls ein Verfahren zur Unter-

grundkorrektur für die MSCD Methode vorgestellt. Der letzte Abschnitt dieses Kapitels diskutiert mit Hilfe unterschiedlicher Kernmodelle die neuen Ergebnisse von unbekanntem Lebensdauern in den schweren ^{214}Po und ^{214}Bi Isotopen, die in zuvor vorgestellten unterschiedlichen Experimenten mehrmals innerhalb des Fehlers von lediglich 5-10 ps übereinstimmend gemessen wurden. Die in früheren Veröffentlichungen formulierten Vermutungen bezüglich der Kernstruktur dieser Isotope werden durch die neuen Ergebnisse bekräftigt.

Die MSCD Methode wurde auch äußerst erfolgreich in einem sogenannten "in-beam" Experiment angewendet. Hierbei wird der zu untersuchende angeregte Kern über eine Kernreaktion mit Hilfe von Ionen-Strahlen erzeugt. Die akkuraten Ergebnisse der Lebensdauerbestimmung der ersten vier angeregten Zustände in der Grundzustandsbande des deformierten gerade-gerade Kerns ^{176}W werden in Kapitel 5 vorgestellt. Das Besondere an diesem Experiment ist die Verwendung von aktiver Unterdrückung des γ -Strahlen-Untergrundes. Es wird erstmalig der Ursprung des Untergrundes mit Hilfe der präzisen Zeitinformationen identifiziert. Die Ergebnisse der Lebensdauern werden für eine theoretische Analyse der Kernstruktur von ^{176}W verwendet. Zusätzlich wird das Rotor-ähnliche Verhalten von ^{176}W mit seinen benachbarten gerade-gerade Wolfram-Isotopen im Rahmen einer IBA-Rechnung (Interacting Boson Approximation) verglichen. Diese Ergebnisse wiederum werden mit neuen akkuraten Daten für die gerade-gerade Hf- und Os-Isotopenreihen um die Neutronenzahl $N=104$ in der Schalenmitte in Bezug auf Formphasenübergänge verglichen. Dabei zeichnet sich eine mögliche veränderliche Unterschalen-Struktur ab, so wie sie auch in schweren, ungeraden Isotopen beobachtet wird.

Im abschliessenden 6. Kapitel werden die für die experimentelle Kernphysik wichtigen und neuen Erkenntnisse über das fast timing zusammengefasst sowie eine äußerst positive Aussicht für Pikosekunden Lebensdauerermessungen am Institut für Kernphysik der Universität zu Köln erstellt.

Abstract

The measurement and determination of the lifetime of an excited state, or a radioactive isotope, respectively, is fundamental for the analysis of nuclear structure. This work is dedicated to the electronic “delayed coincidence technique” introduced in the 1950s, which is often called the *fast timing technique*. This technique practices a renaissance as a result of the rapid progress in the development of new scintillation (fluorescent) materials during the last decade. The time resolution of scintillator detectors is two to three orders of magnitude better than the widely used semi-conductor detectors for high-resolution energy spectroscopy.

After an introduction with historical background, the theoretical basis of the electronic lifetime measurement is reviewed in Chapter 2. This includes descriptions of the typical components of a fast timing setup. The exceptional property of the Cerium doped Lanthanum-Tribromide $\text{LaBr}_3(\text{Ce})$ scintillators is the very good energy resolution of 2%-4% for γ -ray energies larger than 300 keV. An important contribution for the understanding of the fast timing technique is given in Section 2.3. Therein, the timing principle of the constant fraction discriminator (CFD) is discussed, and an energy dependent function of the CFD time marker is derived for the first time.

The known methods to analyze the experimentally obtained time distributions are reviewed in Chapter 3. The use of the centroid shift method is sensitive to time difference measurements in the few picosecond region. Most important for this method is the accurate calibration of the time response of the electronics setup which is often called the “prompt curve”. In the ideal case, the prompt curve is defined by the energy dependent CFD time marker. Within this work, the *mirror symmetric centroid difference* (MSCD) method was developed as an extension of the centroid shift method. This MSCD method is discussed in detail also in this Chapter 3.

In Chapter 4, the theoretical predictions made in the previous chapters are verified experimentally. Using standard γ -ray sources and the γ - γ fast timing technique, the theories are successfully confirmed and a complete characterization of the $\text{LaBr}_3(\text{Ce})$ scintillation detector is presented. It is shown that the MSCD method is more sensitive than the centroid shift method due to imperative mirror symmetry of the method. Also, it is shown for the first time that the time response of a standard fast timing setup is defined by the CFD timing principle. Beside the introduction of a highly reliable and accurate procedure to calibrate the linearly combined time response of the whole setup, the “prompt response difference”, attention is paid to possible systematic errors. The background correction procedure of the MSCD method is also presented. In different experiments, lifetimes of certain nuclear excited states were measured consistently within an error of only 5-10 ps. The results are discussed in the last Section of this Chapter using different nuclear models. The new results on the heavy ^{214}Po and ^{214}Bi confirm previously published assumptions on their nuclear structure.

The MSCD method is also successful in so-called “in-beam” experiments, where the excited nucleus of interest is created by a nuclear reaction using ion

beams. In Chapter 5, the precise results of the previously unknown lifetimes of the lowest four states of the ground-state band of the deformed even-even isotope ^{176}W are presented. The particularity of this experiment is the use of active background suppression. For the first time, the origin of the background in γ -ray spectroscopy has been identified due to precise timing information. The lifetime results are used for nuclear structure analysis of the ^{176}W isotope. In addition, the rotor like behavior of the ^{176}W isotope is compared with neighboring even-even tungsten isotopes and to predictions from calculations performed using different limits of the Interacting Boson Approximation (IBA). These results are then compared to new and refreshed accurate data of the even-even Hf and Os isotopic chains around the neutron number $N=104$ at mid-shell with regard on nuclear shape phase transitions. A change in sub-shell structure seems to become apparent, similar to observations in heavy odd-mass nuclei.

In Chapter 6, the important new findings on fast timing for nuclear experimental physics are summarized and finally, a positive outlook is posed for picosecond lifetime measurements at the Institute of Nuclear Physics of the Cologne University.

Contents

1	Introduction	8
2	On the fast timing technique	11
2.1	Scintillators	13
2.2	Photomultiplier tubes (PMT)	15
2.3	The constant fraction discriminator (CFD)	16
3	Analysis of time distributions	21
3.1	The centroid shift method	21
3.2	The prompt curve in γ - γ timing experiments	23
3.3	The mirror symmetric centroid difference method	26
4	The LaBr₃(Ce) detector characteristics	31
4.1	Non-linearity and resolution	31
4.2	Time-walk analysis using γ -ray sources	35
4.3	The PRD calibration procedure	42
4.4	The dynode timing with the XP20D0 PMT	54
4.5	Time-walk using different timing conditions	59
4.6	The first excited state in ²¹⁴ Po and ²¹⁴ Bi	62
5	Lifetime measurements in W and Hf isotopes	65
5.1	Nuclear structure considerations	65
5.2	γ - γ fast timing on ¹⁷⁶ W using the MSCD method	72
5.2.1	Experimental setup and results	72
5.2.2	The lifetimes of the yrast-states in ¹⁷⁶ W	81
5.3	The lifetime of the 2 ₁ ⁺ state in ¹⁷² Hf	83
5.4	<i>B(E2)</i> systematics in the W and Hf isotopic chains	87
6	Conclusions and outlook	93
A	The background correction procedure of the MSCD method	96

Chapter 1

Introduction

For nuclear structure studies, the knowledge of the lifetime of a nuclear excited state is essential. The obtained transition probability, the reciprocal of the lifetime, gives information on the collectivity of the decaying excited state and shows the enhancement or hindrance of the decay in the evolution of nuclear structure with variable number of valence nucleons. These observables are related to the quantum numbers of the states involved. The quantum numbers in turn are used as labels for the basis of the Hilbert space or for irreducible representations of dynamical group structures to generate a model dependent energy spectrum as well as selection rules for nuclear transitions and their strengths. A comparison of the theoretically derived transition probability with the measured one allows to test the nuclear structure models. Different techniques for lifetime determination have been established to cover a wide range of nuclear lifetimes (10^{-15} - 10^{15} s). The electronic lifetime measurement is the only method to access lifetimes in the range of 10^{-9} - 10^{-3} s. Using very fast scintillator detectors, even lifetimes down to the few picosecond region can be determined. The method of the electronic lifetime determination is often called the “*fast timing technique*”.

The use of scintillators for experimental nuclear physics dates back to 1903, where W. Crookes invented the *Spinthariscopes* [1] (from the Greek word scintillation). This instrument consists of a zinc sulfide (ZnS) coated screen at the end of a brass tube with a tiny amount of radium salt at about a millimeter in front of it and a lens or a microscope at the other end. By the eye, one can observe individual light flashes (scintillations) on the screen caused by the incident alpha particles. Bringing the radium nearer to the screen the scintillations become more numerous and brighter indicating higher radioactive intensity and higher energy deposition; important observations at that time. In combination with the human eye, the Spinthariscopes were even used as the first scintillation counter to measure the radioactive decay probability.

Briefly after the multi-stage electrostatic photomultiplier tube (PMT) was commercially introduced, the scintillator and PMT detector assembly as used today was invented by S. Curren in 1944 [2]. PMTs absorb the light emitted by the scintillator and re-emit it in the form of electrons via the photoelectric effect. The subsequent multiplication of the photoelectrons results in an electrical

pulse which can then be analyzed electronically. This invention quickly led to important applications, as the time-of-flight (TOF) mass spectrometer [3] or the nowadays world wide established positron emission tomography (PET) for oncological diagnostics [4].

For measurements of nuclear lifetimes, E. R. Bell developed an electronic timing circuitry in 1955. The principle is to measure the time difference between two time correlated events and is called the *delayed coincidence technique* [5, 6]. Already in 1947, R. Hofstadter invented the heavy thallium activated sodium iodide scintillator, NaI(Tl), which made it possible to use γ -rays for the measurement of nuclear lifetimes [7]. However, the use of NaI(Tl) is limited by its energy resolution of about 7% and resulting bad peak-to-background ratio [8]. The fastest scintillators of those days were organic scintillators with time resolution better than 10^{-10} s. But due to relatively bad energy resolution of 10-20%, the electronic nuclear lifetime determination was only successful using particle detection, as the α - e^- [9] and the β - e^- [10] fast timing techniques (e^- being the conversion electron emitted from the atom as a nuclear transition process). In the early 1960s and later, the scintillator detector assemblies were replaced by semi-conductor detectors for high resolution γ -ray spectroscopy [11]. However, the time resolution of semi-conductor detectors is worse by two to three orders of magnitude, therefore fast timing with semi-conductor detectors is an accurate technique for lifetime determination down to the few nanosecond region.

In the mean time, the development of new scintillation materials was pushed by the objective of improving both the time and the energy resolution. In the 1980s the ultra fast BaF₂ scintillator was introduced, the fastest inorganic scintillator available until now. This scintillator allowed H. Mach et al. to introduce a picosecond *ultra fast timing technique* also known as the *advanced time delay (ATD)*¹ method in 1989 [12]. The method takes advantage of the high resolution Ge-detectors to select a γ -ray of the decay path (cascade) of the interest which is used as a trigger to clean the BaF₂ γ -ray spectrum, whilst the nuclear lifetime is measured via β - γ -coincidences. The γ -decay lifetime is obtained using the γ -gated BaF₂ scintillator in combination with a thin plastic scintillator detector providing uniform timing with β s. Fundamental works [12, 13] and important observations [14] have made the ATD method the nowadays best established picosecond application for the fast timing technique.

The scientific development during the last decade has brought forth many kinds of heavily doped inorganic scintillators. For the LaBr₃(Ce) scintillator invented in 2001 [15], an increase in cerium doping is equivalent to an increase in energy and time resolution [16]. The timing property is equivalent to very fast plastic scintillators, while the energy resolution could be improved drastically to about 3% [17] which also improves remarkably the peak to background ratio. This enabled the introduction of a new picosecond γ - γ fast timing technique in 2010 by myself. The *mirror symmetric centroid difference* (MSCD) method [18] takes advantage of the symmetry obtained when performing γ - γ lifetime measurements using a pair of almost identical very fast scintillator detectors. In contrary to the

¹also called “the β - γ - γ timing technique”

ATD method, each detector then reproduce the lifetime of a nuclear excited state. The *centroid difference* of the obtained two time distributions is mirror symmetric with respect to the energy difference of the two participating γ -rays. This allows for precise calibration of the combined γ - γ time-walk characteristics of the setup. The energy dependent *prompt response difference* (PRD) describing the time-walk characteristics was already measured precisely with an accuracy of only 4-8 ps ($\propto 2\Delta\tau$) [18]. Therefore, the MSCD method in application with very fast scintillators allows for precise lifetime determination down to the few picosecond region.

The aim of this work is to fully characterize the properties of the LaBr₃(Ce) scintillator detector and to investigate the time-walk characteristics with respect to the reliability of the recently reported calibration function. Also, the author would like to emphasize the newly developed and very attractive MSCD method which was used to analyze the mass of data recorded for this work. The main issue is to introduce a highly precise and reliable procedure to calibrate the energy dependent timing response of the setup which is described by the PRD curve. Additionally, the results of in-beam and off-beam measurements of unknown lifetimes are reported. The precise lifetimes are used for nuclear structure analysis using different theoretical models.

Chapter 2

On the fast timing technique

As illustrated in Fig. 2.1, the principle of the delayed coincidence technique is to measure the time difference between two coincident, i.e. time correlated electronic signals. For measurements of nuclear excited states, a reference timing signal indicating the moment of formation of the nuclear excited state is needed. This reference “start” timing signal can be provided by a nuclear transition feeding directly the state of the interest [18, 19], but also by nuclear decay products [9, 10, 20] or by a signal synchronized with the radio frequency of a pulsed beam [21]. The second “stop” signal is obtained from the decay of the state of interest.

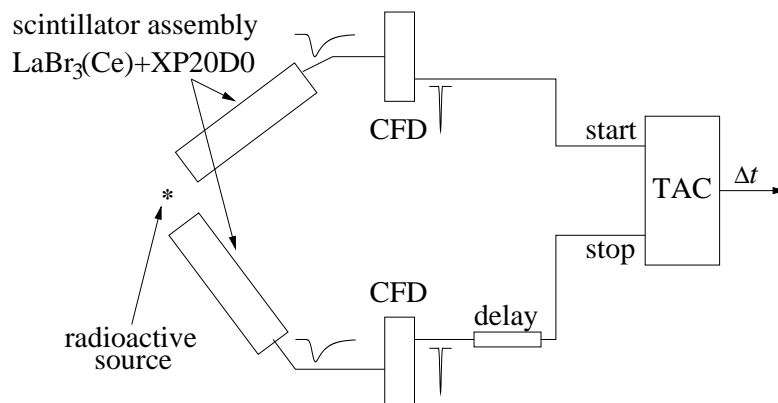


Figure 2.1: Schematic drawing of the fast timing setup used in this work (the delayed coincidence circuitry); figure from Ref. [18]. XP20D0: 8-stage photomultiplier tube from the Photonis company, CFD: constant fraction discriminator, TAC: time to amplitude converter.

For the purpose of investigating the overall timing properties of a standard fast timing setup (Fig. 2.1), the intrinsic timing characteristics of each individual timing branch has to be measured. The scintillator detector assembly used for this work consists of a cylindrically shaped $\text{Ø}1.5'' \times 1.5''$ $\text{LaBr}_3(\text{Ce})$ scintillator with about 5% cerium doping¹ in conjunction with the XP20D0 photomultiplier tube

¹as specified by the manufacturer Saint-Gobain

(PMT). As shown in Fig. 2.1, the PMT anode signal from the scintillator detector assembly is directly connected to the input of a constant fraction discriminator (CFD). The main property of the CFD is to minimize the timing uncertainty due to statistical amplitude variations of the input signal (explained in Section 2.3). The time to amplitude converter (TAC) output amplitude is proportional to the time difference between the two CFD fast timing signals coupled directly at the start and delayed at the stop inputs. A standard slow energy coincidence circuit completes the setup to record triple events $(E_1, E_2, \Delta t_{12})$ within a coincidence time window of about 100 ns.

The intrinsic time resolution of the setup can be measured using real prompt (simultaneously occurring) events or using prompt decay transitions. For fast timing setups, a prompt decay is associated with lifetimes $\tau \leq 1$ ps. The obtained prompt response function (PRF) is a Gaussian distribution and its FWHM gives a rough estimate of the time resolution. In the ideal case of no feeding and no background contributions, time distributions of directly measurable lifetimes show the typical asymmetric shape of a convolution of the PRF $P(t)$ with an exponential decay:

$$D(t) = n\lambda \int_{-\infty}^t P(x)e^{-\lambda(t-x)}dx \quad \text{with} \quad \lambda = 1/\tau, \quad (2.1)$$

where n is the normalization factor. Time distributions of lifetimes which are longer than the FWHM of the corresponding PRF have a pronounced decay slope and the lifetime τ can be determined directly using the slope or the deconvolution method according to Eq. (2.1) [12, 19, 22].

The FWHM of prompt events includes all timing uncertainties (time jitter σ) obtained from the scintillator due to the processes of scintillation light collection and conversion at the photocathode of the PMT, the electronics comprising the PMTs and the CFDs of both timing branches and possible uncertainties due to the setup geometry, e.g. when using an extended γ -ray source. L. G. Hyman et al. developed in 1964 his theory for the description of the scintillation light shape and resulting time resolution of scintillator plus PMT detector assemblies [23, 24]. The time resolution δt of a fast timing branch is expressed by the Hyman function which describes a normalized time resolution [23]:

$$\delta t \propto H(\text{PMT}, f) = k\sqrt{\frac{\tau}{N_{\text{phe}}}}, \quad (2.2)$$

where τ is the scintillator decay time (see Section 2.1) which defines the scintillation light pulse shape and N_{phe} is the number of photoelectrons obtained after conversion of the scintillation light. k is a constant dependent on PMT properties and the fraction f of the detector response pulse height which is used for CFD operation. These parameters are discussed in the following Sections. Assuming a point source in a γ - γ timing experiment, the time resolution of a fast timing branch related to the FWHM of the PRF and corresponding to a 2σ deviation can be written as

$$\delta t = \frac{\text{FWHM}}{\sqrt{2}} \approx \sqrt{\sigma_{\text{Sc.}}^2 + \sigma_{\text{PMT}}^2 + \sigma_{\text{CFD}}^2}. \quad (2.3)$$

2.1 Scintillators

The most important contribution to the time resolution of a fast timing setup [(Eq. (2.3))] is due to the nature of the scintillator, which can be classified in two main categories, namely the organic and inorganic scintillators. Also, the crystal size contributes to the time resolution, because of the interaction point vs. scintillation light collection time corresponding to 33 ps per cm [12, 13] (see also Fig. 2.2). Organic scintillators are made of aromatic hydrocarbons in crystalline shape or as a solvent in liquids or in matrices of amorphous polymers (plastics and glasses). Due to low Z -material (Z being the atomic number), organic scintillators are predominantly used for particle detection, as in elementary particle physics (high energy physics [25]) and also in nuclear structure physics (e.g. lifetime measurements using conversion electrons [19, 21]). For γ -ray spectroscopy, the inorganic halide scintillators with higher density ρ and high Z are the better choice due to Z^5 and ρ dependency of the photoelectric effect [26]. In Table 2.1, the main properties of different organic and inorganic scintillators are compared.

Table 2.1: Properties of commonly used scintillators. τ_f is the decay time of the fast component of the scintillation light pulse. The light yield is expressed by the number of fast scintillation photons created per energy deposited in the scintillator material. The essential for the time resolution is the figure of merit η of Eq. (2.4) given in arbitrary units. The value of the energy resolution ΔE corresponds to the FWHM of the 662 keV full energy peak (^{137}Ba γ -line). The values for the $\text{LaBr}_3(\text{Ce})$ scintillator are given for Ce^{3+} concentrations $\geq 0.2\%$ [27].

scintillator	type	τ_f [ns]	light yield [N_f/MeV]	η [a.u.]	$\Delta E/E$ [%]
anthracen	org. crystal	30	8000	1.94	15
p-terphenyl	liquid org., plastics	1-5	2000-4000	0.5-1.6	10-20
NaI(Tl)	inorg. crystal	230	38000	2.5	7
BaF ₂	inorg. crystal	0.8	2000	0.6	10
LaBr ₃ (Ce)	inorg. crystal	15-26	45000-61000	0.5-0.8	3

An important factor for the time resolution is the decay time τ (lifetime) of the excited states in the crystal which decay by the emission of scintillation light. For most scintillators, the light pulse shape can be described as a convolution of a Gaussian with two exponential decays corresponding to a fast and a slow component τ_f and τ_s of the crystal relaxation [23]. In organic scintillators

molecular singlet states are excited by ionizing radiation. The decay to the singlet ground-state is very fast and accompanied by the emission of scintillation light. The lifetime τ_f of such molecular excited singlet states is typically in the low nanosecond region [28]. A slow component (phosphorescence or after-glow with $100 \text{ ns} \lesssim \tau_s \lesssim 1 \text{ ms}$) can arise due to triplet state excitations, whose are forbidden to decay to the singlet states. The relaxation in this case is due to triplet-triplet interactions [29]. For inorganic scintillators, the excitations can be described using the electronic band structure of an isolator. Electrons can be excited from the valence band into the conduction band or into the exciton band just below the conduction band. Impurities create electronic levels in the forbidden gap between the valence and the exciton band. The excitons, weakly bound electron-hole pairs, can move freely through the crystal lattice until they reach an impurity center which activates a fast de-excitation of the exciton. The recombination of an electron with a hole is accompanied by the emission of scintillation light. The probability for recombination is strongly increased for higher number of activator centers, hence for higher doping [15]. Holes in the valence band and the associated electrons excited in the conduction band are captured successively by impurity centers exciting certain metastable states not accessible to the excitons. The delayed de-excitation of those metastable impurity states gives rise to a slow decay component of the scintillation light (e.g. $\tau_s=630 \text{ ns}$ for BaF_2 with 79% intensity [30]).

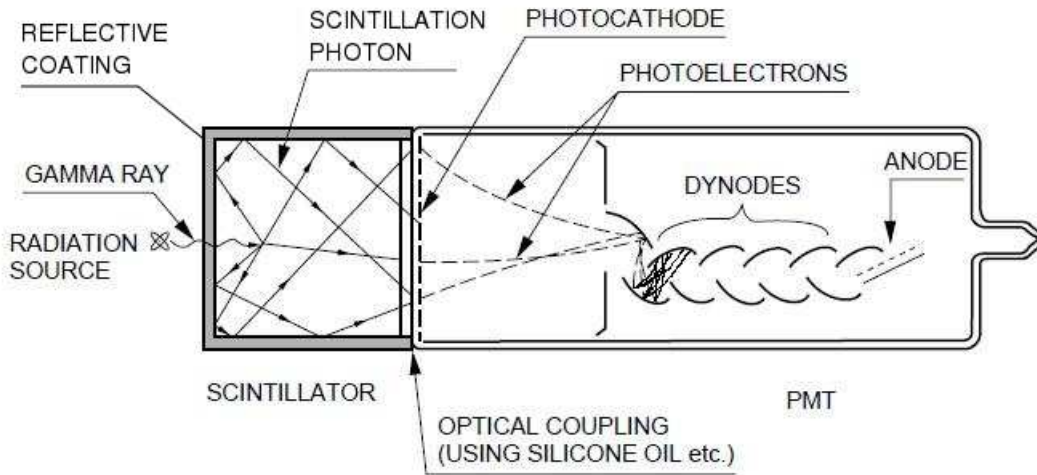


Figure 2.2: Schematic drawing of a typical scintillator and PMT detector assembly and illustration of the detector working principle. The reflective coating on the outer faces of the scintillator is used to minimize losses in scintillation light output. The photocathode and the electrodes including the anode are located inside a vacuum tube. The dynode chain is supplied by a voltage divider [26, 33]. The figure taken from Ref. [33] is slightly modified.

The $\text{LaBr}_3(\text{Ce})$ crystal is one of the brightest scintillators available. A high scintillation light output is desirable, as the final detector response pulse height is directly related to the detected number of fast scintillation photons N_f and

the statistical response resolution is proportional to $1/\sqrt{N_f}$. The best energy resolution is also a result of the very low non-proportionality in light yield of about 6% for $60 \text{ keV} < E_\gamma < 1274 \text{ keV}$ [27, 31]. Especially for fast timing with γ -rays, a very good energy resolution is requested. For Ce^{3+} concentrations of 0.2% and more, the scintillation light shape is dominated by the fast component (slow component: $\tau_s = 66 \text{ ns}$) with intensity more than 93% [27]. In reference to the work of M. Conti et al. [32], the scintillator time jitter can be expressed by the figure of merit η :

$$\sigma_{\text{Sc.}} \propto \eta = k' \sqrt{\frac{\tau_f}{N_f}} \quad (2.4)$$

which for the $\text{LaBr}_3(\text{Ce})$ scintillator is comparable with the fastest scintillators available. Following Hymans theory of time resolution according to Eq. (2.2), k' is a constant dependent on PMT properties and the pulse height fraction f .

2.2 Photomultiplier tubes (PMT)

The photomultiplier tube is used to convert the scintillation photons into an appropriate electronic signal which can be used for pulse shape and timing analyzes. A primary photoelectron is generated at the semitransparent photocathode via the photoelectric effect and accelerated toward the dynode chain, which may contain up to 14 elements. Upon impacting the first dynode, a photoelectron will invoke the release of additional secondary electrons that are accelerated toward the next dynode, as illustrated in Fig. 2.2. Due to successive electron multiplication, a gain of 10^5 to 10^8 secondary electrons per photoelectron is obtained dependent on the material and the number of the dynodes and the applied acceleration voltage between them [34]. This makes the detection of even one single scintillation photon possible [35]. The total single photoelectron transit time-spread σ_{SPT} then consists of the time-spread between the photocathode and the first dynode, the transit time-spread in the electron multiplier and that between the electron multiplier and the anode. The most important contribution is due to the photoelectron time-spread in reaching the first dynode [34] and which can be measured using the single photon technique (SPT) described in Ref. [35]. This time-spread is dependent on the geometry of the photocathode and the focusing electrodes. The total transit time-spread resulting from the initial photoelectron velocity distribution is reduced by increasing the voltages between the photocathode and the first dynode and between the next stages of the electron multiplier [34]. On the other hand, a higher gain can drive the PMT into saturation due to space charge effects in between the last dynodes and especially at the anode. This increases the non-linearity of the PMT response which in turn decreases the energy resolution [36]. As a result of statistical processes, the PMT time jitter σ_{PMT} can be considerably reduced for increased photocathode quantum efficiency, increased secondary emission yield and reduced total transit time [34].

For this work, the 8-stage Photonis XP20D0 PMT and the very well known 12-stage XP2020 PMT were used. The photocathode of both PMTs are made of

a semi-transparent $\varnothing 51$ mm bi-alkali metal (Sb-K-Cs) with 20%-25% quantum efficiency at spectral wave lengths of 350-450 nm [37], which fits well with the emission maximum wave length of 380 nm for the $\text{LaBr}_3(\text{Ce})$ scintillator resulting in a quantum efficiency of 23.2% for Ce^{3+} concentration of about 5% [38]. The single photoelectron time-spread of the XP2020 PMT was measured to be about 200 ps [39], which is superior to the decay time of scintillators, while the XP20D0 PMT was reported to provide better timing by factor of 1.2 due to reduced number of dynodes and the application of a screening grid at the anode to reduce space charge effects [17]. Fig. 2.3 shows a scintillation light pulse shape (with $N_{\text{phe}} \gg 1$) obtained from the $\text{LaBr}_3(\text{Ce})$ +XP20D0 detector assembly. The decay time of the used 5% doped $\text{LaBr}_3(\text{Ce})$ scintillator is measured to be $\tau = 17(2)$ ns and virtually no slow component is observed. These results are in agreement with the results reported in Ref. [27]. More important is the detector rise time t_r as it defines the slope of the CFD bipolar pulse at the baseline crossover, which is the essential for the setup time resolution and is investigated in the following.

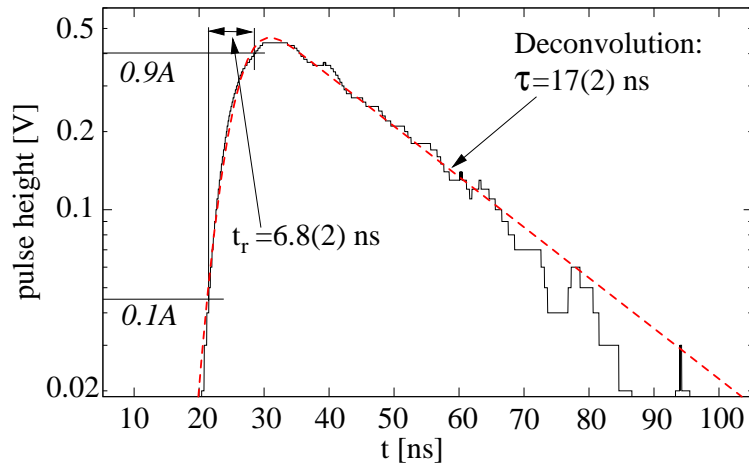


Figure 2.3: Semi-logarithmic plot of the IKP Cologne $\varnothing 1.5'' \times 1.5''$ $\text{LaBr}_3(\text{Ce})$ scintillation light pulse shape which is mainly caused by the decay time of the scintillator. The dashed time curve was obtained by a fit of the detector pulse shape using Eq. (2.1). The inverse of the slope for $t > 45$ ns corresponds to the decay time τ of the tested 5% doped $\text{LaBr}_3(\text{Ce})$ scintillator. The detector rise time t_r is defined as the time the pulse needs to rise from 10% to 90% of the amplitude A [40].

2.3 The constant fraction discriminator (CFD)

The design of the CFD was stimulated by the ability to produce a timing signal which in the ideal case is precisely related in time to the occurrence of an event, regardless of the PMT output pulse height. Indeed, the statistical amplitude

variations ΔA of the PMT output pulse height A and the PMT output signal-to-noise ratio induce a timing uncertainty σ_{CFD} of the CFD time pick-off element. Using the conventional leading-edge timing mode, the threshold crossover will “walk” in time relative to the initiation time t_0 of the input pulse dependent on the input amplitude A , as illustrated in Fig. 2.4. This time-walk is the major source of the CFD time jitter [40]. An additional time-walk contribution is obtained due to the charge sensitivity of the threshold crossover detecting device [40].

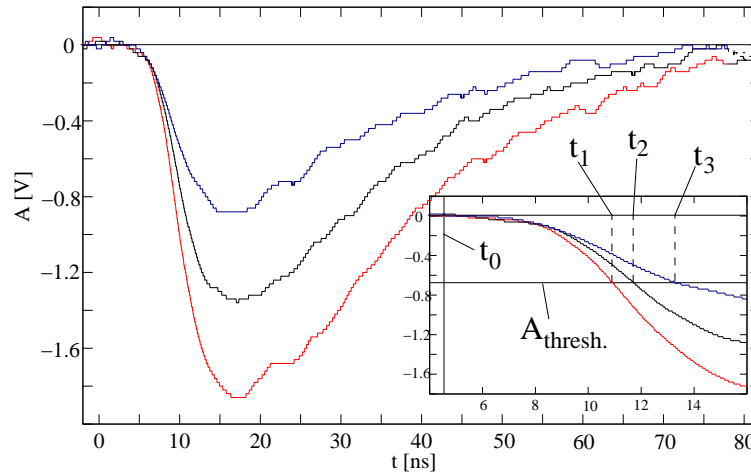


Figure 2.4: XP20D0 anode pulses with different amplitudes obtained in combination with the Cologne $\text{LaBr}_3(\text{Ce})$ scintillator. No significant changes in the detector rise time can be observed. Inset: Illustration of the time-walk obtained when using the leading-edge timing mode with threshold level $A_{\text{thresh.}}$. For pulses with different amplitudes A_i starting at the same time t_0 , the threshold crossover used to trigger a logic timing signal occurs at different times t_i .

In the CFD timing mode, the input signal is delayed by the shaping delay time t_d , and a fraction $f \in [0, 1]$ of the undelayed pulse is subtracted from it to shape a bipolar pulse. By proper selection of $f = A_{\text{thresh.}}/A$ which defines the triggering fraction in leading-edge timing, the time resolution can be minimized. The optimum triggering fraction was analytically derived by L. G. Hyman et al. [24] and measured for the first time in 1963 by A. Schwarzschild [6] to be $f \approx 0.1$. Most commercially available CFDs attenuate the input signal by a constant fraction of $f = 0.2$ for being used to shape the CFD bipolar pulse. As illustrated in Fig. 2.5, the zero crossover of the generated bipolar pulse is detected and used as a trigger to produce the logic CFD output fast timing signal. By proper selection of the shaping delay time t_d , the time-walk due to input amplitude and rise time variations can be minimized [40].

Dependent on the choice of the shaping delay time, two cases in determining the zero crossover time are considered. The true-constant-fraction (TCF) timing mode is given for the condition:

$$t_d > t_r(1 - f) \quad \text{TCF timing} \quad (2.5)$$

with t_r being the detector rise time. The second case to be considered is the amplitude-and-rise-time-compensation (ARC) timing mode:

$$t_d < t_r(1 - f) \quad \text{ARC timing.} \quad (2.6)$$

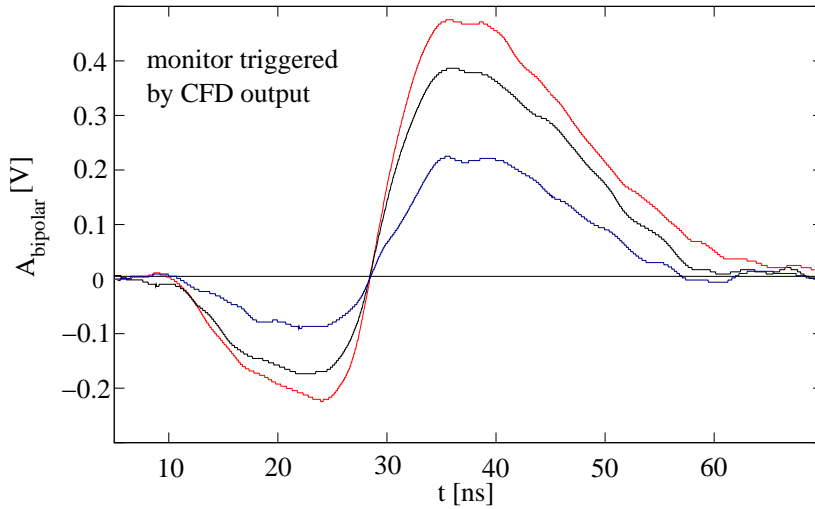


Figure 2.5: Monitoring of the generated CFD bipolar pulse shape obtained using a shaping delay time of $t_d = 16$ ns. The baseline crossover of the bipolar pulse is used to provide the logic CFD output fast timing signal. The zero crossover timing virtually eliminates the leading edge time-walk. Note the amplitude dependent slope of the bipolar pulse at zero crossover.

Assuming ideal signals with linear rise time, the zero crossover time T relative to the input pulse starting time $t_0 = 0$ is [40]

$$T_{\text{TCF}} = t_d + ft_r, \quad T_{\text{ARC}} = \frac{t_d}{1 - f}. \quad (2.7)$$

In ARC timing the fraction of the input pulse height at which the time pick-off is generated is not constant and is described by the effective triggering fraction [40]

$$f_{\text{eff}} = \frac{ft_d}{t_r(1 - f)}, \quad (2.8)$$

which is always less than f , according to Eq. (2.6). For the case of an ideal input signal with linear rise time and assuming an amplitude independent rise time, as is the case for scintillator detectors, the zero crossover is independent of the amplitude for both the TCF and ARC timing [40]. However, the rising of a real detector pulse is not linear, as can be seen in Fig. 2.4. This may have an impact on the triggering fraction or the effective triggering fraction, respectively.

As can be seen in Fig. 2.5, the slope of the generated CFD bipolar pulse at zero crossover is dependent on the input amplitude, regardless of the CFD timing mode. Still assuming an ideal input pulse, the slope at zero crossover for TCF

timing is [40]

$$\left. \frac{dA_{\text{bipol.}}}{dt} \right|_{T_{\text{TCF}}} = \frac{A}{t_r}, \quad (2.9)$$

and for ARC timing [40]:

$$\left. \frac{dA_{\text{bipol.}}}{dt} \right|_{T_{\text{ARC}}} = \frac{A(1-f)}{t_r}. \quad (2.10)$$

The time-walk due to charge sensitivity of the zero crossover comparator is related to the slope of the bipolar signal as it passes through the zero baseline, as illustrated in Fig. 2.6a. Assuming the bipolar pulse to be linear during the time ΔT that is required to accumulate the sensing charge related to the area q , the time-walk due to charge sensitivity can be expressed by

$$\Delta T \cong \sqrt{\frac{2q}{\left. \frac{dA_{\text{bipol.}}}{dt} \right|_T}}, \quad (2.11)$$

following the argumentation made in Ref. [40]. T is the zero crossover time of either the TCF or the ARC timing mode, as defined by Eqs. (2.5-2.7). Considering Eqs. (2.9)-(2.11), for identical input pulses the time-walk ΔT_A and the time-walk induced statistical timing uncertainty $\Delta T_{\Delta A}$ due to charge sensitivity is greater for ARC timing than for TCF timing, as the slope of the ARC bipolar pulse at zero crossing is always less than that of the TCF pulse at zero crossing.

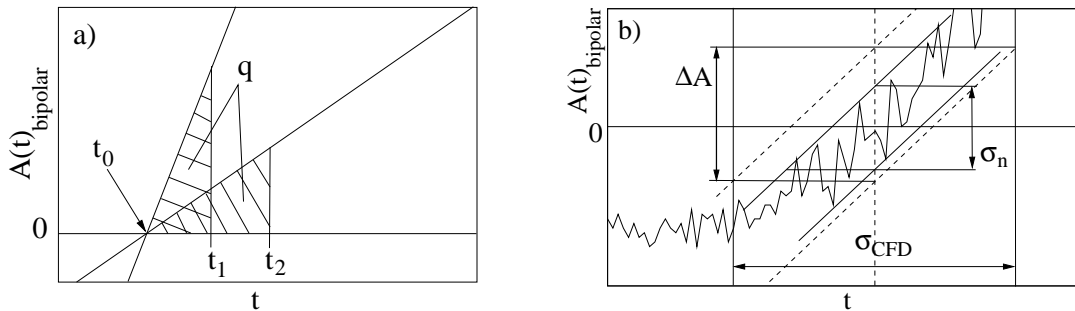


Figure 2.6: a: Amplitude dependent time-walk due to charge sensitivity of the zero crossover comparator. Due to amplitude dependent slope of the bipolar signal at zero crossover, the sensing charge q is collected at times t_i relative to zero crossover t_0 resulting in a time-walk $\Delta T_{A_i} = t_i - t_0$. b: The CFD time jitter, Eq. (2.14), obtained in combination with scintillator detectors is dominated by the jitter due to statistical amplitude variations.

As illustrated in Fig. 2.6b, another source of the CFD timing uncertainty is given by noise that is superimposed on the input signal and that can also be generated by the CFD itself. Assuming uncorrelated noise with root mean square value σ_n , the noise induced uncertainty in the zero crossover timing is given by

[40]

$$\Delta T_n \cong \frac{\sigma_n \sqrt{1 - f^2}}{\left. \frac{dA_{\text{bipol.}}}{dt} \right|_T}. \quad (2.12)$$

As a consequence of the considerations made before, the CFD timing can be described as

$$T_{\text{CFD}} = T + \Delta T_A, \quad (2.13)$$

$$\sigma_{\text{CFD}} = \sqrt{\Delta T_{\Delta A}^2 + \Delta T_n^2}. \quad (2.14)$$

For large amplitudes, the CFD timing is expected to be almost constant. Using very fast scintillator detectors, the CFD time jitter is altered by statistical amplitude variations rather than by noise [41]. With decreasing amplitudes the time-walk due to charge sensitivity increases as well as the CFD time jitter. Using high resolution Ge-detectors with ARC timing, the “slope-to-noise” ratio becomes the essential for the time resolution of the setup [41].

Assuming a linear amplitude versus energy relation, $A \propto E$, and referring to Eqs. (2.9-2.11) and (2.13), the CFD time-walk characteristics is expected to be described by

$$T(E)_{\text{CFD}} = \frac{a}{\sqrt{E + b}} + c \quad (2.15)$$

for either the TCF or the ARC timing mode. a, b and c are free adjusting parameters to be fitted to experimental data. A similar energy dependency is expected for the setup time resolution, according to Eqs. (2.11), (2.12) and (2.14).

To provide energy selectivity and to prevent the time pick-off device from triggering on noise, a leading-edge discriminator is used to arm the zero crossover detection device. In ARC timing, the CFD can produce leading-edge time-walk, if the zero crossover time occurs before the leading-edge of the input pulse reaches the adjustable “CFD threshold” of the arming comparator. Also, the CFD will randomly trigger on noise, if the zero crossover detector is armed before the bipolar pulse begins. As the input pulses from ultra fast detectors have finite pulse widths, the shaping delay time in TCF timing must also be chosen short enough in order to force the zero crossover to occur during the time the attenuated signal is at its peak. To avoid leading-edge time-walk, the CFD threshold should be set as low as possible, e.g. just above the baseline noise.

Chapter 3

Analysis of time distributions

The basis of the nuclear lifetime determination from an experimentally obtained time distribution is that in any case the time distribution $D(t)$ is a convolution of the setup PRF with an exponential decay, as defined by Eq. (2.1). The most straightforward procedure to determine the lifetime is to use the slope method, where the straight line of the decay obtained in a semi-logarithmic plot is fitted and its slope is directly the decay constant λ , hence the inverse of the lifetime τ :

$$\ln[D(t)] \propto -t/\tau \quad \text{the slope method for } \tau > \text{FWHM} \quad (3.1)$$

This method is used for lifetimes which are longer than the FWHM of the PRF, as in this case the long slope provides enough data points to fit the straight line. Also, possible falsification due to prompt contributions as a result of feeding from higher states or due to prompt background contributions can be avoided by fitting the slope outside the region outspreaded by the time distribution of the background. The feeding from higher states can be avoided using as “start” signal nuclear transitions which feed directly the level of the interest. If the background contribution is negligibly small, the deconvolution method provides a more precise result, while the complete time distribution is fitted using Eq. (2.1), as shown in Fig. 2.3 of Chapter 2.2. In γ - γ fast timing experiments, the limit of the deconvolution method is well described by the time resolution $\delta t = \text{FWHM}/\sqrt{2}$, as defined by Eq. (2.3).

3.1 The centroid shift method

For determinations of lifetimes which are smaller than the FWHM of the setup PRF, the centroid shift method is used. Using ultra fast scintillator detectors, the centroid shift method is picosecond sensitive [12, 18]. Analytically, the method was introduced in 1950 by Z. Bay [42]. The centroid, i.e. the first moment of a delayed time distribution $D(t)$ is defined as

$$C(D) = \langle t \rangle = \frac{\int tD(t)dt}{\int D(t)dt} \quad (3.2)$$

with $D(t)$ of Eq. (2.1). The statistical error is given by the variance of $D(t)$:

$$dC = \sqrt{\text{var}[D(t)]} = \sqrt{\langle t^2 \rangle - \langle t \rangle^2}. \quad (3.3)$$

Assuming the ideal case of no feeding and no background contributions, it follows per definition that the centroid (“center of gravity” [42]) of the delayed time distribution is displaced by the mean lifetime from the centroid $C(P)$ of its corresponding PRF:

$$\tau = C(D) - C(P), \quad (3.4)$$

if the decay transition is gated with the stop detector; otherwise: $\tau = C(P) - C(D)$. As explained in Chapter 2.3, the CFD timing is dependent on the amplitude of the detector output pulse. The knowledge on the setup time-walk characteristics, i.e. the energy dependent PRF centroid $C(P)$, is crucial for centroid shift analysis and its accuracy gives the limit of the fast timing technique. Therefore, the time-walk characteristics, often called “the prompt curve”, has to be determined as precise as possible in order to derive the lifetime according to Eq. (3.4).

The prompt curve can be determined by the measurements of prompt events or of precisely known lifetimes at different energies covering a wide dynamic range. Lifetime and background corrections are applied to the data and the prompt curve is calibrated with an accuracy of 2-10 ps [14, 18, 20]. The prompt curve shown in Fig. 3.1 was obtained using real prompt events, namely the promptly generated secondary δ -electrons using an ion beam pulse which hits a thin target [21]. The reference timing signal was provided by a standard NIM¹ signal synchronized with the radio frequency of the pulsed beam. The IKP Cologne orange type electron spectrometer acts as an energy selector and thus provides mono-energetic δ -electrons which is ideal for a measurement of the CFD time-walk characteristics using an ultra fast plastic scintillator plus XP2020 detector assembly. The CFD prompt curve was calibrated empirically using [21]

$$C(E) = \frac{a}{E + b} + c, \quad (3.5)$$

which is a monotonic function of the energy like the physically derived CFD timing given in Eq. (2.15). Note, that the prompt curve is calibrated down to 50 keV which corresponds to an amplitude of only 70 mV slightly above the threshold of the arming comparator set at about 30 mV.

¹abbreviation for Nuclear Instrumentation Modules

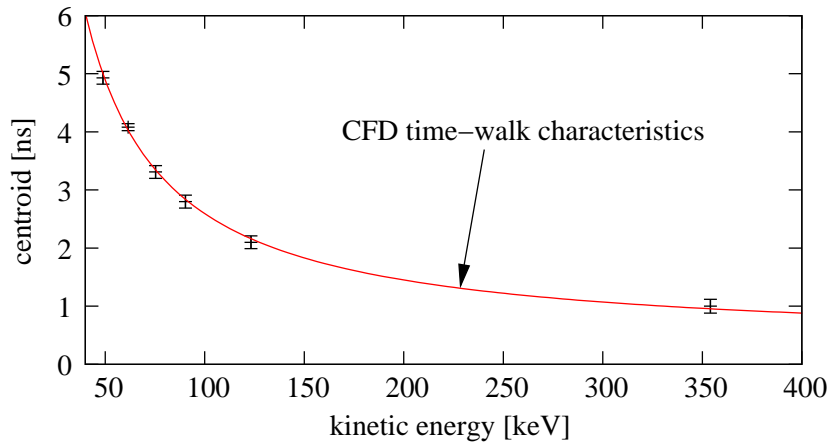


Figure 3.1: The CFD time-walk characteristics (the prompt curve defining $\tau = 0$) obtained using the plastic type NE102 scintillator detector and mono-energetic prompt δ -electrons delivered by the IKP Cologne Orange spectrometer in a pulsed beam experiment [21]. The prompt centroids (data points) are corrected for the energy dependent electron time-of-flight [21]. Note the smooth progression of the prompt centroids especially in the low energy region corresponding to amplitudes of $70 \text{ mV} < A < 200 \text{ mV}$.

3.2 Prompt curve determination in γ - γ timing experiments

To measure the prompt curve in a γ - γ fast timing experiment, a reference timing signal from the experimental system is needed. This is achieved by gating one γ -ray detector constantly on a directly populating or depopulating transition of interest. The other detector selects coincident prompt transitions of different energies to measure its prompt curve. In the off-line analysis, this work has to be made for both γ -ray detectors in order to gain in statistics when performing γ - γ lifetime experiments. The standard ^{152}Eu γ -ray source is ideal to measure the prompt curve according to Eq. (3.4), as it emits many coincident transitions connecting a lot of states with precisely known picosecond lifetimes. As a good example, we consider the 344 keV state in ^{152}Gd (a portion of the level scheme is shown in Fig. 3.2). Seven γ -ray transitions are in coincidence with the 344 keV decay transition, as can be seen in Fig. 3.3. Therefore, the reference energy gate of 344 keV is used to provide the reference timing signal of the setup.

The time spectra of the 344 keV decay transition presented in Fig. 3.4 were obtained without subtracting background contributions of any kind. The energy dependent time resolution and time-walk induced by the CFD is illustrated by the FWHM and the centroids of the time spectra which were determined with a statistical accuracy of only 2-7 ps [18]. The 344 keV gated centroids of coincident transitions were corrected for the known lifetimes and plotted against the γ -ray

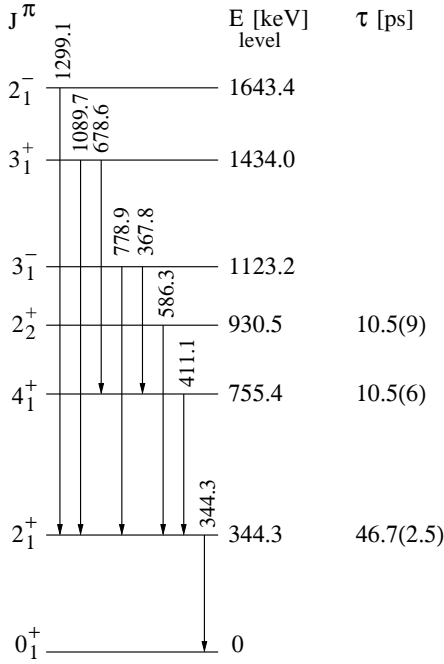


Figure 3.2: Partial level scheme of ^{152}Gd obtained after β^- decay of the standard ^{152}Eu γ -ray source. J^π , E_γ , E_{level} and τ from Ref. [43].

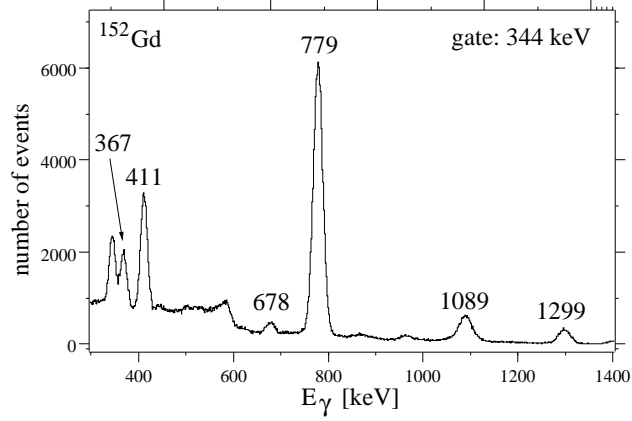


Figure 3.3: Coincidence γ -ray spectrum of the 344 keV decay transition in ^{152}Gd .

energy to obtain the prompt curves shown in Fig. 3.5. The centroids connected by the prompt curve indicated with $C_P(E)_{\text{stop}}$ were obtained by gating the reference energy of 344 keV with the stop detector and varying the gates of the start detector, as illustrated in Fig. 3.4. Analogous, the prompt curve of the stop branch was obtained. Each prompt curve represents a fit of the centroids using Eq. (3.5) and which confirms the result of the CFD time-walk measurement reported in Ref. [21] and presented in Section 3.1. The error of the calibrated prompt curves shown here is only 6-12 ps for the range of $340 \text{ keV} < E_\gamma < 1300 \text{ keV}$. This accuracy is in agreement with the measured centroid uncertainties and is representative for the goodness of the fit.

The two calibrated 344 keV gated prompt curves cross each other at nearly 344 keV, that is exactly the reference energy gate of the system. This is correct, as for equal energy gates, one is not able to distinguish between the γ -rays triggering either both the timing of the start and the stop branch. Thus only one time distribution is obtained for this hypothetical case. This true prompt centroid $C_P(\Delta E_\gamma = 0)$ for the energy combination 344-344 keV could be reproduced using the calibration function of Eq. (3.5). However, the timing of the two timing branches in that experiment is not symmetric, as can be seen in Fig. 3.5. Relative to the energy axis, the time difference between each prompt curve and the horizontal dashed line representing the ideal symmetric timing is different.

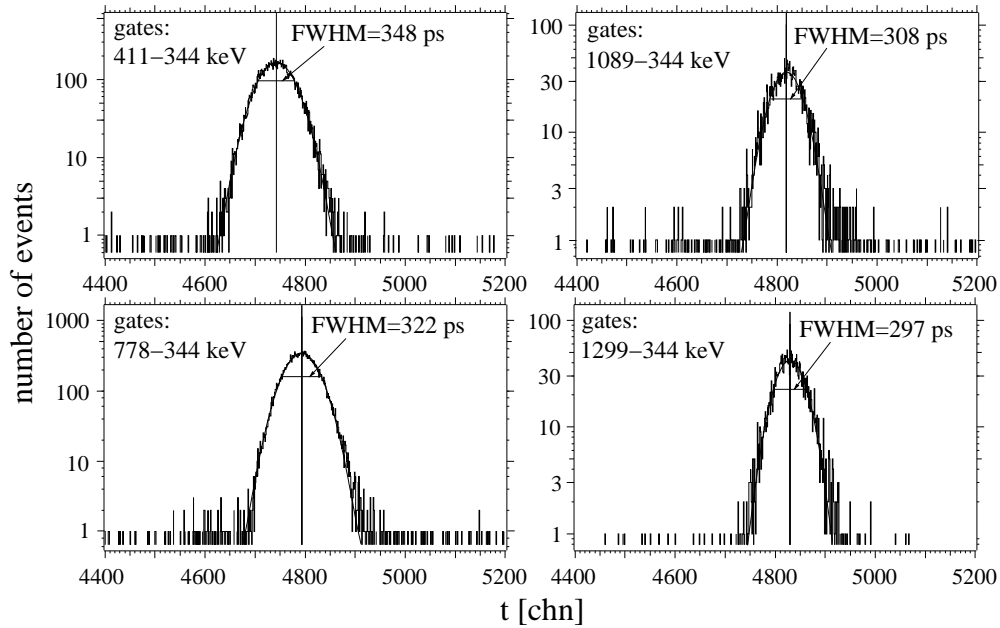


Figure 3.4: $\text{LaBr}_3(\text{Ce})$ γ - γ time distributions of the 2_1^+ state in ^{152}Gd obtained by gating the decaying 344 keV transition (on the delayed detector giving the stop signal for the TAC) and direct feeders of different energies. Centroid positions are illustrated by vertical lines. Figure from Ref. [18].

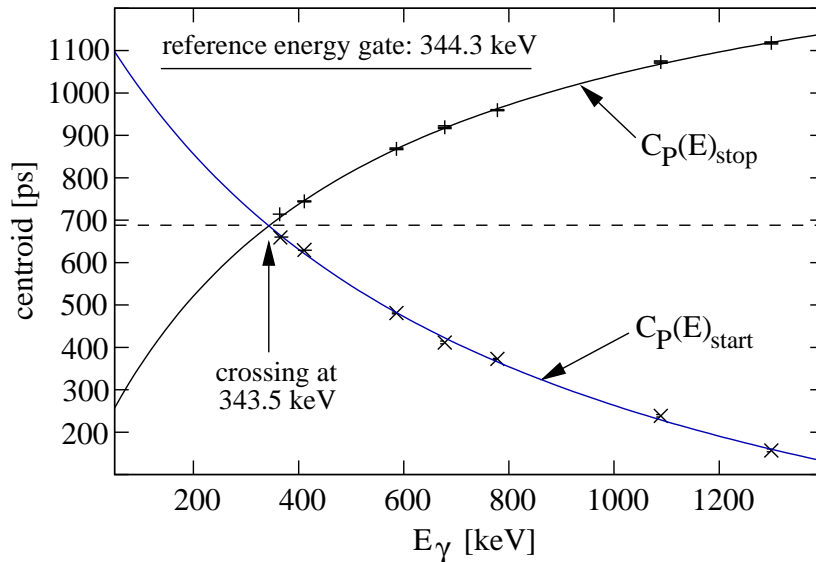


Figure 3.5: The prompt curves of the two timing branches obtained in a γ - γ fast timing experiment using $\text{LaBr}_3(\text{Ce})$ scintillator detectors [18]. The horizontal dashed line represents the ideal case of the symmetric timing, which is the identical timing of both branches for identical energies ($C_P(\Delta E_\gamma = 0) = \text{constant}$). The results are interpreted in the text.

To determine the PRF centroid for an energy combination of the interest, more PRF information is needed. Using other reference energy gates, the resulting prompt curves will be shifted from those presented in Fig. 3.5. This and the timing asymmetry of real fast timing setups makes the determination of the two PRF centroids of interest complex and eventually even impossible (e.g., for $E_\gamma < 344$ keV). The newly proposed mirror symmetric centroid difference method, an extension of the centroid shift method, combines the two branch time-walk characteristics of a γ - γ fast timing setup and simplifies substantially the often difficult measurement of the prompt curve.

3.3 The mirror symmetric centroid difference (MSCD) method

In the previous section it was shown that in application of the γ - γ timing technique, the lifetime of a nuclear excited state can be measured either with the start branch or the stop branch detector. The problem of calibrating the prompt curve still remains, as the time-walk characteristics of the two branches differ in a real setup. Therefore, the prompt curve has to be calibrated for each branch. The timing asymmetry in the branch time-walk characteristics is canceled when defining a new physical quantity, the centroid difference

$$\Delta C = C(D)_{\text{stop}} - C(D)_{\text{start}},$$

for a specific γ -ray cascade in reference to Eq. (3.4). The obtained energy dependent prompt response difference,

$$\text{PRD} = C(P)_{\text{stop}} - C(P)_{\text{start}},$$

describes the combined γ - γ time-walk of the setup and its energy dependency, $\text{PRD}(E_\gamma)$, is called the PRD curve.

We assume for simplification an ideal γ - γ fast timing setup, which means that both timing branches produce identical timing signals for identical energies, as presented in Fig. 3.6. In this example, we consider a decay transition with energy of 800 keV that is the reference energy gate of the system. No background or feeding are contributing to the time distributions. Referring to Eq. (3.4), the centroid curve $C(D)_{\text{stop}}$ is shifted by $+\tau$ from the corresponding prompt curve $C(P)_{\text{stop}}$, as the decay transition, in that case used as the reference timing signal, is gated by the stop detector. If the decay transition is gated by the start detector, the corresponding centroid curve $C(D)_{\text{start}}$ is shifted by $-\tau$ from the prompt curve, as in this case the start detector is affected by the lifetime.

As can be seen in Fig. 3.6, one has to distinguish between $\Delta E_\gamma > 0$ and $\Delta E_\gamma < 0$, where ΔE_γ is the difference of the γ -ray energies of the feeding and decaying transitions:

$$\Delta E_\gamma = E_{\text{feeder}} - E_{\text{decay}}. \quad (3.6)$$

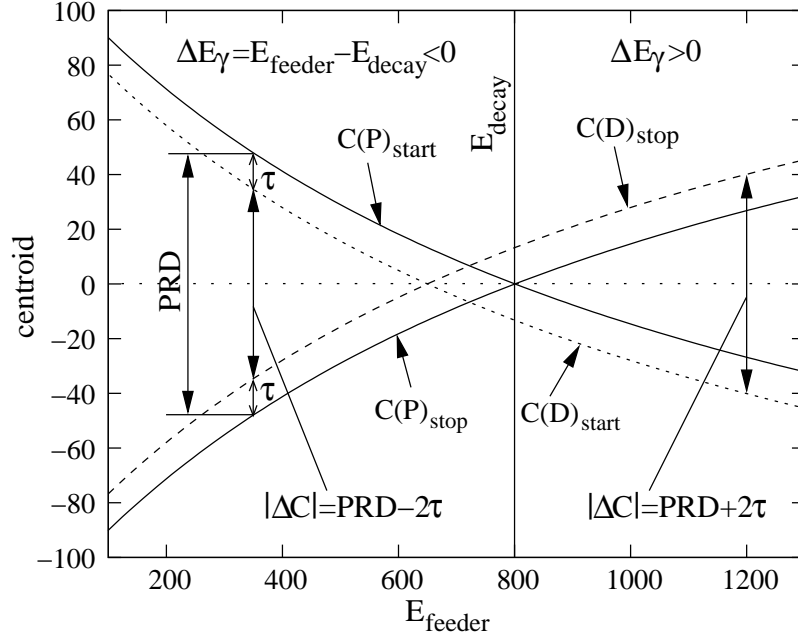


Figure 3.6: 800 keV gated prompt curves $C(P)$ of the two branches of an ideal fast timing setup with symmetric timing characteristics. The dashed curves are the centroid curves related to a lifetime τ obtained if only the decay transition is used as the reference energy gate (walk free timing signal of the system). Note that the relation for the value of the centroid difference ΔC depends on whether the feeding energy is larger or smaller than the decay energy. Figure from Ref. [18].

According to Eq. (3.4), the value of the centroid difference for both cases is given by:

$$|\Delta C| = \begin{cases} |\text{PRD}| + 2\tau & : \Delta E_\gamma > 0 \\ |\text{PRD}| - 2\tau & : \Delta E_\gamma < 0, \end{cases} \quad (3.7)$$

while the centroid difference is defined as:

$$\Delta C(\Delta E_\gamma)_{\text{decay}} = C(D)_{\text{stop}} - C(D)_{\text{start}}. \quad (3.8)$$

The subscript “decay” indicates that the reference timing signal of the setup is provided by a decay transition, which in the case of “ $C(D)_{\text{stop}}$ ” is gated on the stop detector. Fig. 3.7 shows the linearly combined centroid difference curve obtained using Eq. (3.8) and plotted against the energy difference as defined in Eq. (3.6). Using Eq. (3.4), it follows:

$$\begin{aligned} \Delta C(\Delta E_\gamma)_{\text{decay}} &= C_P(\Delta E_\gamma)_{\text{stop}} + \tau - (C_P(\Delta E_\gamma)_{\text{start}} - \tau) \\ &= \text{PRD}(\Delta E_\gamma)_{\text{decay}} + 2\tau. \end{aligned} \quad (3.9)$$

In analogy to the standard Centroid Shift method, the linearly combined centroid difference curve, Eq. (3.9), is shifted by $+2\tau$ from the corresponding PRD curve as illustrated in Fig. 3.7. The $(\Delta C, \Delta E_\gamma)$ -diagram is particularly useful because

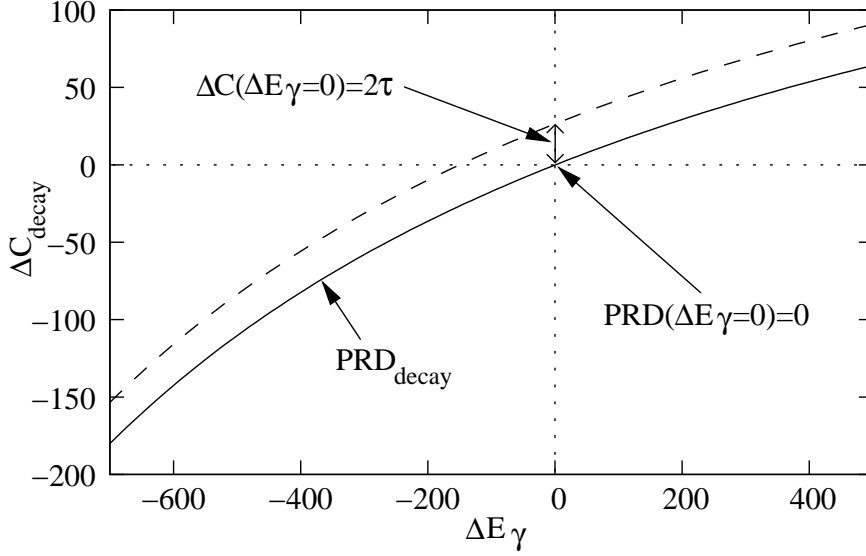


Figure 3.7: The $(\Delta C, \Delta E_\gamma)$ -diagram: The energy dependent PRD describing the PRD curve (solid curve) of a γ - γ fast timing setup is obtained for a decay transition that is used as the reference energy gate of the setup. The combined centroid difference curve related to a lifetime τ (the dashed curve) is shifted from the PRD curve by $+2\tau$. The PRD curve crosses the zero point and therefore, the centroid difference at $\Delta E_\gamma = 0$ corresponds to 2τ . Figure from Ref. [18].

of the zero point crossing of the PRD curve, that makes the direct determination of lifetimes possible, if the centroid difference at $\Delta E_\gamma = 0$ can be interpolated.

Now, we consider a feeding transition that is used as reference energy gate, i.e. the reference timing signal of the setup. Considering Fig. 3.6, the energy axis will then represent the decay energy. For the case of $E_{\text{feeder}} = 800$ keV, the identical prompt curve $C(P)_{\text{stop}}$ is then obtained by gating the reference feeding transition on the stop detector. But, the resulting centroid curve $C(D)_{\text{stop}}$ is then shifted towards shorter times, because now the decay transition with its lifetime information is gated on the start detector. To account for this decay-feeder inversion which is equivalent to the start-stop inversion described by Eq. (3.7), we define the centroid difference for a reference feeding transition as:

$$\begin{aligned}
 \Delta C(\Delta E_\gamma)_{\text{feeder}} &= C(D)_{\text{start}} - C(D)_{\text{stop}} \\
 &= C_P(\Delta E_\gamma)_{\text{start}} + \tau - (C_P(\Delta E_\gamma)_{\text{stop}} - \tau) \\
 &= \text{PRD}(\Delta E_\gamma)_{\text{feeder}} + 2\tau.
 \end{aligned} \tag{3.10}$$

Again, the subscript “feeder” indicates that the reference timing signal is provided by a feeding γ -ray which in the case of $C(D)_{\text{start}}$ is gated on the start detector. Using Eqs. (3.6) and (3.8-3.10), the experimentally obtained centroid differences are well defined in the $(\Delta C, \Delta E_\gamma)$ -diagram. If we consider a cascade of two subsequent γ -rays with different γ -ray energies ($E_{\text{decay}} \neq E_{\text{feeder}}$) and the energy combination $\Delta E_{\text{casc.}} = E_{\text{feeder}} - E_{\text{decay}}$ as defined in Eq. (3.6), then Eqs. (3.9)

and (3.10) are equivalent to:

$$\Delta C(\Delta E_{\text{casc.}})_{\text{decay}} = \Delta C(\Delta E_{\text{casc.}})_{\text{feeder}}, \quad (3.11)$$

$$\text{PRD}(\Delta E_{\text{casc.}})_{\text{decay}} = \text{PRD}(\Delta E_{\text{casc.}})_{\text{feeder}} \quad (3.12)$$

and accordingly:

$$\text{PRD} = 0 \text{ and } \Delta C = 2\tau \text{ for } \Delta E_{\gamma} = 0. \quad (3.13)$$

Fig. 3.8 shows the (800 keV gated) $\text{PRD}_{\text{decay}}$ curve, as presented in Fig. 3.7, and the $\text{PRD}_{\text{feeder}}$ curve obtained when the reference energy gate corresponds to the energy of the feeding transition [Eq. (3.10)] of the investigated cascade, in this example with $E_{\text{feeder}} = 1190$ keV. Note that the $\text{PRD}_{\text{feeder}}$ curve is convex, while the $\text{PRD}_{\text{decay}}$ curve is concave. As illustrated in Fig. 3.8, the relations of Eqs. (3.11-3.13) denote that for the specific energy combination $\Delta E_{\text{casc.}}$, the centroid difference (PRD) is independent of whether the reference energy gate corresponds to the energy of the feeding or the decaying transition. This is independent of the energy combination and thus the measurement of centroid differences cancels the timing asymmetry of the two timing branches in a real γ - γ fast timing setup.

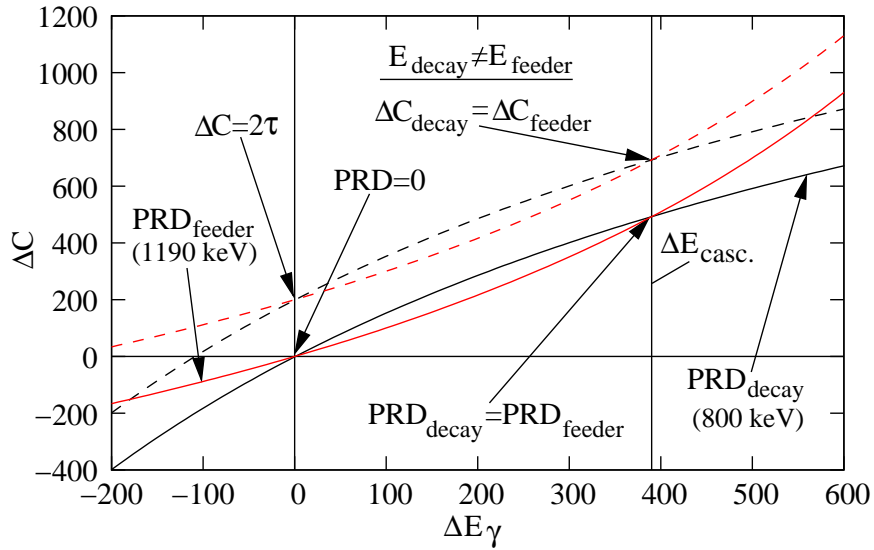


Figure 3.8: The two centroid difference curves and corresponding PRD curves are obtained when the reference energy gate corresponds to the energy of the decay transition (800 keV) of a γ -ray cascade (e.g., $\text{PRD}_{\text{decay}}$), or to the feeding transition [Eq. (3.10)], respectively. Corresponding to the energy combination, the two curves cross each other at $\Delta E_{\gamma} = E_{\text{feeder}} - E_{\text{decay}}$ and accordingly at $\Delta E_{\gamma} = 0$ [Eq. (3.13)]. Figure from Ref. [18].

In the majority of cases, the calibration of the PRD for an energy combination of the interest is needed. Considering a specific reference energy gate ($E_{\text{ref.}} = \text{constant}$) which corresponds to the energy of a feeding transition ($E_{\text{ref.}} = E_{\text{feeder}} \Leftrightarrow$

$\Delta E_\gamma = E_{\text{ref.}} - E_\gamma$), the PRD can be written as:

$$\begin{aligned} & \text{PRD}(-\Delta E_\gamma)_{\text{feeder}} \\ &= C_P(E_\gamma - E_{\text{ref.}})_{\text{start}} - C_P(E_\gamma - E_{\text{ref.}})_{\text{stop}} \\ &= -[C_P(E_\gamma - E_{\text{ref.}})_{\text{stop}} - C_P(E_\gamma - E_{\text{ref.}})_{\text{start}}]. \end{aligned} \quad (3.14)$$

For a decay transition that is used as reference signal, Eq. (3.6) is equivalent to $\Delta E_\gamma = E_\gamma - E_{\text{ref.}}$ and thus Eq. (3.14) is equivalent to:

$$\text{PRD}(\Delta E_\gamma)_{\text{decay}} = -\text{PRD}(-\Delta E_\gamma)_{\text{feeder}}, \quad (3.15)$$

$$\Delta C(\Delta E_\gamma)_{\text{decay}} = -\Delta C(-\Delta E_\gamma)_{\text{feeder}}. \quad (3.16)$$

These mirror symmetric relations imply that the value of the centroid difference (PRD) for any energy combination is independent of the reference energy gate of the system, which is in agreement with Eqs. (3.11-3.13). This means in particular, that the PRD for any energy combination is obtained from the PRD curve regardless of the reference energy gate used to calibrate the PRD curve.

Beside the cancellation of timing asymmetries and the ability to derive the PRD for any energy combination, the use of the MSCD method provides the following supremely advantageous features:

1. The zero point in the $(\Delta C, \Delta E_\gamma)$ -diagram can be used as a universal prompt calibration point, because Eq. (3.13) is independent of energy and possible timing asymmetries of the two timing branches.

2. Due to mirror symmetry, Eqs. (3.15-3.16), a centroid difference ΔC can be used twice dependent on whether the feeding or the decaying transition is considered. This can provide additional PRDs which is very useful for the calibration of the PRD curve.

3. The possible time shift called “electronic drift” due to thermal fluctuations in electronics cancels, because this shift is independent of energy and therefore affects both time distributions in the same way.

4. In γ - γ timing experiments, the PRD curve is independent of the setup geometry. Like in point 3, a change of the setup geometry results in an energy independent shift of both time distributions in the same way. This feature is also very useful for the calibration of the PRD curve.

5. Trivially, by combining the two centroids of the two time spectra of a cascade, this is equivalent to an increase of statistics.

6. Corollary, the final total error of the lifetime determination is reduced.

7. Due to Eq. (3.13), one can determine picosecond lifetimes even without calibrating the PRD curve, if the combined time-walk characteristics is known. If enough data points for a reference feeding or decaying transition are available and one of these is near to the zero point, e.g., for $|\Delta E_\gamma| < 100$ keV, the data points then can be fitted and the value of the interpolated or extrapolated centroid difference at $\Delta E_\gamma = 0$ is equal to 2τ .

Chapter 4

The $\text{LaBr}_3(\text{Ce})$ scintillator detector characteristics

The aim of this Chapter is to fully characterize the timing properties of the $\text{LaBr}_3(\text{Ce})$ scintillator detector. This includes the determination of the detector response linearity and its response resolution at different operating conditions in order to investigate for limitations in the application of the fast timing technique using $\text{LaBr}_3(\text{Ce})$ scintillator detectors. For these purposes, standard γ -ray sources as ^{60}Co , ^{133}Ba , ^{152}Eu and ^{226}Ra were used. Fig. 4.1 shows the singles γ -ray spectrum obtained from the ^{152}Eu source which decays to ^{152}Gd via β -emission (a portion of the ^{152}Gd level scheme is presented in Chapter 3.1.1) and also to ^{152}Sm via electron capture decay. The partial level scheme of ^{152}Sm is shown in section 4.2.1. Both daughters provide many γ -rays with different energies covering a wide dynamic range, which is ideal to measure various detector characteristics. For energy measurements, the preamplified PMT dynode output pulse is sent to a main amplifier for pulse height analysis. Analogous studies were made using the PMT anode pulse. Except the pulse height, no significant discrepancy in the linearity and the resolution of the response (pulse height) obtained from the anode and the dynode pulses could be observed.

4.1 Non-linearity and resolution

Based on “The theory and practice of scintillation counting” published by J. B. Birks in 1964 [44] and reviewed in detail in Ref. [31], the detector relative energy resolution can be expressed by

$$R^2 = \left(\frac{\Delta E}{E}\right)^2 = R_{\text{Sc.}}^2 + R_{\text{PMT}}^2. \quad (4.1)$$

The scintillator resolution $R_{\text{Sc.}}$ is due to Poisson statistics of the scintillation photons created per energy deposition (the intrinsic resolution) and includes the light yield non-proportionality and the geometry of the crystal [31]. Other possible non-uniformities in the transfer of γ -rays to photoelectrons are assumed to be

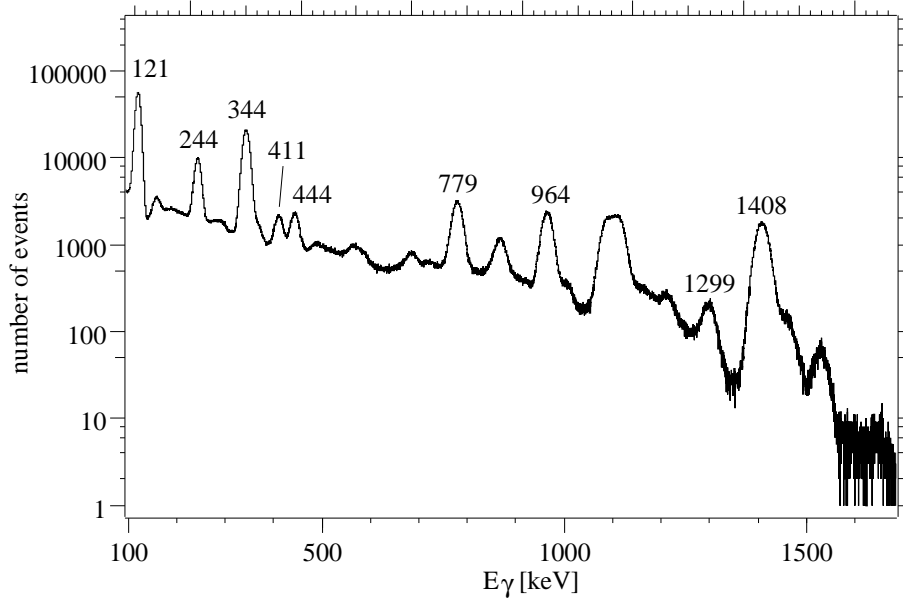


Figure 4.1: Singles γ -ray spectrum of the ^{152}Eu source obtained using the 5% doped $\text{LaBr}_3(\text{Ce})$ scintillator plus XP20D0 PMT detector assembly. The positions of the labeled full energy peaks were used to investigate for the detector response non-linearity.

negligible compared to the other components of the energy resolution [31]. Then, the relative energy resolution in term of $\Delta E = \text{FWHM}$ of the full energy peak is written as

$$R = 2.355 \sqrt{\frac{1 + \nu}{N_{\text{phe}}}}, \quad (4.2)$$

where ν is the variance of the electron multiplication or the PMT gain, respectively.

Investigations on non-linearities using different PMTs and different operation voltages have been performed, as illustrated in Fig. 4.2. The XP2020 PMT is known to provide very good linearity due to small gain variance of about 1% [31]. This could also be observed in a wide range of operation voltages (1400 V-1900 V). For the XP20D0 PMT, a non-linear and in some cases even a non-monotonic (wavy) response was observed. No report on characteristics for the case of non-linear response of the XP20D0 was found. For some XP20D0 PMTs¹, a very good response linearity was obtained, but only in a narrow range of operation namely at voltages of 700 V-800 V. In some cases, the best linearity is obtained only for a specific operation voltage. As shown in Fig. 4.3a, non-linearities, i.e. deviations from linear behavior smaller than 1% could be obtained. Below the minimum applicable voltage of about 700 V, the response becomes non-monotonic and energy resolution rapidly becomes worse. When increasing the PMT operation voltage, non-linearity increases and saturation effects for $E_\gamma > 1.5$ MeV appear at about -1400 V. At higher operation voltages (850 V-1300 V) however,

¹At the IKP, five $\text{LaBr}_3(\text{Ce})+\text{XP20D0}$ assemblies were available

a smooth monotonic response of the XP20D0 is obtained which is well described using a polynomial of second order, as illustrated in Figs. 4.2 and 4.3b. In any case, the factor of the quadratic term of the fitted polynomial is smaller than 10^{-4} times the factor of the linear term.

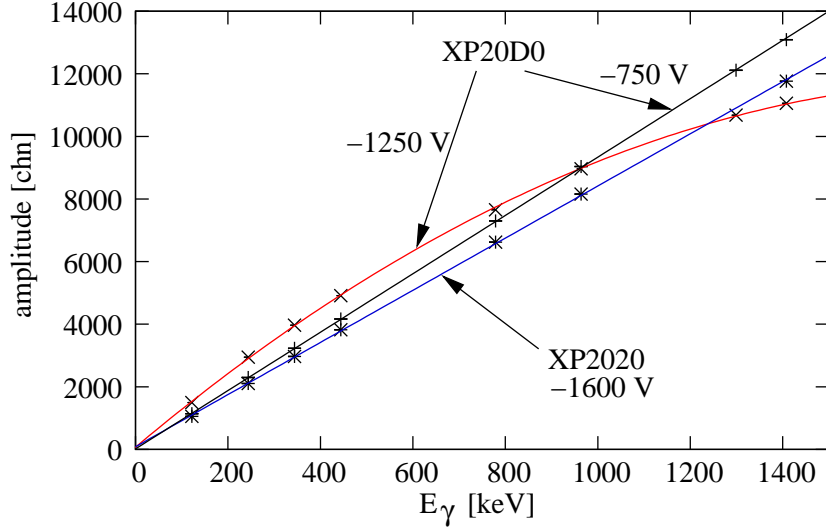


Figure 4.2: Amplitude versus γ -ray energy relation in dependence on the PMT operation voltage for different PMTs. Note the monotonic response characteristics of the non-linear operated XP20D0 PMT at -1250 V, which was fitted using a polynomial of second order.

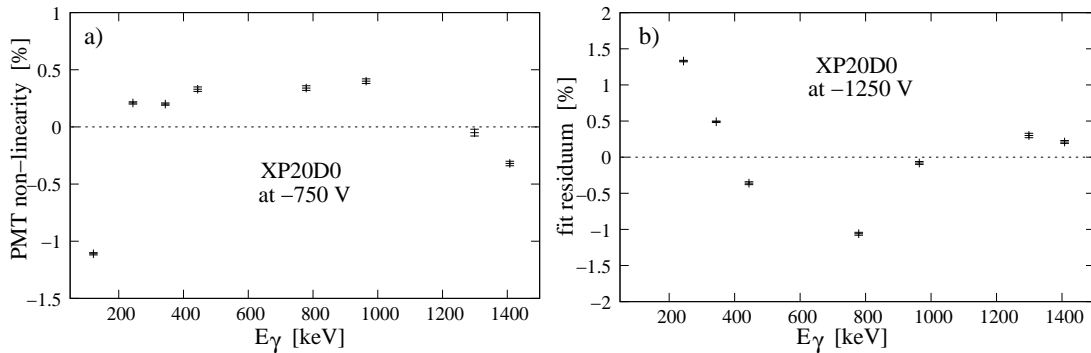


Figure 4.3: a: Relative deviation from the ideal linear PMT response at low PMT operation voltage (“linear operation”). b: Relative deviation from the fitted second order polynomial for the non-linear operation with higher voltages, as shown in Fig. 4.2.

The effect of non-linear PMT response on the energy resolution is depicted in Fig. 4.4. As the number of photoelectrons created at the photocathode is directly proportional to the detected γ -ray energy, Eq. (4.2) can be written as

$$R(E_\gamma)_{\text{lin.}} = \frac{\alpha}{\sqrt{\beta + E_\gamma}}, \quad (4.3)$$

with α and β being free fit parameters. For the case of linear operation [$A(E_\gamma) \propto E_\gamma$], Eq. (4.3) exactly reproduces the experimental data, as shown in Fig. 4.4. This simply reflects the Poisson statistics in creation of N_{phe} and confirms the results presented by P. Dorenbos et al. [31]. The energy resolution for the non-linear operation mode could not be reproduced using Eq. (4.3) even using a polynomial to describe the energy dependency of the amplitude. The linear term of the polynomial dominates and the resulting fit does not differ significantly from the linear operation mode. But, when adding a linear term to Eq. (4.3), thus using

$$R(E_\gamma)_{\text{nonlin.}} = \frac{\alpha}{\sqrt{\beta + E_\gamma}} + \gamma E_\gamma, \quad (4.4)$$

where γ is another free fit parameter, the energy resolution for the non-linear case could be reproduced remarkably well. As the linear term of the polynomial dominates in the response, the relative energy resolution for the non-linear operation of the XP20D0 PMT can be written as

$$R(E_\gamma)_{\text{nonlin.}} = R(E_\gamma)_{\text{lin.}} + \gamma E_\gamma. \quad (4.5)$$

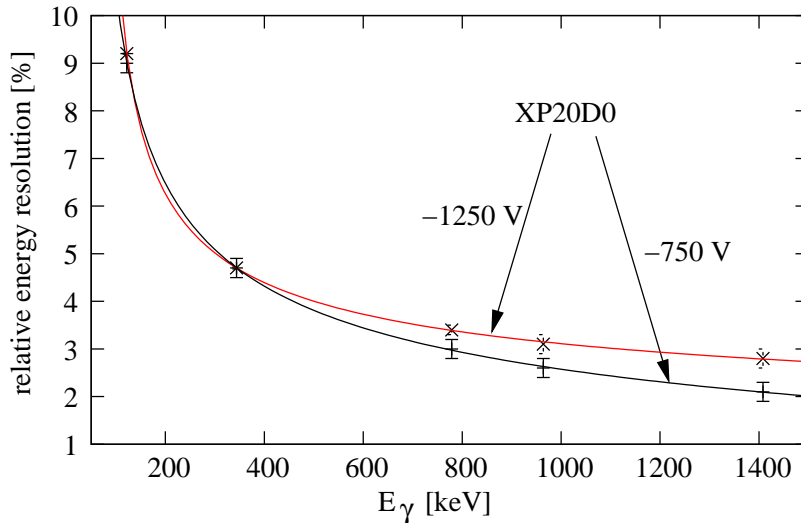


Figure 4.4: Relative energy resolution in dependence on γ -ray energy obtained for different operation voltages of the XP20D0 PMT. For $E_\gamma > 350$ keV, the non-linear operation mode (-1250 V) makes the energy resolution slightly worse. The fit of these data points was obtained using Eq. (4.4), as explained in the text. For the case of linear operation (-750 V), the energy resolution results from statistical amplitude variations [Eq. (4.3)].

An important observation is that for $E_\gamma < 350$ keV, the energy resolution is not affected by the PMT response of either the linear or the non-linear operation mode. This can be explained referring to Fig. 4.2, where the response for $E_\gamma < 350$ keV is almost linear even at higher operation voltages. This is very useful for lifetime measurements using low-energy events.

The energy resolution obtained using the XP2020 PMT is almost the same, maybe slightly worse by factor of about 1.1. A non-linear operation of the XP2020 was not practicable as saturation effects already appear at about -2000 V due to higher number of dynodes resulting in a higher gain of the converted high $\text{LaBr}_3(\text{Ce})$ scintillation light output. Using voltages lower than -1400 V, energy resolution becomes worse due to non-monotonic PMT response.

Results of time resolution measurements using the XP20D0 PMT with different operation voltages are presented in Fig. 4.5. Increasing the PMT voltage results in a reduction of the total PMT transit time spread and an increase in gain, thus in a better time resolution. An improvement by factor 1.2 can be obtained, if the energy resolution is not of particular interest. For low-energy events, the non-linear operation mode is definitely the better choice. For the XP2020 PMT, the best time resolution obtainable is comparable to that of the XP20D0 obtained using the linear operation mode. Thus the use of XP20D0 PMT indeed provides better time resolution with improvement by factor of up to 1.2.

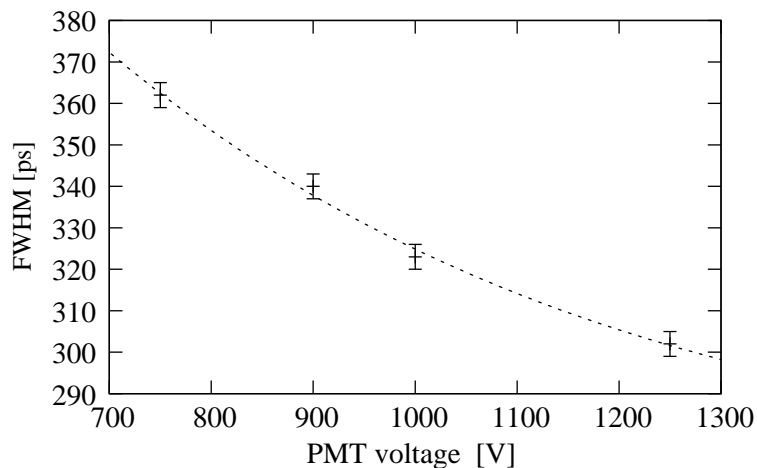


Figure 4.5: Time resolution of the $\text{LaBr}_3(\text{Ce})+\text{XP20D0}$ γ -ray detector assembly in dependence on the PMT operation voltage. Both PMT voltages were adjusted to the same indicated operation voltage. The time resolution is expressed by the FWHM of the time distribution obtained for the cascade $779 \text{ keV} \rightarrow 344 \text{ keV}$ in ^{152}Gd (See the level scheme in Fig. 3.2, Chapter 3.1.1). The nearly linear dashed line is only to guide the eye.

4.2 Time-walk analysis using γ -ray sources

The most important issue for lifetime measurements using the centroid shift method or the MSCD method, respectively, is to determine the energy dependency of the PRF centroid, hence the determination of the prompt curve or the PRD curve. Using small crystals, the prompt curve can be approximated using

the prompt ^{60}Co γ -ray source [13, 14]. This source emits only two γ -rays after β -decay to ^{60}Ni . The 1173 keV γ -ray feeds the first 2^+ state in ^{60}Ni which decays by the 1333 keV transition with lifetime of 1.5(6) ps [43], which is prompt for a fast timing setup.

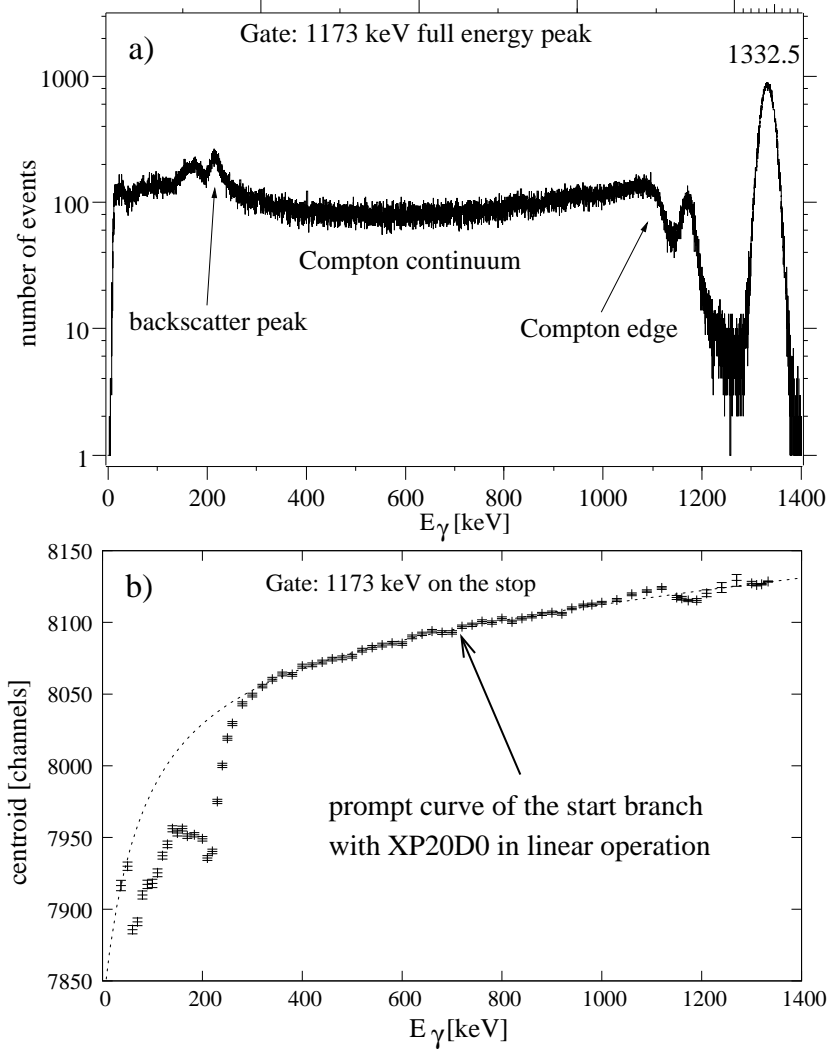


Figure 4.6: a: Coincidence γ -ray spectrum of ^{60}Co obtained by gating the stop detector on the 1173 keV full energy peak. b: Approximated time-walk characteristics of the start detector obtained using the γ -ray spectrum of the prompt ^{60}Co source in coincidence with the 1173 keV full energy peak which was gated by the stop detector. The dashed line representing the expected prompt curve is fitted to the data points with $E_\gamma > 300$ keV using Eq. (4.6). The time spectrum calibration is 2.54 ps/chn.

As illustrated in Fig. 4.6a, the typical γ -ray spectrum of the 1333 keV decay transition was obtained by gating the stop detector on the 1173 keV feeding transition. The Compton continuum results from the 1333 keV γ -rays and thus the time distributions obtained by gating on it should also be prompt. The start

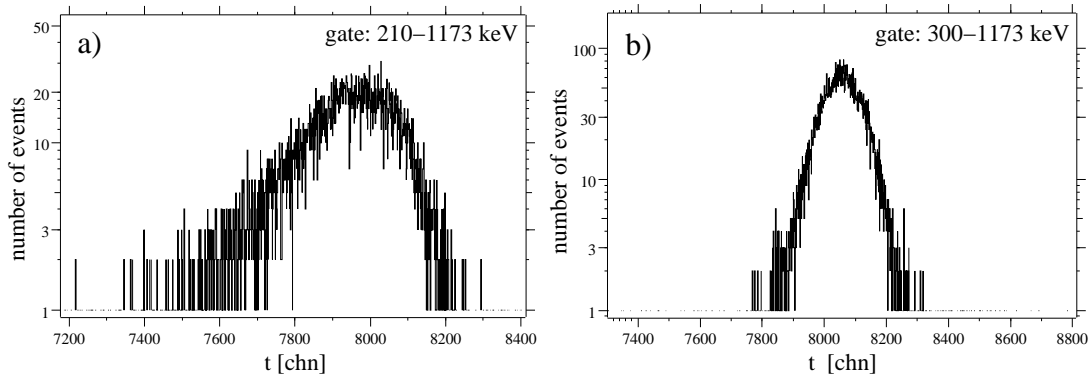


Figure 4.7: a: Time spectrum of the backscatter peak at 210 keV in coincidence with the 1173 keV full energy peak of ^{60}Co . b: Time spectrum obtained for the combination 300-1173 keV. As this one, the time distributions for $E_\gamma > 300$ keV are nearly identical to the Gaussian distribution, as expected for prompt events.

detector in this experiment consisted of the standard detector equipped with the XP20D0 PMT, while the stop detector was equipped with the XP2020 PMT. Both PMTs were adjusted to deliver almost linear response. A shaping delay time of $t_d = 16$ ns was chosen for the CFD timing of the start branch (with XP20D0). For the stop branch, the shaping delay time was $t_d = 5$ ns.

Fig. 4.6b shows the centroids of the time spectra obtained by gating the stop detector on the 1173 keV full energy peak and varying the ≈ 10 keV wide gates of the start detector in steps of 20 keV. For energies below 300 keV, the time spectra have asymmetries towards the negative time scale, as shown in Fig. 4.7a. The backscatter peak at 210 keV results from a Compton event in the environment around the detector. While the primary energy transfer is deposited in the environment, the backscattered γ -ray is detected after full energy absorption via the photoelectric effect. Therefore, the time spectrum of the backscatter peak is artificially delayed. Also, scattered and backscattered γ -rays can leave one crystal to hit the other detector crystal, which are called the cross-talk events. This can be an explanation for the delayed structure below 300 keV.

For energies above 300 keV, however, the time spectra are almost symmetric (see Fig. 4.7b) and the progression of the centroids with energy is very smooth and monotonic up to $E_\gamma \approx 1$ MeV. Then, a small structure due to multiple Compton events and the full energy centroid at 1333 keV are obtained. For $E_\gamma > 800$ keV, the time-walk is almost linear. Therefore, the centroids for $E_\gamma > 300$ keV were fitted using

$$C(E_\gamma) = \frac{a}{\sqrt{b + E_\gamma}} + cE_\gamma + d, \quad (4.6)$$

which corresponds to the derived CFD timing of Eq. (2.15) including a linear term to account for the obtained linear time-walk for $E_\gamma > 800$ keV.

An analogous time-walk analysis was performed on the stop timing branch, as presented in Fig. 4.8. The stop branch detector of this setup consisted of a $\text{LaBr}_3(\text{Ce})$ scintillator connected to the XP2020 PMT. A similar time-walk characteristics is obtained, only the timing for $E_\gamma > 500$ keV is almost linear

with a very small slope. Compared with the start branch, the timing of the stop branch is not symmetric, though both PMTs were adjusted for linear operation. Obviously, the slope of the prompt curve at higher energies is dependent on the CFD shaping delay time t_d . For $E_\gamma > 300$ keV, also the time-walk characteristics of the stop branch could be calibrated using Eq. (4.6). The statistical error for each prompt curve determination is in the range of 10-15 ps. If we consider the prompt curve of the start branch, the time-walk between the energies of 344 keV and 1173 keV is

$$\Delta C_P(1173 - 344)_{\text{start}} = C_P(1173)_{\text{start}} - C_P(344)_{\text{start}} = 148(11) \text{ ps.} \quad (4.7)$$

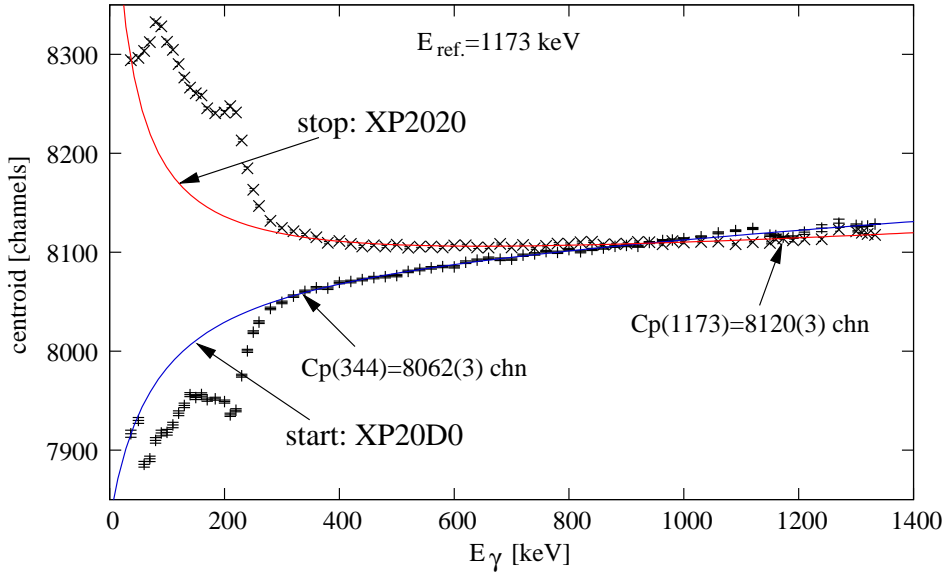


Figure 4.8: Time-walk of the two timing branches obtained for the same reference energy gate of 1173 keV. A very strong timing asymmetry is observed. From the prompt curve of the “start” branch, two prompt centroids are interpolated for further analysis. The relative difference of these centroids corresponds to $\Delta C_P(1173 - 334)_{\text{start}} = 58(4.3) \text{ chn} = 148(11) \text{ ps}$.

Further analyzes were performed in order to derive the shift of the prompt curve obtained when using other reference energy gates. In Fig. 4.9, the prompt curves obtained by gating the start detector on two different reference energies are compared. The 344 keV gated centroids show a slightly different structure than those obtained for the gate of 1173 keV. However, a parallel shift of the prompt curve can be observed, as expected for a characteristics when using different reference timing signals having different amplitudes with resulting time-walk effects of the reference detector. The shift between the two prompt curves obtained by gating the start detector on the two different reference energies shown in Fig. 4.9 corresponds to

$$\Delta C_P(E_\gamma)_{\text{start}} = C_P(E_\gamma)_{1173} - C_P(E_\gamma)_{344} = 143(15) \text{ ps.} \quad (4.8)$$

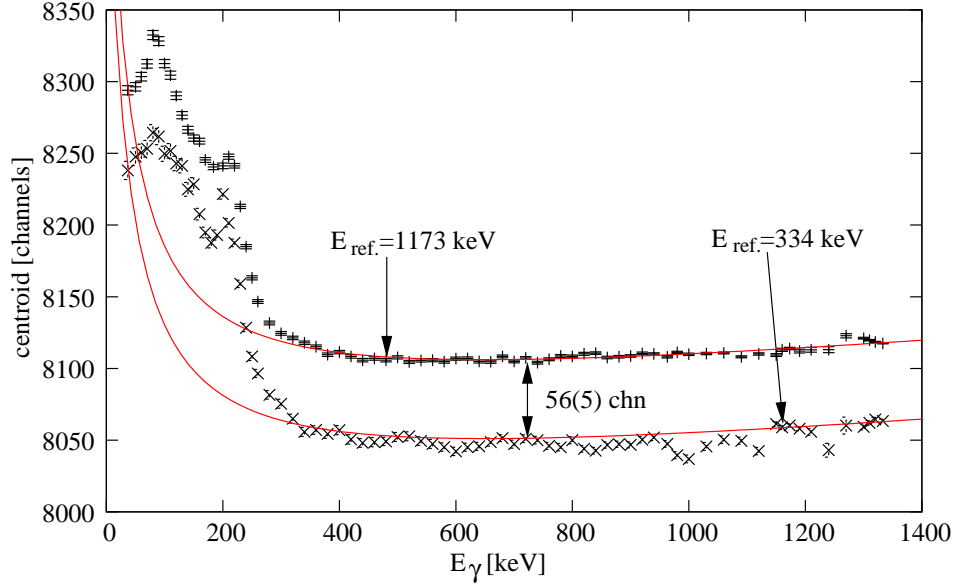


Figure 4.9: Time-walk of the stop branch using different reference energy gates with the start detector. Note the parallel shift of the prompt curve. This shift corresponds to the relative difference of the start branch centroids for the two given reference energies (see also Fig. 4.8)

This result is in agreement with the relative time-walk of the start detector between the two energies, as illustrated in Fig. 4.8 and given by Eq. (4.7). Analogously, the shift between the prompt curves of the start branch obtained for gating the stop detector on different energies can be derived. The result in that case is

$$\Delta C_P(E_\gamma)_{\text{stop}} = C_P(E_\gamma)_{1173} - C_P(E_\gamma)_{344} = 7(15) \text{ ps.} \quad (4.9)$$

Most interesting is the linear combination of the two prompt curves obtained for a specific reference energy gate by subtracting the one from the other one to obtain the PRD curve which is the principle of the MSCD method. The data points of both the start and the stop branch obtained for the reference energy of 1173 keV as shown in Fig. 4.8 are subtracted using $\Delta C(E_\gamma)_{1173} = C(E_\gamma)_{\text{stop}} - C(E_\gamma)_{\text{start}}$ and the resulting centroid differences are plotted against the γ -ray energy, as presented in Fig. 4.10. For comparison, the two calibrated prompt curves (solid lines in Fig. 4.8) were also combined to obtain the PRD curve presented in Fig. 4.10 indicated with $E_{\text{ref.}} = 1173 \text{ keV}$.

An analogous MSCD analysis was made using the reference energy gate of 344 keV, the result is also presented in Fig. 4.10. Obviously, this reference energy is not appropriate for calibration purposes. A significant structure of the centroid differences is observed in that case, especially in the region of the Compton edges of the two ^{60}Co γ -rays. However, a parallel shift of the PRD curve for different reference energy gates is observed. As a linear combination of two characteristics, the PRD curve represents the γ - γ time-walk characteristics of the whole setup. The parallel shift of the PRD curve for different reference energies can be derived

from the 1173 keV gated PRD₁₁₇₃ curve as well as from the 344 keV gated PRD₃₄₄ curve as follows:

$$\begin{aligned} \text{PRD}(1173 - 344)_{1173} &= \text{PRD}(1173)_{1173} - \text{PRD}(344)_{1173} \\ &= -\text{PRD}(344 - 1173)_{344} = 138(13) \text{ ps}, \end{aligned} \quad (4.10)$$

which reflects the mirror symmetry of the MSCD method [see also Eqs. (3.15-3.16)]. Departing from the single branch time-walk characteristics and considering Eqs. (4.8-4.9), it follows

$$\text{PRD}(1173 - 344) = |\Delta C_P(E_\gamma)_{\text{stop}} - \Delta C_P(E_\gamma)_{\text{start}}| = 136(21) \text{ ps}, \quad (4.11)$$

which is in very good agreement with the result derived from the PRD curve. Due to combination of centroids and resulting reduction of the statistical error, the result obtained from the PRD curve is more precise.

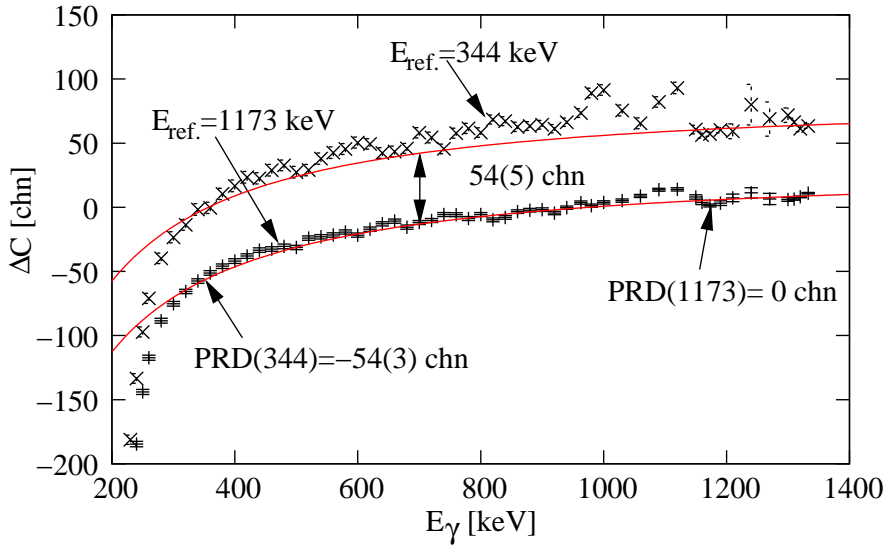


Figure 4.10: Linear combination of the two time-walk characteristics of the γ - γ fast timing setup obtained by measuring the “centroid difference”. The value of the parallel shift of the PRD curve is given by the relative difference of the two interpolated PRDs at corresponding reference energies.

To investigate the quality of the PRD curve obtained due to Compton events in combination with the 1173 keV full energy peak from the ^{60}Co source, the lifetime of the first 2^+ state at 344 keV in ^{152}Gd was measured using the same experimental setup. As explained in Chapter 3.2, the 344 keV decay transition is used as the reference energy gate of the system. Fig. 4.11 illustrates the principle of the MSCD analysis: For a specific cascade, the centroid difference of the two time spectra obtained by gating the detectors in the two possible ways is measured. This is made for every energy combination of the 344 keV decay transition with a coincident feeding transition. To obtain the PRD, the measured centroid difference is corrected by twice the lifetime of the 2_1^+ state in ^{152}Gd . As

shown in Fig. 4.12, the obtained 344 keV gated PRDs are plotted against the γ -ray energy, corresponding to the different feeding transitions. On the energy axis at the reference energy of 344 keV, a data point is added and used to calibrate the PRD curve [$\text{PRD}(\Delta E_\gamma = 0) = 0$]. Assuming Eq. (4.6) to describe the time-walk characteristics of the single timing branches, the full energy prompt calibration points (the PRDs) were fitted using:

$$\Delta C(E_\gamma) = \frac{a}{\sqrt{b + E_\gamma}} + cE_\gamma + d, \quad (4.12)$$

with resulting statistical uncertainty of only 8 ps for $340 \text{ keV} < E_\gamma < 1300 \text{ keV}$ (2σ deviation).

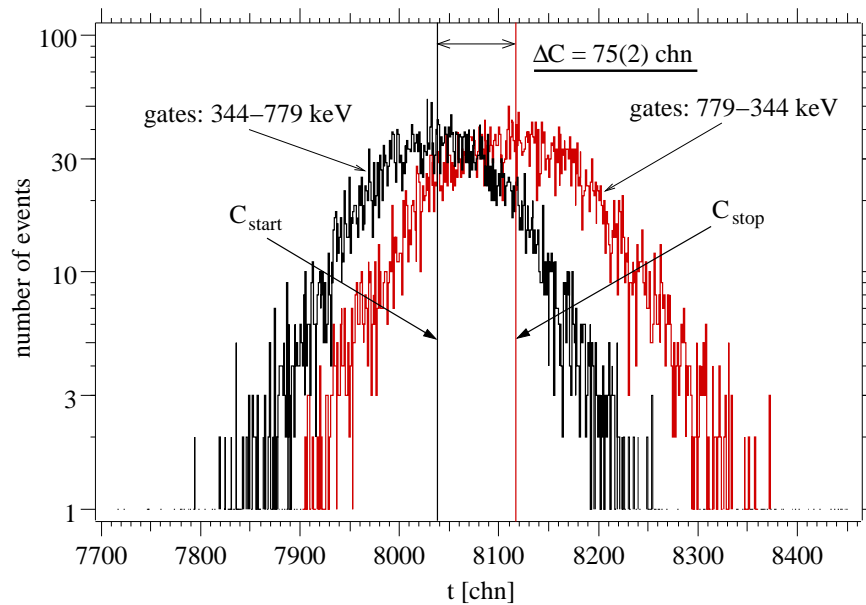


Figure 4.11: The centroid difference of the cascade $779 \text{ keV} \rightarrow 344 \text{ keV}$ connecting the 2_1^+ state at 344 keV in ^{152}Gd . The time spectra were obtained by gating on the 344 keV decay transition once by the start detector, e.g. C_{start} , and once by the stop detector (and ditto for the feeding transition). The statistical error for the centroid difference is calculated as $d(\Delta C) = \sqrt{(dC_{\text{start}})^2 + (dC_{\text{stop}})^2}$ with dC according to Eq. (3.3).

For comparison, the 1173 keV gated data points of the ^{60}Co source shown in Fig. 4.10 were shifted in parallel until the full energy events of ^{60}Co at 1173 keV and 1333 keV are fitting the calibrated full energy events PRD curve, as presented in Fig. 4.12. Obviously, the Compton events induce systematical deviations from the true PRD curve. The shift of the Compton events relative to the full energy events is in the range of 20-40 ps (10-20 ps for one detector), which is much larger as the observations made in Ref. [14]. There, a small $1/2'' \times 1/2''$ cylindrical BaF_2 scintillator was used for timing experiments. The observed delay is explained to be a result of a contribution of a multiple Compton interaction in creation of

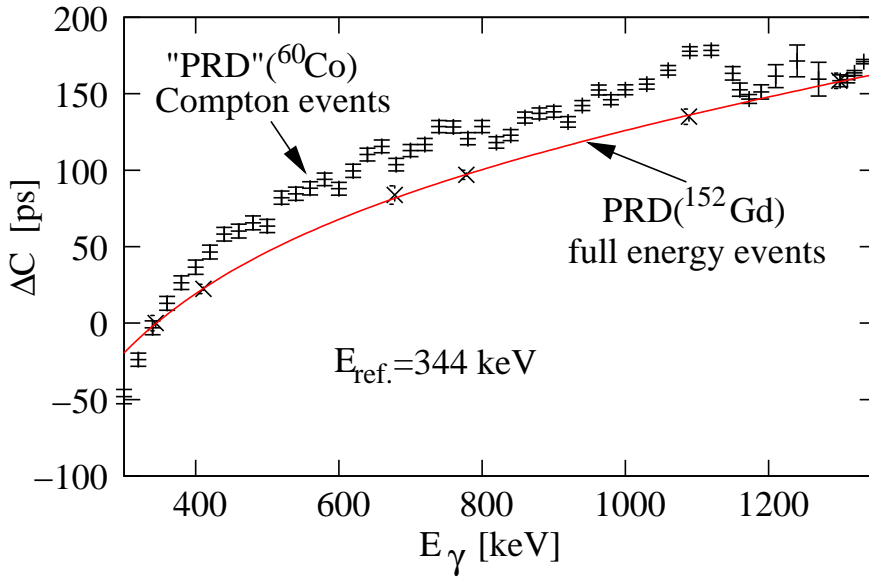


Figure 4.12: The centroid difference diagram of the γ - γ fast timing setup. Discrepancy between the combined time-walk characteristics obtained due to full energy events (^{152}Gd) and due to the Compton events of the prompt ^{60}Co γ -ray source. This result is interpreted in the text.

the full energy event. The artificial delay is related to the time-of-flight of the scattered γ -rays [14]. This statement is confirmed with respect to the larger scintillator volume used for this work. For $E_\gamma \gtrsim 350$ keV, the 1173 keV full energy event is delayed relative to a Compton event. The largest shift is observed at the Compton edge, where a single “knock-on” interaction of the primary γ -ray evokes a real prompt Compton event. Below the Compton edge, multiple Compton interactions are contributing to the Compton continuum and thus the shift is a little reduced. Below about 450 keV, the low energy Compton events seem to be contaminated by background as backscatter γ -rays, cross-talk events or scattered γ -rays from the experimental surrounding. These background events are largely delayed relative to full energy events. Therefore, these events are shifted in the opposite direction, as can also be seen in Fig. 4.7a.

4.3 The PRD calibration procedure

Based on the fact that only full energy events reproduce the true PRD curve, a highly reliable and very precise procedure to calibrate the PRD curve was developed. The ^{152}Eu γ -ray source allows for precise PRD calibration in the range of $240 \text{ keV} < E_\gamma < 1300 \text{ keV}$, which often is sufficient. For lower energies down to 53 keV, the ^{133}Ba γ -ray source can be used. To access higher energies, MSCD analyzes were also performed on the ^{226}Ra γ -ray source.

The setup of this experiment consisted of two standard IKP $\text{LaBr}_3(\text{Ce})$ plus XP20D0 detectors. To provide good signal-to-noise ratio for low energy events,

the PMT voltages were adjusted to about -850 V. A very small non-linear detector response at higher energies was observed. The energy spectrum could be calibrated very well using a polynomial of second order. For both timing branches, a CFD shaping delay time of $t_d = 20$ ns was chosen to ensure TCF timing.

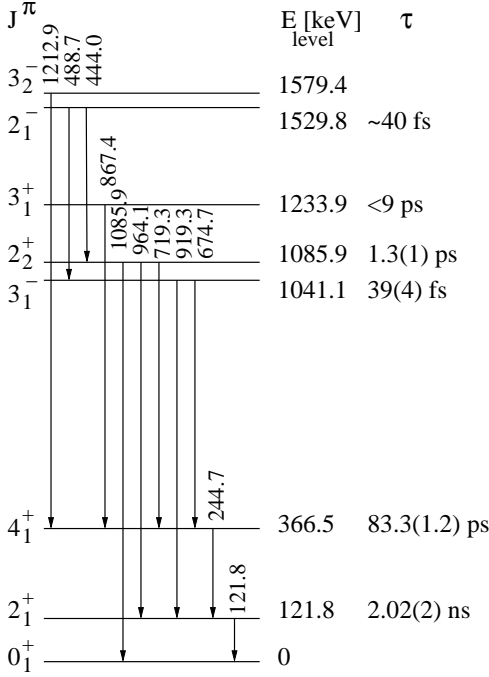


Figure 4.13: Partial level scheme of ^{152}Sm obtained after electron capture decay of ^{152}Eu . J^π , E_{level} , E_γ and τ from Ref. [43].

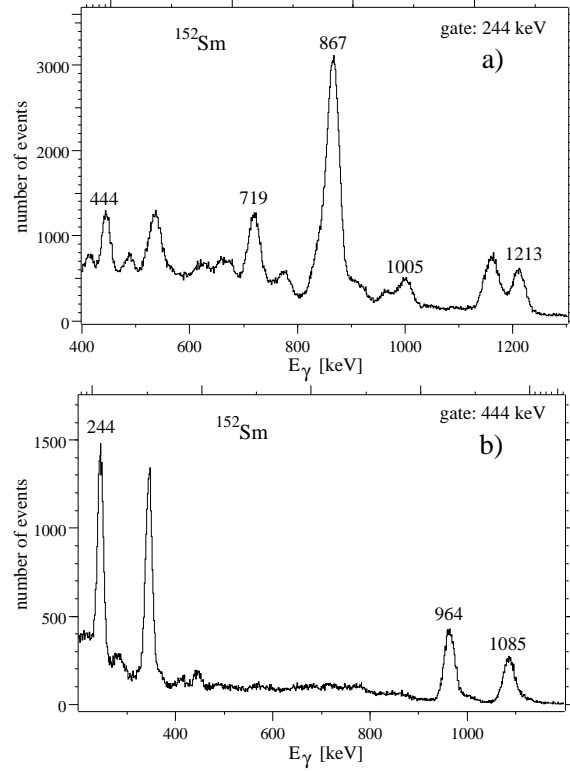


Figure 4.14: Coincidence γ -ray spectra of the 244 keV (a) and the 444 keV (b) transitions in ^{152}Sm .

The very particular of the ^{152}Eu source is that beside the continuously discussed case of ^{152}Gd also the excited ^{152}Sm isotope is generated. As can be seen in Figs. 4.13 and 4.14, at least three transitions are in coincidence with the 244 keV and the 444 keV transitions which therefore can be used as additional reference energy gates of the system. For every energy combination of coincident transitions, the centroid difference $\Delta C(E_\gamma)_{E_{\text{ref}}} = C(E_\gamma)_{\text{stop}} - C(E_\gamma)_{\text{start}}$ is measured, corrected for known lifetimes according to Eq. (3.7) and plotted in the centroid difference diagram, as presented in Fig. 4.15. Note that the measured PRD of the combination 444-244 keV is used twice, namely at 244 keV and at 444 keV but with opposite signs (mirror symmetry of PRDs). The PRDs (data points) with common reference energy are connected to illustrate the parallel shift of the PRD curve obtained for different reference energies. As explained in the previous section, this shift can be derived from the PRD curve itself. Therefore, the data points with common reference energies were shifted in parallel to fit a single smooth PRD curve. Fig. 4.16a shows the result of this procedure, which is

extremely sensitive. Data points which are falsified by background contributions are directly identified due to abnormal deviation from the smooth monotonic time-walk characteristics. In this case, data points in the energy region of 1000 keV-1100 keV were omitted (see also Fig. 4.15). It can be seen in Fig. 4.1 that in this region several γ -rays are overlapped to form a broad “peak”. In such cases, the contaminating γ -ray transitions cannot be separated and thus contribute to the time spectra. This can be avoided using an additional trigger, as for example the γ - γ - γ method proposed by N. Mărginean et al. [45].

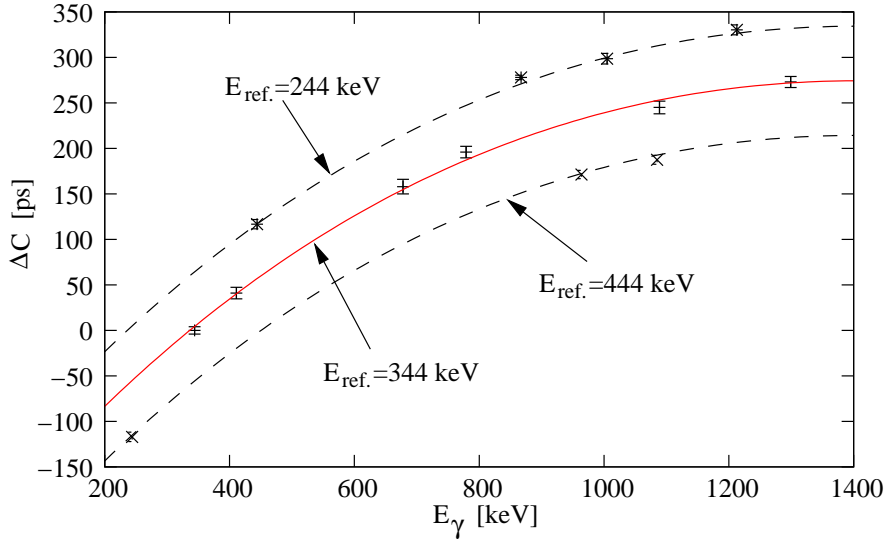


Figure 4.15: PRDs for different reference energy gates in dependence on gated γ -ray energy. The 344 keV gated PRDs were fitted using Eq. (4.13). For different reference energies, the PRD curves are shifted in parallel as indicated by the dashed curves. The shift was derived from the 344 keV gated PRD curve (solid curve).

The data points shown in Fig. 4.16a were fitted using

$$\Delta C(E_\gamma) = \frac{a}{\sqrt{b + E_\gamma}} + cE_\gamma + d, \quad (4.13)$$

with resulting fit parameters of

fit 1:

$$\begin{aligned} a &= (-826391 \pm 111713) \text{ ps}\sqrt{\text{keV}} && (13.5\%) \\ b &= (3316.85 \pm 357.39) \text{ keV} && (10.8\%) \\ c &= (-1.28444 \pm 0.00944) \text{ ps/keV} && (1\%) \\ d &= (14104.7 \pm 1194.7) \text{ ps} && (8.5\%). \end{aligned}$$

The error bars shown in Fig. 4.16b result from statistics and include uncertainties of the known lifetimes taken from Ref. [43]. No error is taken into account

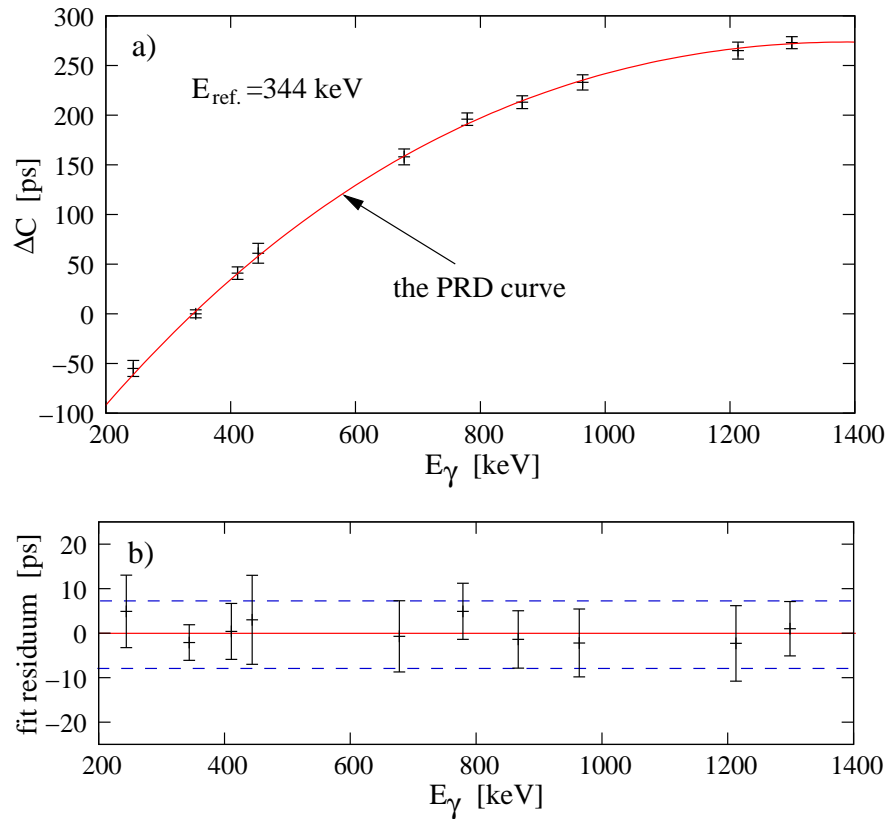


Figure 4.16: a: The combined time-walk characteristics (the PRD curve) of the γ - γ fast timing setup obtained using the ^{152}Eu source. b: Data point deviation to the fit (fit 1). The dashed lines indicate the 2σ deviation corresponding to 8 ps.

for the parallel shift of the data points, as the induced error of this procedure is negligibly small compared with the other errors. The total error of 8 ps for the determination of the PRD curve is derived from the fit residuum shown in Fig. 4.16b and corresponds to a 2σ deviation. For $240 \text{ keV} < E_\gamma < 1300 \text{ keV}$, the resulting limitation of the lifetime determination in this experiment is only 4 ps.

For comparison, the same data points were also fitted using

$$\Delta C(E_\gamma) = \frac{a'}{b' + E_\gamma} + c'E_\gamma + d', \quad (4.14)$$

with parameter values of:

fit 2:

$$\begin{aligned} a' &= (-260697000 \pm 39344200) \text{ ps keV} && (15.1\%) \\ b' &= (8811.6 \pm 330.7) \text{ keV} && (3.8\%) \\ c' &= (-2.53476 \pm 0.19872) \text{ ps/keV} && (7.9\%) \\ d' &= (29349.4 \pm 2956.48) \text{ ps} && (10.1\%). \end{aligned}$$

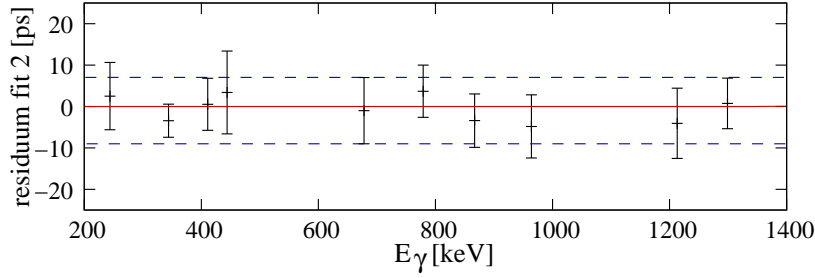


Figure 4.17: Residuum of the fit using Eq. (4.14) with parameters of fit 2. The quality of the fit is comparable to the fit of Eq. (4.13) shown in Fig. 4.16.

As illustrated in Figs. 4.16b, 4.17 and 4.18, no significant difference between the two performed fits can be observed so far. The effect of the deviation between the two fits on the lifetime determination is smaller than 1 ps. Thus, Eq. (4.13) can be approximated by Eq. (4.14), assuming Eq. (4.13) to be the correct analytical expression. This means in particular that the results of the prompt curve measurements presented in Chapter 3.1 and those published in Refs. [18, 20, 21] in which Eq. (3.5) was used as calibration function are in agreement with the observations made in this work. Assuming the linear term of Eqs. (4.13-4.14) to vanish in certain cases, these equations are identical to the derived CFD time-walk characteristics defined by Eq. (2.15).

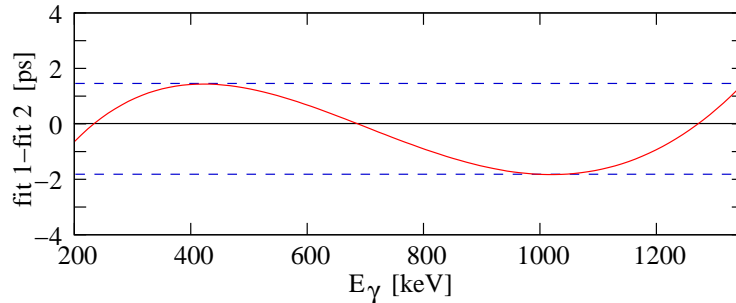


Figure 4.18: Deviation between the calibration function of Eq. (4.13) with parameters of “fit 1” and Eq. (4.14); “fit 2”.

A particular aim of this work is to calibrate the PRD curve within the largest possible dynamic range. Using the setup described in this section, investigations on two further standard γ -ray sources were performed. Fig. 4.19 shows the partial level scheme of ^{214}Po , one daughter in the decay chain of the standard ^{226}Ra source. Seven γ -ray transitions are in coincidence with the 609 keV ground state transition, as can be seen in Fig. 4.20. The lifetime of the first 2^+ state in ^{214}Po has not been measured yet. For a collective E2 transition with energy of 609 keV, the lifetime was calculated to be smaller than 10 ps (see Section 4.6).

Time distributions were generated and centroid differences for seven energy combinations in ²¹⁴Po were measured without subtracting contributions of any background. The results were plotted in the centroid difference diagram and compared with the calibrated PRD curve (fit 1) obtained using the ¹⁵²Eu source, as presented in Fig. 4.21. The calibrated PRD curve was shifted in parallel to cross the energy axis at 609 keV. This shift corresponds to PRD(344 – 609) = –129(8) ps obtained using Eq. (4.13) and parameters of fit 1. For $E_\gamma > 1000$ keV, the 609 keV gated centroid differences are consistent with the PRD curve derived for the reference energy of 609 keV. The delay of the data points below 1000 keV can be explained by the large Compton background underneath the full energy peaks of the interest, as can be seen in Fig. 4.20. A background correction procedure for the MSCD method was also developed and is described in Appendix A.

Using Eq. (4.13) and the parameters of fit 1, it follows from the PRD curve:

$$\text{PRD}(1120 - 609) = 126(8) \text{ ps.} \quad (4.15)$$

The 1120 keV γ -ray transition has the largest peak-to-background ratio of about 15. Neglecting background contributions, the measured centroid difference corresponds to

$$\Delta C(1120 - 609) = 124(3) \text{ ps} \quad (4.16)$$

and the lifetime of the first 2⁺ state in ²¹⁴Po is obtained using

$$\tau = \frac{\Delta C(\Delta E_\gamma) - \text{PRD}(\Delta E_\gamma)}{2} = -1(5) \text{ ps} \implies \tau \leq 4 \text{ ps,} \quad (4.17)$$

according to Eq. (3.7). In regard to nuclear structure studies, the expected and reasonable result is discussed in Section 4.6.

To investigate the low-energy PRD, the standard ¹³³Ba source was used which provides a γ -ray with energy of only 53 keV. As can be seen from the partial level scheme of ¹³³Cs shown in Fig. 4.22, the 53 keV transition feeds a state whose lifetime is known. The 303 keV transition is the strongest decay of this state. Fig. 4.23 shows coincidence γ -ray spectra with two low energy transitions at 53 keV and 161 keV; the 81 keV transition is not of interest as $\tau(81 \text{ keV}) = 9.08(3)$ ns. For this work, also the known lifetime of the second 5/2⁺ state at 161 keV was measured. The results of the MSCD analysis on ¹³³Cs are presented in Figs. 4.24 and 4.25.

Considering the PRD fit 1 using Eq. (4.13) valid for 244 keV < E_γ < 1300 keV, the shift of the PRD curve for $E_{\text{ref.}} = 303$ keV is given by

$$\text{PRD}(344 - 303) = 25(8) \text{ ps.} \quad (4.18)$$

The PRD for the combination 344-53 keV can be written as

$$\begin{aligned} \text{PRD}(344 - 53) &= \text{PRD}(344 - 303) + \text{PRD}(303 - 53) \\ &= \text{PRD}(344 - 303) + [\Delta C(303 - 53) + 2\tau], \end{aligned} \quad (4.19)$$

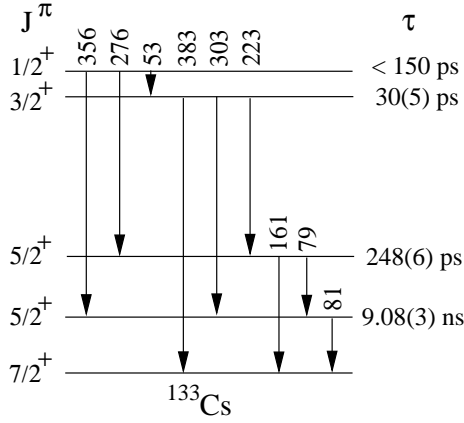


Figure 4.22: Partial level scheme of ^{133}Cs obtained after electron capture decay of ^{133}Ba . J^π , E_γ and τ from Ref. [43].

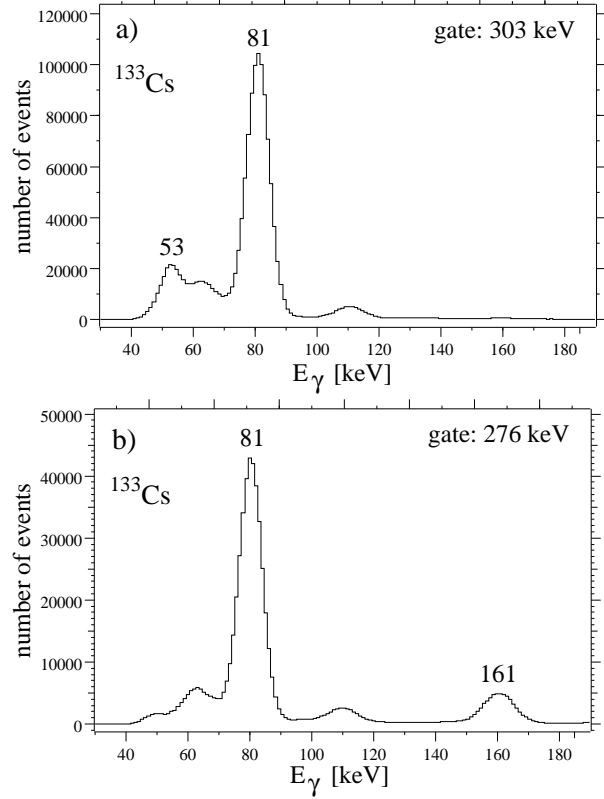


Figure 4.23: Coincidence γ -ray spectra of the 303 keV (a) and the 276 keV (b) transitions in ^{133}Cs .

according to Eq. (3.7), as the energy of the decay transition is larger than that of the feeder in the case of the 53 keV \rightarrow 303 keV cascade [$\Delta E_\gamma < 0$ as defined by Eq. (3.6)]. The evaluation results in

$$\text{PRD}(344 - 53) = [25(8) + 92(8) + 60(10)] \text{ ps} = 177(16) \text{ ps} \quad (4.20)$$

and which can be used as additional PRD for the calibration of the PRD curve [for the reference energy of 344 keV, the data point at 53 keV is: $\text{PRD}(53 - 344) = -177(16) \text{ ps}$]. The same procedure was applied to the data points for $E_\gamma > 1000 \text{ keV}$ shown in Fig. 4.21. The final result of the PRD curve determination for $50 \text{ keV} < E_\gamma < 1510 \text{ keV}$ is shown in Fig. 4.26.

The final PRD curve was obtained by a fit of the data points shown in Fig. 4.26a using Eq. (4.13) with resulting parameters of:

fit 3:

$$\begin{aligned} a &= (-734770 \pm 55841) \text{ ps}\sqrt{\text{keV}} && (7.6\%) \\ b &= (3271.56 \pm 197.78) \text{ keV} && (6.1\%) \\ c &= (-1.13006 \pm 0.00592) \text{ ps/keV} && (0.5\%) \\ d &= (12612.6 \pm 596.4) \text{ ps} && (4.8\%). \end{aligned}$$

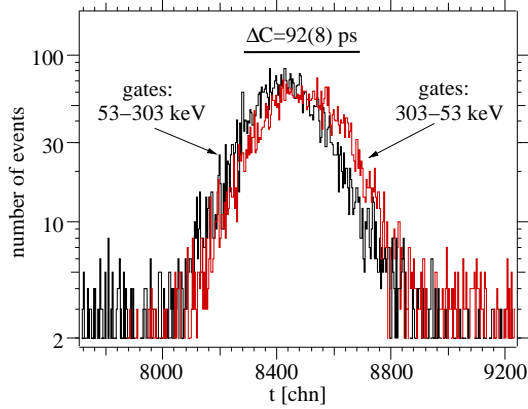


Figure 4.24: The two time distributions of the 53 keV \rightarrow 303 keV cascade in ^{133}Cs .

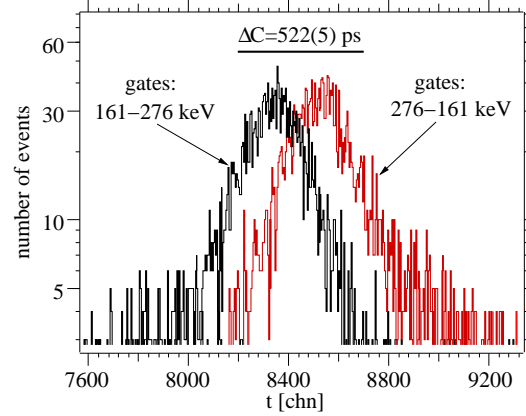


Figure 4.25: The two time distributions of the 276 keV \rightarrow 161 keV cascade in ^{133}Cs .

Within the dynamic range of $50 \text{ keV} < E_\gamma < 1510 \text{ keV}$, the calibration function of Eq. (4.13) fits every data point. The total error of the PRD curve determination corresponding to two standard deviations is only 8 ps ($\propto 2\Delta\tau$), as illustrated in Fig. 4.26b. Again, Eq. (4.14) was also used to fit the data for comparison. The fit parameters obtained are:

fit 4:

$$\begin{aligned}
 a' &= (-56076300 \pm 5583190) \text{ ps keV} && (10\%) \\
 b' &= (5167.12 \pm 293.84) \text{ keV} && (5.7\%) \\
 c' &= (-1.28815 \pm 0.00512) \text{ ps/keV} && (0.4\%) \\
 d' &= (10621.7 \pm 471.0) \text{ ps} && (4.5\%).
 \end{aligned}$$

This result is illustrated by the fit residuum presented in Fig. 4.27. Again, no significant differences between the two fits are observed, as illustrated in Fig. 4.28. In conclusion, the results presented in Chapter 3.1 and those published in Refs. [18, 20, 21] are highly accurate. However, the deviation at 53 keV is worse for the case of fit 4 using Eq. (4.14), as can be seen in Fig. 4.27 compared with Fig. 4.26b. It is reasonable to assume that Eq. (4.13) approximates the true PRD curve more accurately, as it coincides with the physically derived CFD timing of Eq. (2.15) for the case of vanishing linear factor c which seems to be dependent on the shaping delay time t_d .

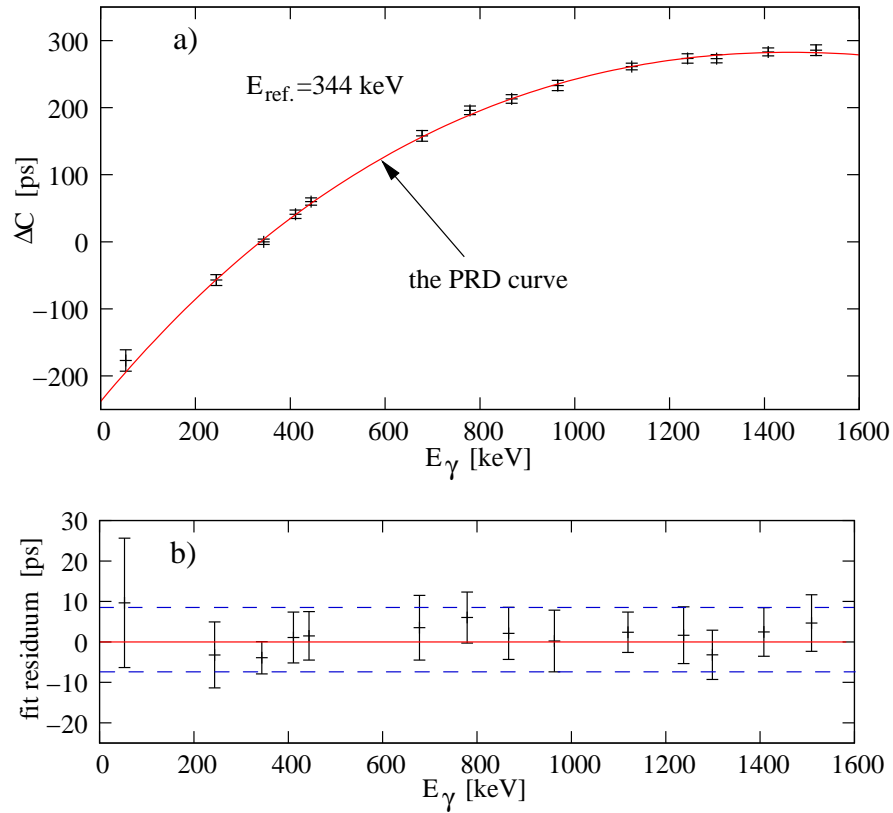


Figure 4.26: a: The PRDs after corrections for shifts due to different reference energy gates in relation to the reference energy of 344 keV. The data points are fitted by the solid PRD curve using Eq. (4.13) which represents the combined γ - γ time-walk characteristics of the setup. b) Fit residuum represented by the dashed lines corresponding to two standard deviations (σ).

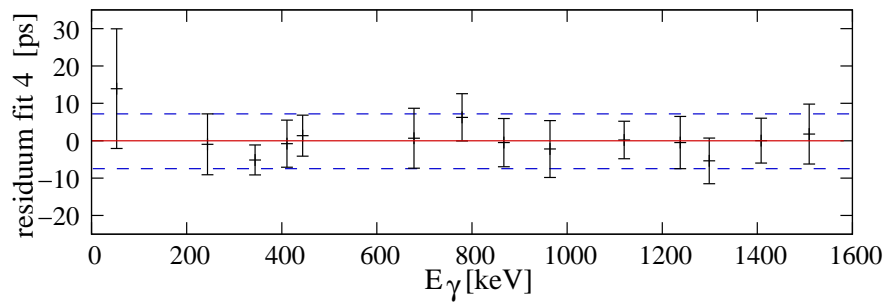


Figure 4.27: Residuum of the fit using Eq. (4.14) with parameters of fit 4.

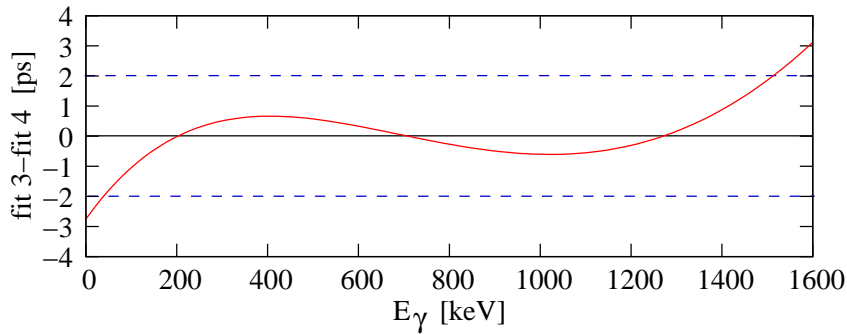


Figure 4.28: Deviation between the calibration function of Eq. (4.13) with parameters of “fit 3” and Eq. (4.14) with “fit 4” parameters.

The result of this PRD curve measurement is remarkable: The shape of the PRD curve presented in Fig. 4.26a differ considerably from the expected one, which should have a shape like those presented in Figs. 3.1 and 4.6b. However, Eq. (4.13) is able to describe these two very different PRD curves. Many other functions with four and more parameters were tried, but only Eq. (4.13) is able to fit every data point within the full dynamic range.

Now, lifetimes can be measured using low-energy events. The result of the MSCD analysis for the 161 keV state in ¹³³Cs is already presented in Fig. 4.25. From the final PRD curve (fit 3) shown in Fig. 4.26a, it follows

$$\begin{aligned} \text{PRD}(276 - 161) &= 75(8) \text{ ps} \\ \implies \tau &= \frac{\Delta C(276 - 161) - \text{PRD}(276 - 161)}{2} = 224(10) \text{ ps.} \end{aligned} \quad (4.21)$$

This result slightly differ from the stated lifetime of 245(6) ps [12, 43]. The lifetime determination using the slope or the deconvolution method was not practicable due to low statistics. Also, the time resolution for the energy combination 276-161 keV is about $\delta t \approx 350$ ps. A contribution from the Compton background to the time spectra also cannot be excluded.

Another lifetime in ²¹⁴Bi could also be measured. The first excited state at 53 keV in ²¹⁴Bi, another daughter of the ²²⁶Ra source, was already measured by Z. Berant et al., but only an upper limit of $\tau < 144$ ps could be assigned [46]. A simplified level scheme of ²¹⁴Bi is shown in the inset of Fig. 4.29 and the result of the MSCD analysis is presented in Fig. 4.30. The strong 53 keV decay transition provides very good peak-to-background ratio and virtually no background contribution to the time distributions can be observed. The shift of the PRD between 53 keV and 241 keV derived from the final PRD curve (fit 3) is $\text{PRD}(241 - 53) = 133(15)$ ps and thus the lifetime of the first excited state in ²¹⁴Bi is measured to be

$$\tau = \frac{\Delta C(241 - 53) - \text{PRD}(241 - 53)}{2} = -5(8) \text{ ps} \implies \tau \leq 3 \text{ ps.} \quad (4.22)$$

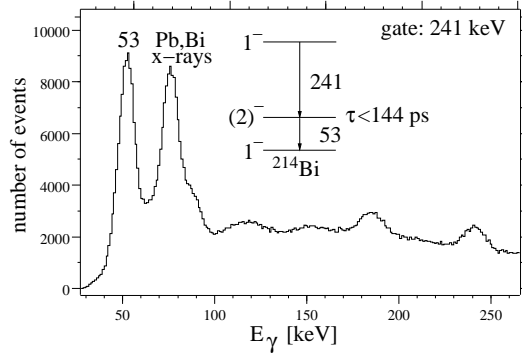


Figure 4.29: Coincidence γ -ray spectrum of the 241 keV transition in ^{214}Bi . Inset: cascade of the interest and lifetime from Ref. [43].

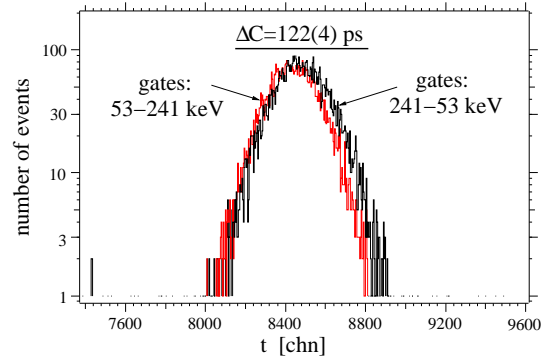


Figure 4.30: The two time distributions of the 241 keV \rightarrow 53 keV cascade in ^{214}Bi . Note the symmetric time spectra with FWHM of \approx 680 ps.

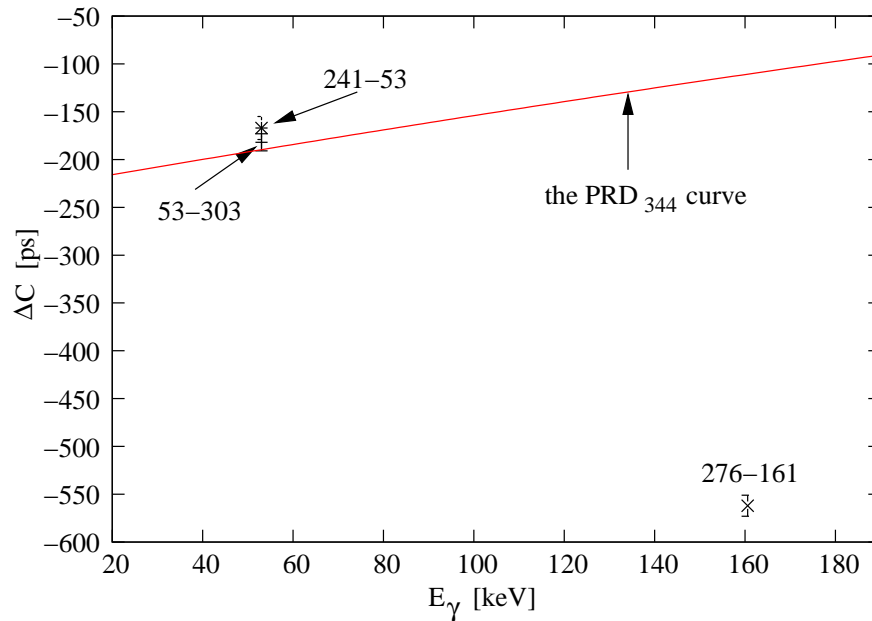


Figure 4.31: Centroid differences of indicated energy combinations (cascades). The original data were corrected for the reference energy gate of 344 keV. The shift between the data points and the PRD curve corresponds to twice the lifetime of the intermediate state.

Considering Fig. 4.30, the time spectra are almost identical to a Gaussian distribution. Also this reasonable result is used in Section 4.6 for nuclear structure studies. The last two lifetime results are presented graphically in Fig. 4.31. There, the data were corrected for the reference energy gate of 344 keV, as demonstrated by Eqs. (4.18-4.19). The PRD indicated with 53-303 was used to calibrate the PRD curve represented by the solid line. The derived centroid difference of the 241-53 keV cascade is slightly above the PRD curve, but still in agreement within the statistical uncertainties. As practically no background contribute to the time spectra of the 241-53 keV cascade, the result of this lifetime determination given by Eq. (4.22) is not underestimated. A larger lifetime would shift the centroid difference significantly below the PRD curve, like the data point of the 276-161 keV cascade. This new upper limit for the lifetime of the state at 53 keV in ^{214}Bi is very useful for future PRD curve measurements.

4.4 The dynode timing with the XP20D0 PMT

In the previous section it was shown that the time-walk characteristics can differ considerably when using different PMT operation modes. The requirement of adequate and especially linear PMT output signals makes the use of the XP20D0 difficult. An almost linear operation (non-linearity $< 1\%$) can be achieved, but only for voltages ≤ 750 V. At this mode, the pulse height of the dynode output for events with $E_\gamma < 80$ keV is too small for standard pulse height analysis using a preamplifier-amplifier-ADC² system. But, the larger anode signal can be used for this purpose. The positive dynode pulse then is used for fast timing by sending it directly through a timing filter amplifier (TFA) which provides an amplified negative pulse for the CFD, as illustrated in Fig. 4.32. This dynode timing technique is reported to provide better time resolution by factor of 1.2 [36]. However, the dynode timing technique applied on the XP20D0 PMT has not been performed before this work.

The setup of this dynode timing experiment consisted of two IKP $\text{LaBr}_3(\text{Ce})$ detectors (including XP20D0) operated in linear mode. The positive dynode pulses were send directly to a TFA model Ortec 579. To conserve the detector rise time, the integration time constant of the TFA was set to zero. The inverted and amplified dynode pulses were differentiated with time constant 50 which provided very smooth TFA output pulses with large amplitudes, as presented in Fig. 4.33. A gain in amplitude of factor 10 was achieved. Of course, also the noise generated by the electronics of the PMT is amplified. Therefore, the CFD threshold was set to -80 mV for avoiding the zero comparator to trigger on noise. A CFD shaping delay time of $t_d = 5$ ns was used for this experiment.

The PMT anode output was used for the slow energy circuitry. The anode amplitude is large enough to record γ -rays down to about 20 keV even in the low PMT voltage linear mode. No significant differences in energy response and energy resolution could be observed between the anode and the dynode pulses.

²ADC: Analogue to digital converter used in multi-channel analyzers

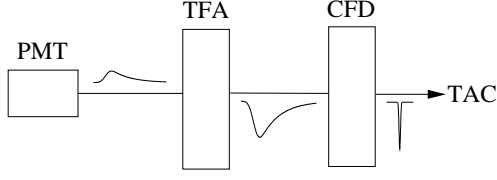


Figure 4.32: Schematic drawing of the electronics setup for dynode timing.

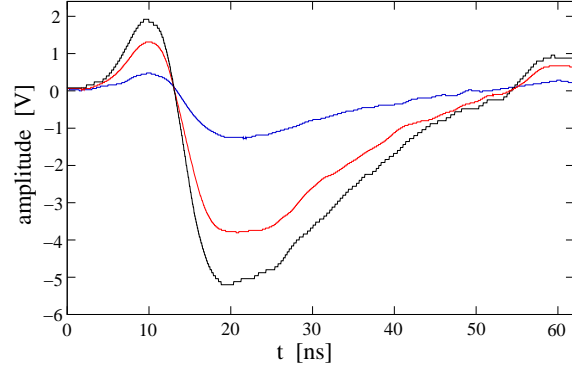


Figure 4.33: The shaped dynode pulses of different amplitudes at the TFA output.

A MSCD analysis was performed to determine the combined γ - γ time-walk characteristics of the setup. In a first step, the ^{152}Eu γ -ray source provided PRDs to calibrate the PRD curve for the energy region $240 \text{ keV} < E_\gamma < 1300 \text{ keV}$, as described in Section 4.2.1. Secondly, the ^{133}Ba γ -ray source was used to provide a PRD at 53 keV. The results of the MSCD analysis on ^{133}Ba are shown in Figs. 4.34 and 4.35. From the PRD curve calibrated in the first step, the PRD for the energy combination 344-303 keV was derived to be

$$\text{PRD}(344 - 303) = 27(8) \text{ ps}. \quad (4.23)$$

According to Eq. (4.19), the value of the measured centroid difference for the combination 53-303 keV is corrected to provide the PRD at 53 keV as

$$\text{PRD}(344 - 53) = [27(8) + 610(5) + 60(10)] \text{ ps} = 697(14) \text{ ps}. \quad (4.24)$$

The result of this PRD curve measurement is presented in Fig. 4.36. The PRD curve was obtained by fitting the data points using Eq. (4.13) with parameters of:

a	$=$	(-7402.62 ± 137.96)	$\text{ps}\sqrt{\text{keV}}$	(1.87%)
b	$=$	(-7.85554 ± 0.75812)	keV	(9.65%)
c	$=$	$(-0.28281 \times 10^{-3} \pm 6.58201 \times 10^{-3})$	ps/keV	(2327%)
d	$=$	(404.31 ± 8.87)	ps	(2.19%)

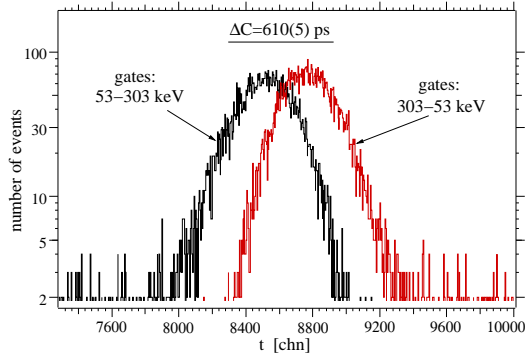


Figure 4.34: The two time distributions of the 53 keV \rightarrow 303 keV cascade in ^{133}Cs obtained using the dynode timing technique.

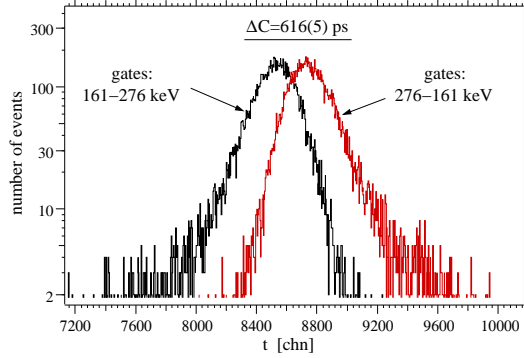


Figure 4.35: The two time distributions of the 276 keV \rightarrow 161 keV cascade in ^{133}Cs obtained using the dynode timing technique.

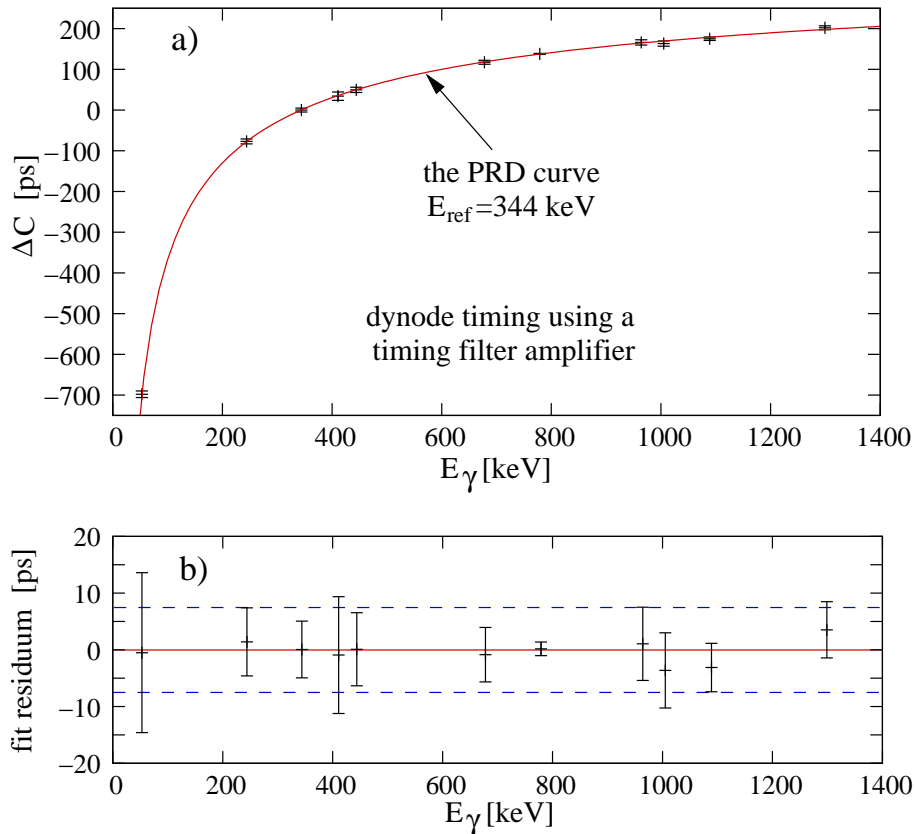


Figure 4.36: a: The PRD curve obtained for the dynode timing in application with the PMT linear operation mode. For both CFDs, a shaping delay time of $t_d = 5$ ns was used. b: The residuum of the calibration function of Eq. (4.13) is indicated by the dashed lines.

The total error for the determination of the PRD for any energy combination in the range of $53 \text{ keV} < E_\gamma < 1510 \text{ keV}$ is 8 ps. The PRD curve of this experiment resembles to the prompt curves shown in Figs. 3.1 and 4.8, where a linear operation of the PMT was applied like in the experiment presented here. It is remarkable that the linear factor c of Eq. (4.13) nearly vanishes in cases where a short CFD shaping delay time of $t_d \approx 5 \text{ ns}$ is used. The influence of the linear term parameter c on lifetime measurement is found to be smaller than 3 ps for $E_\gamma < 1500 \text{ keV}$. This is a strong indication for the time-walk of a fast timing setup is defined by the CFD time-walk characteristics described by Eq. (2.15). However, below 300 keV the time-walk rapidly increases non-linearly in contrary to the nearly linear time-walk down to 53 keV observed for the non-linear PMT operation mode (see Fig. 4.26a).

Lifetime measurements on ^{133}Cs , ^{214}Bi and ^{214}Po have been performed to test the calibrated PRD curve. For the 161 keV state in ^{133}Cs , the PRD of the combination 276-161 keV is:

$$\text{PRD}(276 - 161) = 146(8) \text{ ps.} \quad (4.25)$$

It follows from Fig. 4.35:

$$\tau = [\Delta C(276 - 161) - \text{PRD}(276 - 161)]/2 = 235(10) \text{ ps.} \quad (4.26)$$

This result is in very good agreement with the lifetime of 245(6) ps measured via the ATD method [12]. Fig. 4.37 shows one time spectrum of the 276 keV \rightarrow 161 keV cascade, which has a significant slope thanks to high statistics. The lifetime of $\tau = 233(15) \text{ ps}$ could be extracted by the deconvolution method and confirms the result obtained using the MSCD method.

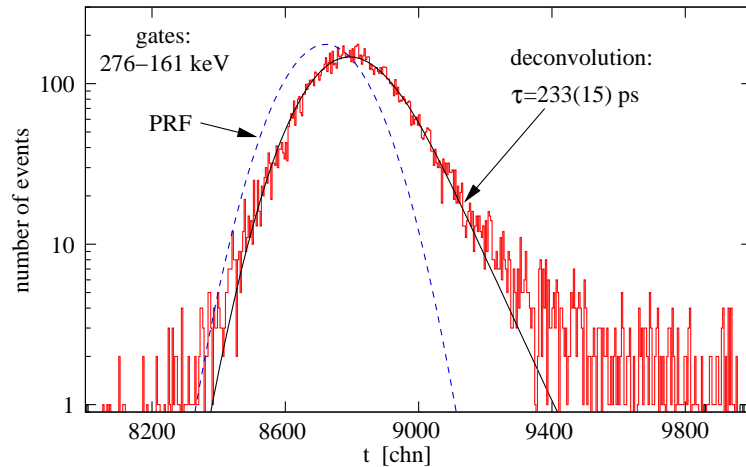


Figure 4.37: Time spectrum of the γ -ray cascade connecting the 161 keV state in ^{133}Cs . The fit of the time spectrum presented as a solid line was performed using Eq. (2.1). The FWHM of the deconvoluted PRF corresponds to a time resolution of $\delta t \approx 350 \text{ ps}$.

Further results of the MSCD analysis are presented in Figs. 4.38 and 4.39. From the calibrated PRD curve it follows for the first excited state in ²¹⁴Bi:

$$\begin{aligned} \text{PRD}(241 - 53) &= 617(15) \text{ ps} \\ \implies \tau &= [\Delta C(241 - 53) - \text{PRD}(241 - 53)]/2 = -7(9) \text{ ps} \\ \implies \tau &\leq 2 \text{ ps.} \end{aligned} \quad (4.27)$$

Analogously, it follows for the first excited state in ²¹⁴Po:

$$\begin{aligned} \text{PRD}(1120 - 609) &= 80(8) \text{ ps} \\ \implies \tau &= [\Delta C(1120 - 609) - \text{PRD}(1120 - 609)]/2 = 1(5) \text{ ps} \\ \implies \tau &\leq 6 \text{ ps.} \end{aligned} \quad (4.28)$$

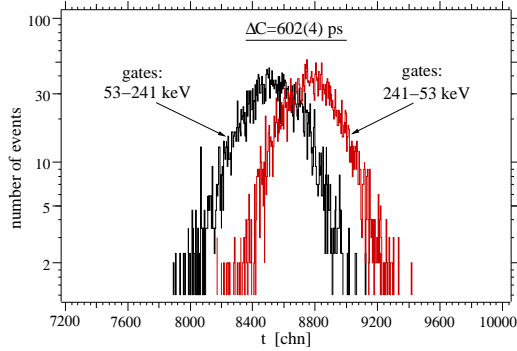


Figure 4.38: The two time distributions of the 241 keV \rightarrow 53 keV cascade in ²¹⁴Bi obtained using the dynode timing technique.

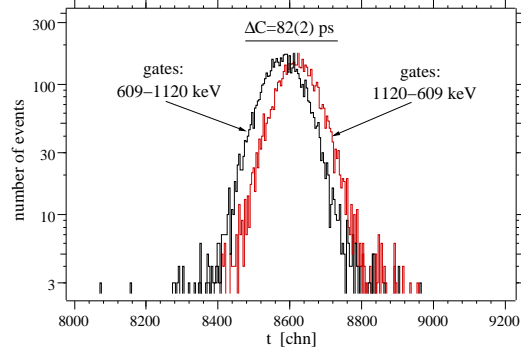


Figure 4.39: The two time distributions of the 1120 keV \rightarrow 609 keV cascade in ²¹⁴Po obtained using the dynode timing technique.

Although the PRD curves presented in this work differ dramatically, the lifetime results obtained are in excellent agreement. These reliable and precise results are demonstrating that the MSCD method provides a powerful tool for picosecond lifetime measurements.

A better timing compared with the standard anode timing technique cannot be confirmed by this work. Considering Fig. 4.38, the FWHM of the time spectra for the energy combination 241-53 keV is 950 ps. This is about 1.4 times worse than the result of 680 ps for the anode timing technique reported in Section 4.2 (Fig 4.30). At higher energies, the time resolution gets better but is still worse by factor of about 1.2 comparing with the anode timing. Also, when considering the total dynamic range, the time-walk obtained using the anode timing technique with slightly non-linear PMT operation is reduced by factor of nearly 2.

4.5 Time-walk using different timing conditions

In this section the change in the shape of the PRD curve is investigated in dependence on the applied PMT operation voltage and the CFD shaping delay time t_d . Such PRD curve measurements were performed using two IKP LaBr₃(Ce) detectors. The aim was to obtain the combined time-walk characteristics in a wide dynamic range in order to compare the PRD curves and resulting lifetimes. In any case, the voltages of both PMTs were adjusted to deliver almost identical transfer functions, i.e. same amplitude versus energy characteristics at about the same operation voltage. Also, the same shaping delay time was used for both CFDs of the setup. Standard γ -ray sources were used and the PRD calibration procedure was applied, as described in Sections 4.2.1 and 4.3. The result of the time-walk characteristics measurements are presented graphically in Fig. 4.40. Results of lifetime determinations using the MSCD method are listed in Tab. 4.1.

Similar prompt curve analyzes were performed using a XP2020 PMT in combination with the LaBr₃(Ce) scintillator. In that experiment, the stop detector consisted of the XP20D0 PMT. Therefore, only the prompt curves obtained using the XP2020 PMT are presented in Fig. 4.41. The data points were obtained using the 344 keV decay transition in ¹⁵²Gd as the reference timing signal.

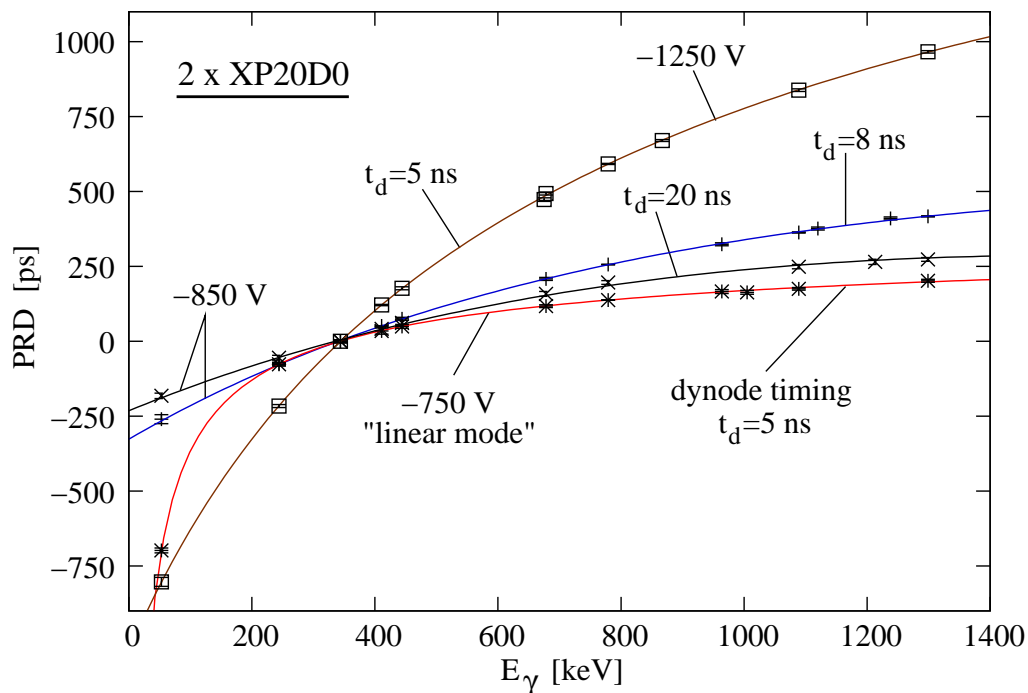


Figure 4.40: The combined time-walk characteristics of the two detector timing system comprising the XP20D0 PMTs. The data points were obtained using different PMT voltages and CFD shaping delay times t_d . The result of two PRD curves were presented in detail in Sections 4.2.1 and 4.3. For all cases, Eq. (4.13) was used to calibrate the PRD curves shown as solid lines.

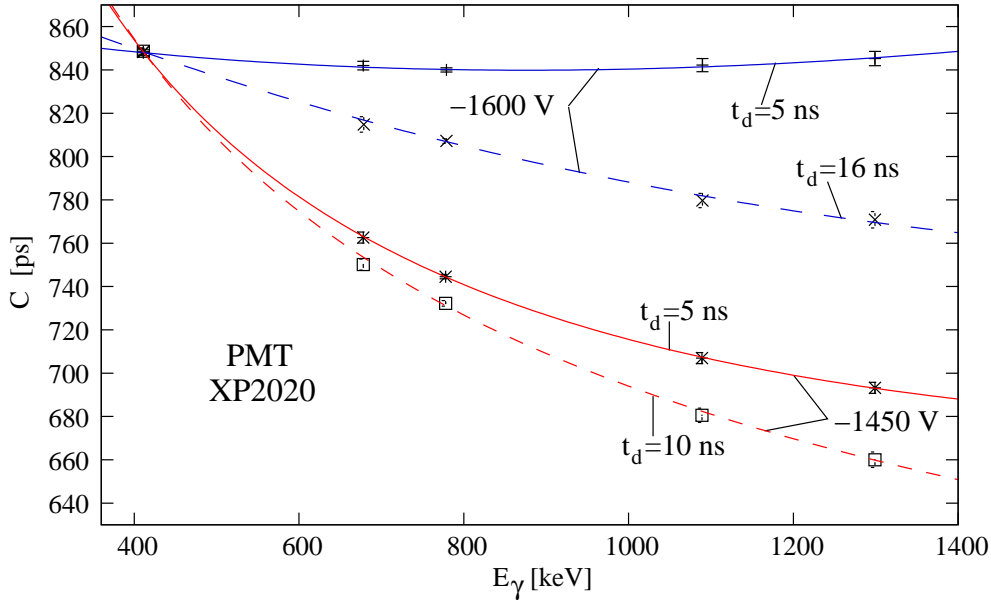


Figure 4.41: Time-walk characteristics of the $\text{LaBr}_3(\text{Ce})+\text{XP2020}$ detector assembly obtained using different PMT voltages and CFD shaping delay times t_d . The data points were shifted in parallel to fit the centroid at 411 keV as a normalization point. For all cases, the data points were fitted using Eq. (4.13).

As can be seen in Fig. 4.40, for the linear PMT operation mode of the XP2020 the typical shape of the CFD time-walk characteristics is observed. In any case, Eq. (4.13) is able to describe the PRD curve within the total dynamic range. For the case of using short CFD shaping delay times (e.g. $t_d = 5$ ns), the factor c of the linear term of Eq. (4.13) is negligibly small and therefore, the PRD curve coincides with the CFD time-walk characteristics defined by Eq. (2.15). The similarity of the calibration function [Eq. (4.13)] with the energy dependency of the energy resolution defined by Eq. (4.4) for the non-linear operation mode is impressive. These observations lead to the conclusion that indeed, the time-walk is a result of the statistical amplitude variations. Although a TFA was used to provide large amplitudes in the linear operation mode, the low statistics of secondary electrons at the PMT dynode results in a large time-walk for energies below 300 keV. However, for larger energies, the smallest time walk is observed for the linear PMT operation. Applying slightly higher operation voltages and using the anode pulse which is produced by a larger number of secondary electrons, the time-walk for energies below 300 keV is considerably reduced. But, with increasing operation voltages, the time-walk also increases. This is due to increase in PMT response non-linearity leading to larger statistical fluctuations of the PMT output pulse height. The time-walk can furthermore be reduced when using a long CFD shaping delay time of e.g. 16-20 ns (TCF timing). A very interesting observation is that the factor c of the linear term of Eq. (4.13) increases with increasing CFD shaping delay time. These observations explain and confirm the results published in Refs. [18, 20], where PMT voltages of about -1200 V were applied and a short CFD shaping delay time of $t_d \approx 5$ ns was chosen.

For the XP2020 PMT the behavior of the time-walk characteristics is different. Although the PMT response of the XP2020 is linear in the range of -1400 V to -1900 V, the best time-walk was obtained at an intermediate operation voltage of about -1600 V. Probably, by proper selection of the CFD shaping delay time this very good time-walk characteristics can also be obtained at higher operation voltages. In contrary to the behavior of the XP20D0, the time-walk is reduced when using short CFD shaping delay times, thus for the ARC timing condition. This observation can be explained by the slightly different shape of the PMT output pulse compared with that of the XP20D0 PMT. The only observation common to the use of the XP20D0 is the increase of the linear term of the calibration function with increasing CFD shaping delay time, as can be seen in Fig. 4.41. This is an additional indication that the time-walk characteristics of the setup is defined by the CFD timing principle.

The lifetime results for three excited states obtained under different circumstances and applying the MSCD method are all consistent, as presented in Tab. 4.1. This demonstrates the high sensitivity of the newly developed MSCD method. For the second excited $5/2^+$ state in ^{133}Cs , the weighted average of the results gives a lifetime of $\tau(161 \text{ keV}) = 235(10) \text{ ps}$ and includes a possible systematic error of 5 ps due to very low background contributions. The result is in very good agreement with the experimental value of $\tau_{\text{Lit.}} = 245(6) \text{ ps}$ [12]. For the first excited 2_1^+ state in ^{214}Po , the largest upper limit of $\tau(609 \text{ keV}) \leq 6 \text{ ps}$ is used for further discussions in the next Section. A more conservative upper limit of $\tau(53 \text{ keV}) \leq 15 \text{ ps}$ will be used for the first excited 2_1^- state in ^{214}Bi . A possible systematic error of 10 ps is taken into account due to small background contributions to the 53-303 keV time spectra of ^{133}Cs used to calibrate the PRD at 53 keV.

Table 4.1: Results of lifetime measurements in ^{214}Bi (53 keV), ^{133}Cs (161 keV) and ^{214}Po (609 keV) using the MSCD method. The lifetimes were derived from the PRD curves shown in Fig. 4.40 and indicated with applied PMT voltage and CFD shaping delay time t_d . c is the fit parameter of the linear term of the calibration function as defined by Eq. (4.13).

voltage [V]	t_d [ns]	c [ps/keV]	$\tau(53 \text{ keV})$ [ps]	$\tau(161 \text{ keV})$ [ps]	$\tau(609 \text{ keV})$ [ps]
-750	5	< 0.01	≤ 2	235(10)	≤ 6
-850	20	1.22	≤ 3	224(10)	≤ 4
-850	8	0.38	≤ 8	241(12)	≤ 3
-1250	5	< 0.04	≤ 7	238(10)	≤ 3

4.6 The first excited state in ^{214}Po and ^{214}Bi

In this Section, the results presented in Tab. 4.1 are discussed with respect to previously published experimental results and nuclear structure calculations. The heavy isotopes ^{214}Po and ^{214}Bi lie close to the doubly magic nucleus ^{208}Pb ($Z=82$, $N=126$) which was found to be a “good closed-shell nucleus” [47]; the ground state binding energy is much stronger than neighboring lead isotopes and isotones. Based on the spherical shell-model [48], the ^{208}Pb core is assumed to be inert and the “active” particles are distributed in the single-particle orbits [47]. As a good approach, the independent particles are orbiting in a realistic spherical mean field $U(r)$ which includes spin-orbit coupling ($\mathbf{l} \cdot \mathbf{s}$) and an \mathbf{l}^2 term (e.g., the Woods-Saxon potential [49]). To account for nucleon-nucleon interactions, a residual interaction is added to the Hamiltonian of the independent particle model. The one-particle nuclei ^{209}Pb and ^{209}Bi are well known for their single-particle structures [50, 51]. The proton model space of the major shell $82 < Z \leq 126$ is $\pi(0h_{9/2}, 1f_{7/2}, 0i_{13/2}, 2p_{3/2}, 1f_{5/2}, 2p_{1/2})$ and the neutron model space for $N > 126$ is $\nu(1g_{9/2}, 0i_{11/2}, 0j_{15/2}, 2d_{5/2}, 3s_{1/2}, 1g_{7/2}, 2d_{3/2})$. For such multi- j -configuration, a so-called large-scale shell-model calculation in the complete model space for multi-particle nuclei is still infeasible [52]. However, shell-model calculations for $A=205$ - 212 using truncated model spaces have shown accurate reproduction of low-energy spectra [47, 52, 53]. Generally, the investigation of the residual interaction is hampered due to the limitations imposed by the truncation [54].

The odd-odd ^{214}Bi

In the work of Z. Berant et al. [46], the spins of the low-energy odd-parity states in ^{214}Bi were determined via angular correlation measurements and with respect to β^- -decay rates in $^{214}\text{Pb}(\beta^-)^{214}\text{Bi}$. Their approach to describe ^{214}Bi is based on systematics of Gamov-Teller β^- decay rates (the $\log f_0 t$ value) in the lead region with $A \geq 208$. They used a modified Kuo-Herling realistic interaction [55, 56] as residual interaction to perform truncated shell-model calculations in order to reproduce the low-energy odd-parity spectra of $^{210,212}\text{Bi}$ and especially the experimental β^- decay rates in $^{210,212}\text{Pb}(\beta^-)^{210,212}\text{Bi}$. An additional truncation to the results of these calculations using the generalized seniority model [57] provided the basis for an extrapolation to ^{214}Bi . To test the resulting eigenfunctions, they calculated the $M1$ transition strengths $B(M1 : 2_1^- \rightarrow 1_1^-)$ of the first excited 2_1^- state in $^{210,212,214}\text{Bi}$ and also β^- decay rates. The generalized seniority model was found to be a good approximation of the Kuo-Herling interaction [46] and experimental observables known so far could be reproduced well. However, the lifetime of the first excited 2_1^- state in ^{214}Bi could not be measured accurately using the ATD method [12] and only an upper limit of $\tau \leq 144$ ps could be established by Z. Berant et al. [46]. Their extrapolation from shell-model calculations for the 2_1^- state in ^{214}Bi yielded $\tau_{\text{SM}} = 17.2$ ps and $B(M1 : 2_1^- \rightarrow 1_1^-)_{\text{SM}} = 0.9$

W.u. [46] (W.u.: 1 Weisskopf unit is the strength for single-particle excitation).

The result obtained in this work is $\tau_{\text{exp}} \leq 15$ ps and thus $B(M1 : 2_1^- \rightarrow 1_1^-)_{\text{exp}} \geq 1.1$ W.u.³ which is close to the theoretical value derived in Ref. [46]. From this point of view, one is in favor to argue that ^{214}Bi is a good candidate for single-particle structures. As mentioned in Ref. [46], a large-scale shell-model calculation would be important for a more qualitative exploration of the results.

The even-even ^{214}Po

First experimental evidence for the quadrupole vibrational character of ^{214}Po is presented in the works of H. W. Taylor et al. [58, 59]. Based on γ - $\gamma(\theta)$ angular correlation measurements, they identified excited states corresponding to the equally spaced phonon spectrum of a collective quadrupole oscillator. As illustrated in Fig. 4.42, the first excited 2_1^+ state is considered as the one quadrupole phonon state of a 5-dimensional anharmonic quadrupole oscillator. The two phonon triplet ($4_1^+, 2_2^+, 0_2^+$) and one state (2_3^+) of the three phonon quintuplet were assigned due to identification of dominant $E2$ transitions to the first excited state. The excited states were populated by β^- -decay of ^{214}Bi which has the ground state spin of $J^\pi = 1^-$ [59]. The spin of the 1015 keV level is assigned most probable to $J^\pi = 4^+$, as this state is not directly populated by β -decay of the parent nucleus (third forbidden transition). However, a weak 406-609 keV γ -ray cascade was observed and the state established at 1015 keV is assumed to be populated by several unobserved γ -rays [59].

Within the geometrical anharmonic vibrator model [60], the energy spectrum of ^{214}Po can be reproduced. An equivalent description is given within the U(5) limit of the Interacting Boson Approximation (IBA) [61], which is presented in Chapter 5.1. Using a simple three parameter Hamiltonian [the CQF Hamiltonian of Eq. (5.20)], the spectrum of the quadrupole phonon states known so far is well reproduced, as presented in Fig. 4.42. The fit parameters obtained are:

$$c = 0.726, \zeta = 0.092 \text{ and } \chi = 0.$$

As explained in Chapter 5.1, $\zeta = 0$ and $\chi \in [0, -\sqrt{7}/2]$ geometrically corresponds to the spherical vibrator (the U(5) limit). The fitted value for ζ is close to zero and therefore, the variation of χ does not substantially change the results presented here. From the fit parameters obtained, the reduced $E2$ transition probability of the $2_1^+ \rightarrow 0_1^+$ transition simply called the $B(E2)$ value can be calculated (see Chapter 5.1). Using the effective boson charge of $e_B = 0.135 eb$, as determined in the mirror nucleus ^{200}Hg [62] (no other value is known for the region around $A=208$), the $E2$ transition strength for the 2_1^+ state results to $B(E2 : 2_1^+ \rightarrow 0_1^+)_{\text{IBA}} \approx 8$ W.u.. The upper limit $\tau_{\text{exp}} \leq 6$ ps for the lifetime of the 2_1^+ state determined in this work suggests $B(E2 : 2_1^+ \rightarrow 0_1^+)_{\text{exp}} \geq 21$ W.u. [using

³ $B(M1) = 3.176 \cdot 10^{-14} \frac{R_b}{1+\alpha_c} \frac{E_\gamma^{-3}}{\tau}$ in W.u. with relative branching ratio R_b , conversion coefficient α_c , E_γ in MeV and τ in s [75].

Eq. (5.12)], which clearly indicates a more collective transition. The results presented here confirm the observations made by H. W. Taylor et al. [58, 59] and are additional indications for the vibrational structure of ^{214}Po .

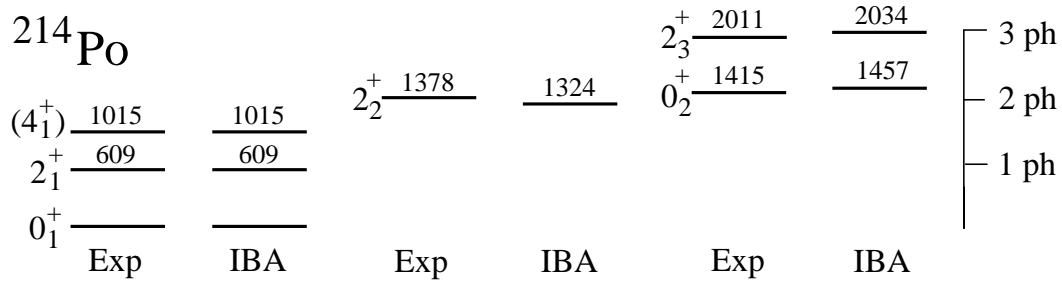


Figure 4.42: Simplified level scheme of ^{214}Po showing only the levels used to fit the energy eigenvalues of the CQF Hamiltonian of the IBA using Eq. (5.20). Experimental level energies and spins J^π from Ref. [59].

Chapter 5

In-beam lifetime measurements in W and Hf isotopes

The evolution of nuclear shape within the context of shape phase transitions in the even-even rare earth isotopes of the mass region $160 \leq A \leq 190$ have been subject of intensive studies [63]-[68]. In this mass region and far away from closed magic shells strong collectivity in even-even nuclei is observed, which manifests in strong $E2$ transition strengths $B(E2; 2_1^+ \rightarrow 0_1^+)$ with values of the order of a few hundreds of Weisskopf units (unit for single-particle excitation). In the geometrical model [69], the large $B(E2)$ value for the $2_1^+ \rightarrow 0_1^+$ $E2$ transition of nuclei around proton and neutron mid-shell ($Z=66$ and $N=104$) corresponds to a rotation of an axially symmetric deformed nucleus. The $B(E2; 2_1^+ \rightarrow 0_1^+)$ systematics of deformed nuclei is also described analytically in the $SU(3)$ limit of the Interacting Boson Approximation (IBA), proposed by A. Arima and F. Iachello in 1974 [70, 71]. This model is successful in describing low-lying collective quadrupole states for many even-even nuclei. Around proton and neutron mid-shell in the $160 \leq A \leq 190$ mass region, the typical excitation energy of the first excited 2_1^+ state is about 100 keV and the typical lifetime of the 2_1^+ state is about 1 ns which can be measured very precisely using the fast timing technique.

5.1 Nuclear structure considerations

As a microscopic model, working best for light nuclei, the nuclear shell-model is generally considered the fundamental model of the nucleus. However, for multi- j -configurations and increased numbers of valence nucleons, the dimension of the model space or the matrices in which the residual interaction must be diagonalized becomes enormous and calculations become impossible. Moreover, even for a few valence nucleons in few j -orbits, hundreds of states of a given J^π value have to be considered. This situation makes the physical interpretation of the results difficult. Thus, two macroscopic approaches to describe collective behavior in medium and heavy nuclei are discussed here.

The rigid rotor model for deformed nuclei

In the geometrical Bohr-Mottelson model [69], the radius for a nucleus is given in first order approximation by

$$R = R_0 \left[1 + \sum_{\mu} \alpha_{\mu} Y_{2\mu}(\theta, \phi) \right] \quad (5.1)$$

where $R_0 = 1.2A^{4/3}$ is the radius of the spherical nucleus of same volume. The $Y_{2\mu}$ are spherical harmonics of order 2 (for quadrupole deformation) and the α_{μ} are expansion coefficients. It is convenient to write

$$\alpha_0 = \beta \cos \gamma, \quad \alpha_1 = \alpha_{-1} = 0 \quad \text{and} \quad \alpha_2 = \alpha_{-2} = \beta \sin \gamma. \quad (5.2)$$

β represents the extent of quadrupole deformation, while γ gives the degree of axial asymmetry. For $\beta = 0$ and $\gamma = 0$, the nucleus is spherically symmetric. As one common convention (the Lund convention [72]) for the ranges of β and γ , one distinguishes between three shapes of deformation:

$$\begin{array}{lll} \beta > 0, & \gamma = 0^{\circ} & \text{axially symmetric prolate nucleus} \\ \beta > 0, & \gamma = -60^{\circ} & \text{axially symmetric oblate nucleus} \\ \beta > 0, & 0^{\circ} < \gamma < 60^{\circ} & \text{axially asymmetric nucleus} \end{array}$$

Using these shape parameters in the intrinsic coordinates, the Bohr-Mottelson Hamiltonian is given by [69]

$$\hat{H} = -\frac{\hbar^2}{2m} \left[\frac{1}{\beta^4} \frac{\partial}{\partial \beta} \left[\beta^4 \frac{\partial}{\partial \beta} \right] + \frac{1}{\beta^2 \sin(3\gamma)} \frac{\partial}{\partial \gamma} \left[\sin(3\gamma) \frac{\partial}{\partial \gamma} \right] \right] + \frac{\hbar^2}{2\Theta} \hat{R}^2 + V(\beta, \gamma). \quad (5.3)$$

Solutions to this Hamiltonian can be obtained dependent on the form of the potential $V(\beta, \gamma)$. A general form of the potential is based on an expansion in powers of β and $\cos(3\gamma)$ which allows to describe the named nuclear shapes as well as transition regions between these shapes including shape phase coexistence. The resulting Gneuss-Greiner Hamiltonian is known as the Geometric Collective Model (GCM) [73]. Considering the special case of a rigid potential in β and γ , centered at $\beta > 0$ and $\gamma = 0^{\circ}$ (prolate nucleus), Eq. (5.3) reduces to a rigid rotor:

$$\hat{H} = \frac{\hbar^2}{2\Theta} \hat{R}^2 = \frac{\hbar^2}{2} \sum_{i=1}^3 \frac{\hat{J}_i^2}{\Theta_i}. \quad (5.4)$$

Θ corresponds to the rigid body moment of inertia and \hat{R} is the rotational angular momentum operator. The general solution of Eq. (5.4) is given by [69]

$$\Psi_{JM} = \sqrt{\frac{2J+1}{16\pi^2}} [D_{JMK} \chi_K + (-1)^{J-K} D_{JM-K} \chi_{-K}]. \quad (5.5)$$

The rotation is described by the D matrix. χ_K is the wave function of an intrinsic excitation with the projection K of the nuclear spin J on the symmetry axis. Note that for $K = 0$, Eq. (5.5) allows only even J values. The diagonalization of the rotational Hamiltonian yields the energy eigenvalues as

$$E_{\text{rot}}(J) = \frac{\hbar^2}{2\Theta} [J(J+1) - K(K+1)], \quad J = K, K+1, K+2, \dots \text{ for } K \neq 0. \quad (5.6)$$

This expression describes the energy spacing of a rotational band based on intrinsic excitations. Like in spherical nuclei, the most low-lying band head energy in deformed nuclei are quadrupole vibrations (phonon excitation). The $K = 2$ mode called “ γ -vibration” represents the dynamic excursion from axial symmetry. For $K = 0$, the vibration is aligned along the symmetry axis and therefore preserves axial symmetry. In this rotation-vibration model [73], the excited $K = 0$ band head is often called “ β -vibration”, though the nature of the lowest $K = 0$ excitation is uncertain [74].

For the ground state in deformed even-even nuclei, the nuclear spin is $J^\pi = 0^+$ and thus $K = 0$. The rotational spectrum of the yrast states based on the ground state, also called the ground band, is given by the well known expression

$$E_{\text{rot}}(J) = \frac{\hbar^2}{2\Theta} J(J+1) \quad K = 0, \quad J \text{ even}. \quad (5.7)$$

This simple formula leads to one of the best signatures for rotational motion and deformation, which is the ratio of the level energies of the 4_1^+ and the 2_1^+ yrast states given by

$$R_{4/2} = \frac{E(4_1^+)}{E(2_1^+)} = 3.33 \quad \iff \quad \text{the rigid rotor model}. \quad (5.8)$$

The rotational concepts of Eqs. (5.6-5.7) are observed for the typically named example of the deformed ^{164}Er nucleus, as shown in Ref. [74], page 206.

Using the wave function of Eq. (5.5), the reduced $E2$ transition probability also called the $B(E2)$ value can be calculated. Assuming a fixed K (transitions within one band) one obtains [69]

$$B(E2 : J_i \rightarrow J_f) = \frac{5}{16\pi} e^2 Q_0^2 \langle J_i K 20 | J_f K \rangle^2, \quad (5.9)$$

where the expression in the bracket is the Clebsch-Gordan coefficient connecting J_i and J_f , e is the electric unit charge and Q_0 is the intrinsic quadrupole moment. However, the experimentally obtained so-called spectroscopic quadrupole moment Q_t needs to be transformed to the laboratory frame by [74]

$$Q_0 \quad \longrightarrow \quad Q_t = Q_0 \left(\frac{3K^2 - J(J+1)}{(J+1)(2J+3)} \right). \quad (5.10)$$

Geometrically, the quadrupole deformation parameter β is directly related to the intrinsic quadrupole moment Q_0 which is a constant within a rotational band [69]:

$$Q_0 = \frac{3}{\sqrt{5\pi}} Z R_0^2 \beta (1 + 0.16\beta) \quad (5.11)$$

with Z being the atomic number. For an evaluation of the intrinsic quadrupole moment, the $B(E2)$ values are determined from the measured lifetime τ as [75]

$$B(E2 : J + 2 \rightarrow J) = 8.161 \cdot 10^{-14} \frac{R_b}{1 + \alpha_c} \frac{E_\gamma^{-5}}{\tau} [(eb)^2] \quad (5.12)$$

with the γ -ray energy E_γ in units of MeV (hereby, the recoil of the nucleus after γ -ray emission is neglected) and τ in seconds. α_c is the conversion coefficient and R_b is the relative branching ratio of the considered transition. The unit ‘‘barn’’ corresponds to $b = 100 \text{ fm}^2$. It is also common to express the $B(E2)$ value in units of single-particle excitation, the Weisskopf unit W.u., using the relation $B(E2)_{\text{W.u.}} = 1.6834 \cdot 10^5 A^{-4/3} B(E2)_{(eb)^2}$ [75].

As the quadrupole moment of the rigid rotor is a constant within one band (intra-band transitions), it follows from Eq. (5.9):

$$B_{4/2} = \frac{B(E2 : 4_1^+ \rightarrow 2_1^+)}{B(E2 : 2_1^+ \rightarrow 0_1^+)} = \frac{10}{7} \iff \text{the rigid rotor model}, \quad (5.13)$$

which is known as one of the ‘‘Alaga rules’’ [76] and provides another strong signature for the rigid rotor model. Transitions between β and γ vibrational bands (inter-band transitions) are forbidden, as such transitions involve the simultaneous destruction of one vibration and creation of another one. Thus, the transition selection rule for the rigid rotor is $\Delta K = 0^1$.

Other collective excitations can be obtained using different potentials $V(\beta, \gamma)$ to solve the Bohr-Mottelson Hamiltonian. For example, a potential rigid in γ centered at $\beta = 0$ and $\gamma = 0^\circ$ gives the typical quadrupole phonon spectrum of a harmonic oscillator (the spherical vibrator) with equal energy spacing of $\hbar\omega$ (vibrational energy). Thus, the signature of a spherical vibrator is $R_{4/2} = 2$. For the axially asymmetric deformed rotor, the potential is centered at a finite β and is completely free in the γ degree of freedom. Such a γ -unstable rotor is described by the Willets-Jean model [74]. The signature for this case of γ instability is $R_{4/2} = 2.5$.

The algebraic Interacting Boson Approximation (IBA)

The IBA for even-even nuclei proposed by A. Arima and F. Iachello in 1974 [70] as an algebraic model is based on a group theoretical approach. The *sd*-IBA is founded on the assumption that the valence nucleons couple in pairs with angular momentum 0 or 2. These coupled nucleons are treated as bosons (*s* and *d* bosons). In its simplest form, the IBA-1, no distinction between protons and neutrons is made. Closed magic shells of protons and neutrons are assumed to be inert. Thus, only valence bosons and the interaction between them generate excitation spectra. The number of valence bosons is half the number of valence protons and valence neutrons. Both are always counted to the nearest proton

¹ γ -g (g: ground band) and β -g ($K=0$ -g) transitions are weakly allowed (hindered) by the Alaga rules and are also observed experimentally [74].

and neutron closed magic shell, whereby the equivalence of boson particles and boson holes are taken into account.

Since an s boson ($J = 0$) has only one magnetic sub-state and a d boson ($J = 2$) has five, the sd boson system spans a 6 dimensional space. Such a system can be described in terms of the algebraic unitary group structure $U(6)$. The IBA formalism is phrased in terms of creation and destruction operators for s and d bosons. The 36 elements of the unitary group $U(6)$ are the operators

$$\mathbf{s}^\dagger \mathbf{s}, \mathbf{s}^\dagger \tilde{\mathbf{d}}_\mu, \mathbf{d}_\mu^\dagger \mathbf{s} \text{ and } (\mathbf{d}_\mu^\dagger \tilde{\mathbf{d}}_\mu)^{(J)} \text{ with } J = 0, 1, 2, 3, 4 \text{ and } |\mu| \leq J. \quad (5.14)$$

This set of operators close on commutation, hence the commutator $[\mathbf{A}, \mathbf{B}] = \mathbf{AB} - \mathbf{BA}$ of any pair of the operators of $U(6)$ vanishes or is proportional to an operator of the group or a linear combination thereof. The operators of $U(6)$ also follow the Jacobi-identity $[[\mathbf{A}, \mathbf{B}]\mathbf{C}] + [[\mathbf{B}, \mathbf{C}]\mathbf{A}] + [[\mathbf{C}, \mathbf{A}]\mathbf{B}] = 0$. Therefore, the 36 operators are referred to as the generators of $U(6)$ and form a Lie algebra [74].

The Hamiltonian must conserve the total number of valence bosons N , hence

$$[\mathbf{H}, \mathbf{N}] = 0, \quad \mathbf{N} = \mathbf{n}_d + \mathbf{n}_s = \sum_{\mu} \mathbf{d}_\mu^\dagger \mathbf{d}_\mu + \mathbf{s}^\dagger \mathbf{s}, \quad N = n_d + n_s, \quad (5.15)$$

where \mathbf{N} is the total boson number operator with eigenvalue N . The total boson number operator commutes with all 36 generators of the group $U(6)$ and therefore, \mathbf{N} is the linear Casimir operator of $U(6)$, $\mathbf{N} = \mathbf{C}_1[U(6)]$. The set of basis states made of $(\mathbf{s}, \mathbf{d}_\mu)$ which conserves the quantum number N is called the irreducible representation of the group $U(6)$.

Suppose now that some smaller set of operators also close among themselves on commutation. This set forms the generators of a smaller subgroup of $U(6)$. This subgroup has one or more irreducible representations, thus quantum numbers that label the states. Per definition, the Casimir operator of a group that commutes with all generators of this group must be diagonal and therefore must conserve all quantum numbers including those of the subgroups. The most general Hamiltonian with one- and two-body interactions is written as a linear combination of first and second order (quadratic) Casimir operators of subgroups of $U(6)$ [74]:

$$\mathbf{H} = \epsilon \mathbf{C}_1[U(5)] + \alpha \mathbf{C}_2[U(5)] + \beta \mathbf{C}_2[O(5)] + \gamma \mathbf{C}_2[O(3)] + \delta \mathbf{C}_2[SU(3)] + \eta \mathbf{C}_2[O(6)]. \quad (5.16)$$

As the Hamiltonian must be invariant under rotation, provided by the rotation group $O(3)$, there are exactly 3 subgroups of $U(6)$ which include the group $O(3)$. The group structure of these three subgroups are referred to as dynamical symmetries of $U(6)$ with geometrical analogues in the case of infinite boson number. The group chains of those limits of the IBA-1 can be written along with their relevant quantum numbers as:

$$\begin{aligned}
\text{U(5) limit (spherical vibrator)} &\iff \text{U(6)} \supset \text{U(5)} \supset \text{O(5)} \supset \text{O(3)} \\
&\qquad\qquad\qquad N \qquad\qquad n_d \qquad\qquad (\nu) \qquad\qquad \Delta n_{ph}, J \\
\text{SU(3) limit (prolate rigid rotor)} &\iff \text{U(6)} \supset \text{SU(3)} \supset \text{O(3)} \\
&\qquad\qquad\qquad N \qquad\qquad (\lambda, \mu) \qquad\qquad \Delta K, J \\
\text{O(6) limit (\gamma-unstable rotor)} &\iff \text{U(6)} \supset \text{O(6)} \supset \text{O(5)} \supset \text{O(3)} \\
&\qquad\qquad\qquad N \qquad\qquad \sigma \qquad\qquad \tau \qquad\qquad \Delta\tau, J
\end{aligned}$$

Since the quantum numbers characterizing a subgroup are conserved, all the states of that representation are degenerated. The degeneracy is broken only by the next step in the group chain, which sub-classifies the levels according to other quantum numbers of the subsequent subgroup. Each Casimir operator has eigenvalues that are functions only of the conserved quantum numbers of the particular subgroup. Thus, a transition operator consisting of generators of a given group or subgroup cannot connect different irreducible representations, which leads to many essential selection rules. The $B(E2)$ values and selection rules for $E2$ transitions in the limits of the IBA are given by [74]:

$$B(E2 : J + 2 \rightarrow J)_{\text{U(5)}} = e_B^2 \frac{1}{4} (J + 2)(2N - 1), \quad \Delta n_{ph} = \pm 1, \quad (5.17)$$

$$B(E2 : J + 2 \rightarrow J)_{\text{SO(3)}} = e_B^2 \frac{3}{4} \left[\frac{(J + 2)(J + 1)}{(2J + 3)(2J + 5)} \right] (2N - J)(2N + J + 3), \quad \Delta K = 0, \quad (5.18)$$

$$B(E2 : J + 2 \rightarrow J)_{\text{O(6)}} = e_B^2 \frac{1}{8} \frac{J + 2}{J + 5} (2N - J)(2N + J + 8), \quad \Delta\sigma = 0 \text{ and } \Delta\tau = \pm 1. \quad (5.19)$$

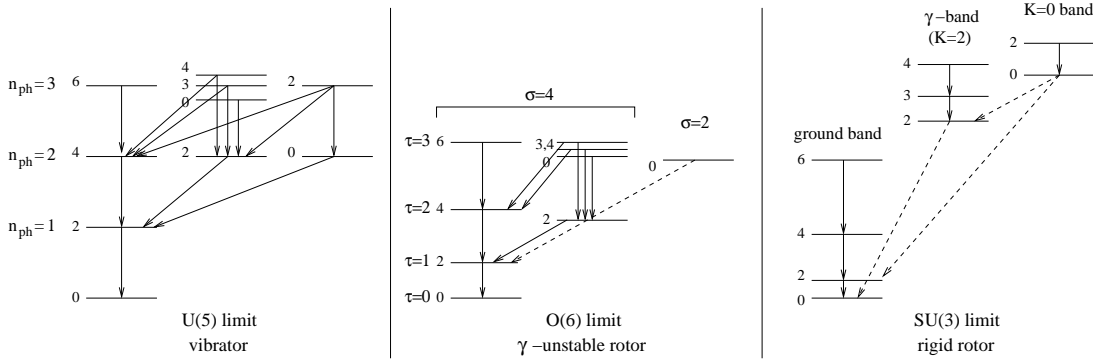


Figure 5.1: Energy spectra of the three IBA limits sub-titled by the geometric analogues. Transitions indicated with dashed arrows are forbidden (hindered).

For nuclear structure studies of transitional nuclei, the consistent Q formalism (CQF) of the IBA formulated by D. D. Warner and R. F. Casten in 1982 [77] is widely used. The CQF reduces the number of free fit parameters from six in Eq. (5.16) to only two plus one scaling factor which makes it easier to establish a relationship between the IBA and corresponding geometrical analogues. The CQF Hamiltonian is given by [77]

$$\mathbf{H} = c \left((1 - \zeta) \mathbf{n}_d - \frac{\zeta}{4N} \mathbf{Q} \cdot \mathbf{Q} \right), \quad (5.20)$$

with c treated as a scaling factor and the quadrupole operator

$$\mathbf{Q} = (\mathbf{s}^\dagger \tilde{\mathbf{d}} + \mathbf{d}^\dagger \mathbf{s})^{(2)} + \chi (\mathbf{d}^\dagger \tilde{\mathbf{d}})^{(2)}, \quad \chi \in \left[-\frac{\sqrt{7}}{2}, 0\right]. \quad (5.21)$$

Using this Hamiltonian, the dynamical symmetries are related to

$$\begin{aligned} \text{U(5) limit:} & \quad \zeta = 0 \quad \text{and} \quad \chi \in \left[-\frac{\sqrt{7}}{2}, 0\right] \\ \text{SU(3) limit:} & \quad \zeta = 1 \quad \text{and} \quad \chi = -\frac{\sqrt{7}}{2} \\ \text{O(6) limit:} & \quad \zeta = 1 \quad \text{and} \quad \chi = 0. \end{aligned}$$

The transitional region between the dynamical symmetries is then described by only two parameters which are defined as

$$\zeta \in [0, 1] \quad \text{and} \quad \chi \in \left[-\frac{\sqrt{7}}{2}, 0\right]. \quad (5.22)$$

These two parameters are commonly used to map the symmetry structure of the IBA in a two dimensional plot, as presented in Fig. 5.2. The three dynamical symmetries are located at the vertices of the symmetry triangle (also known as the ‘‘Casten triangle’’). The transitional nuclei are located inside the Casten triangle and the position is given by the parameterization [78]:

$$\rho = \frac{\sqrt{3}\zeta}{\sqrt{3}\cos\theta_\chi - \sin\theta_\chi}, \quad \theta = \frac{\pi}{3} + \theta_\chi \quad \text{with} \quad \theta_\chi = \frac{2\pi}{3\sqrt{7}}\chi, \quad \theta_\chi \in \left[-\frac{\pi}{3}, 0\right]. \quad (5.23)$$

Shape phase transitions

In analogy to many physical systems, nuclei might undergo a phase transition between two nuclear shapes. Two so-called ‘‘critical symmetries’’, namely the X(5) and the E(5) critical symmetries, were found analytically [79, 80, 81] in the geometrical collective model (GCM [73]). The X(5) critical symmetry is found in the spherical-deformed shape phase transitional region and is classified as phase transition of first order, in accordance with the classification of Ehrenfest [82, 83]. The E(5) critical symmetry is a second order phase transition and lies on the U(5)-O(6) leg of the IBA symmetry triangle, hence $\chi = 0$ [83, 84]. No phase transitions occurs between axially deformed and γ -unstable shapes. In the case of infinite boson number, the U(5)-SU(3) shape phase coexistence in the IBA is related to $\zeta_c = 0.5$ [85], as illustrated by the solid line in Casten triangle shown in Fig. 5.2. Clearly, the critical symmetries are not exactly realized in the IBA due to finite boson number.

As critical point symmetries, the geometrical X(5) and E(5) models each provide universal energy spectra and $E2$ transition strengths $B(E2)$ which only need to be normalized to experimental data. These values can be found in Refs. [81, 84] including detailed descriptions of the analytic calculations and algebraic approaches. The experimental signatures of the critical symmetries are:

$$\text{X(5) model: } R_{4/2} = 2.9, \quad (5.24)$$

$$\text{E(5) model: } R_{4/2} = 2.2. \quad (5.25)$$

It was found experimentally that ^{150}Nd [86] and ^{154}Gd [87] show many X(5) features. Recently, ^{176}Os and ^{178}Os have been measured to be “X(5)-like” [88, 89], the first eligible X(5) candidates in the $A=170-180$ region. An E(5) candidate was found empirically in the ^{134}Ba isotope [83, 90].

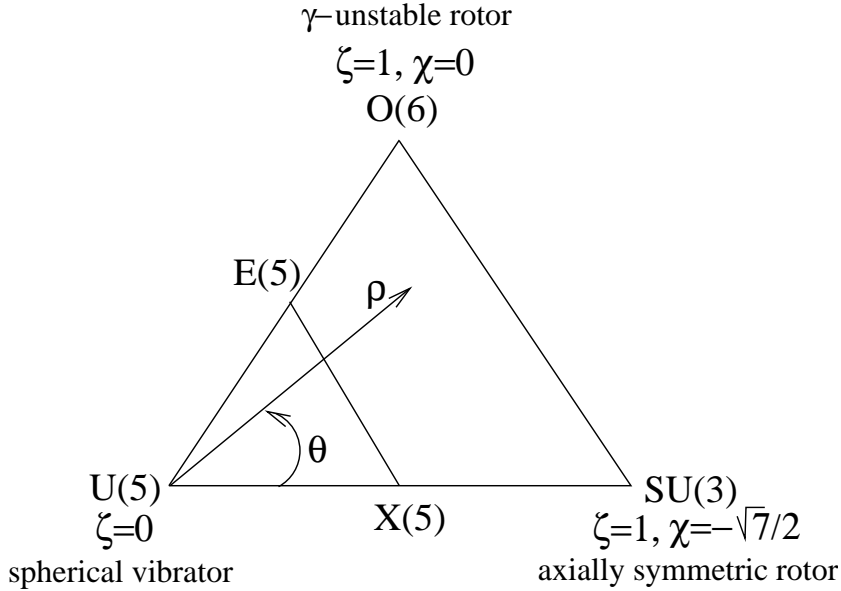


Figure 5.2: The symmetry triangle of the IBA, also called the Casten triangle. The straight line within the Casten triangle corresponds to $\zeta_c = 0.5$ and represents the X(5) shape phase coexistence between spherical and deformed nuclei for the case of infinite boson number.

5.2 γ - γ fast timing on ^{176}W using the MSCD method

The lifetimes of the excited states forming the ground-state yrast band in the even-even ^{176}W isotope (see Fig. 5.4) are unknown. These lifetimes would provide important information for nuclear structure studies on the ^{176}W isotope itself but also for investigation on the nuclear shape phase transition with respect to the isotopic chain of tungsten. ^{176}W is just 2 neutrons away from mid-shell and the ratio of the level energies of the 4_1^+ and 2_1^+ states is $R_{4/2} = 3.21$, which is quite close to $R_{4/2} = 3.33$ of the rigid rotor model. The energy level spacing of a rigid rotor is proportional to $J(J+1)$, which is also almost the case for ^{176}W . Subject of this Section is a nuclear structure analysis on the ^{176}W isotope.

5.2.1 Experimental setup and results

The main goal of this in-beam experiment was to reduce the low-energy background obtained in γ -ray spectroscopy. As illustrated in Chapter 4.2, this low-energy background is probably mainly due to cross-talk events or due to scattered γ -rays from the experimental surrounding. These background events are largely delayed compared with the prompt response of same energy and thus undesirable for timing purposes. In principle, this kind of background can be suppressed using massive BGO scintillators for an active stray γ -ray shielding. In addition, escaped Compton scattered γ -rays which come from the detecting crystal and encounter the BGO shield of this detector can be used as a veto condition to reduce the Compton background. The IKP HORUS cube spectrometer is ideally suited for γ - γ coincidence experiments. This spectrometer was originally designed for high-resolution high-efficiency γ - γ angular correlation measurements and possesses of 6 large anti Compton BGO shields in a well defined geometry.

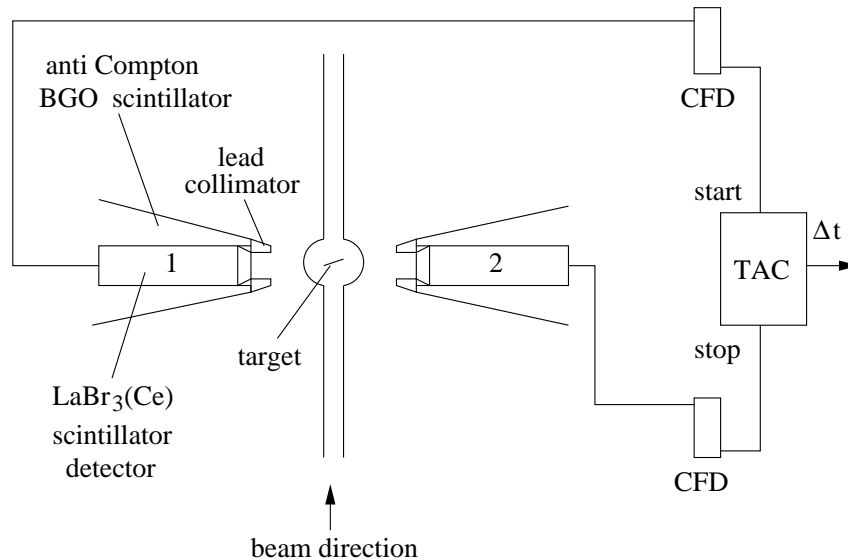


Figure 5.3: Schematic drawing of the experimental setup used for γ - γ timing at the IKP Cologne HORUS γ -ray cube spectrometer. Events detected in the BGO scintillator are used for veto condition.

The excited states in ^{176}W were produced using the fusion evaporation reaction $^{169}\text{Tm}(^{11}\text{B},4\text{n})^{176}\text{W}$. The 56 MeV ^{11}B ions provided a large reaction cross section of ≈ 900 mbarn. Therefore, only two $\text{LaBr}_3(\text{Ce})$ detectors were installed for fast timing experiments. As illustrated in Fig. 5.3, the two IKP $\text{LaBr}_3(\text{Ce})$ detectors (with XP20D0 PMTs) were placed inside two massive BGO shields in a face to face configuration. To avoid direct γ -ray irradiation of the BGO from the target, a 3 cm thick lead collimator with circular opening diameter of 3 cm was mounted on the front end of the BGO scintillator. The whole $\text{LaBr}_3(\text{Ce})$ detector plus BGO shield assemblies were placed close to the spherically shaped target chamber which has a diameter of only 6 cm. Thus, the detector-target distance was about 10 cm. As illustrated in Fig. 5.5a, an effective background suppression for $E_\gamma < 450$ keV was achieved. The spectrum labeled “unshielded”

was obtained in a previous γ - γ timing experiment [91], where the unshielded LaBr₃(Ce) detectors were placed in closed geometry to the target at angles of 45° and 135° to the beam direction. A progressive increase of the background reduction with decreasing γ -ray energy is observed for $E_\gamma < 450$ keV; similarly with the observed increase of the time response of the background relative to prompt events with decreasing energies for $E_\gamma < 450$ keV, as discussed in Chapter 4.2 (see also Fig. 4.12). These results strongly indicate that the “low-energy background” is mainly due to scattered γ -rays coming from the experimental surrounding including the other detectors (i.e. the cross-talk events). At higher energies, the Compton suppression improves the peak-to-background ratio by factor of 1.2 to 1.5.

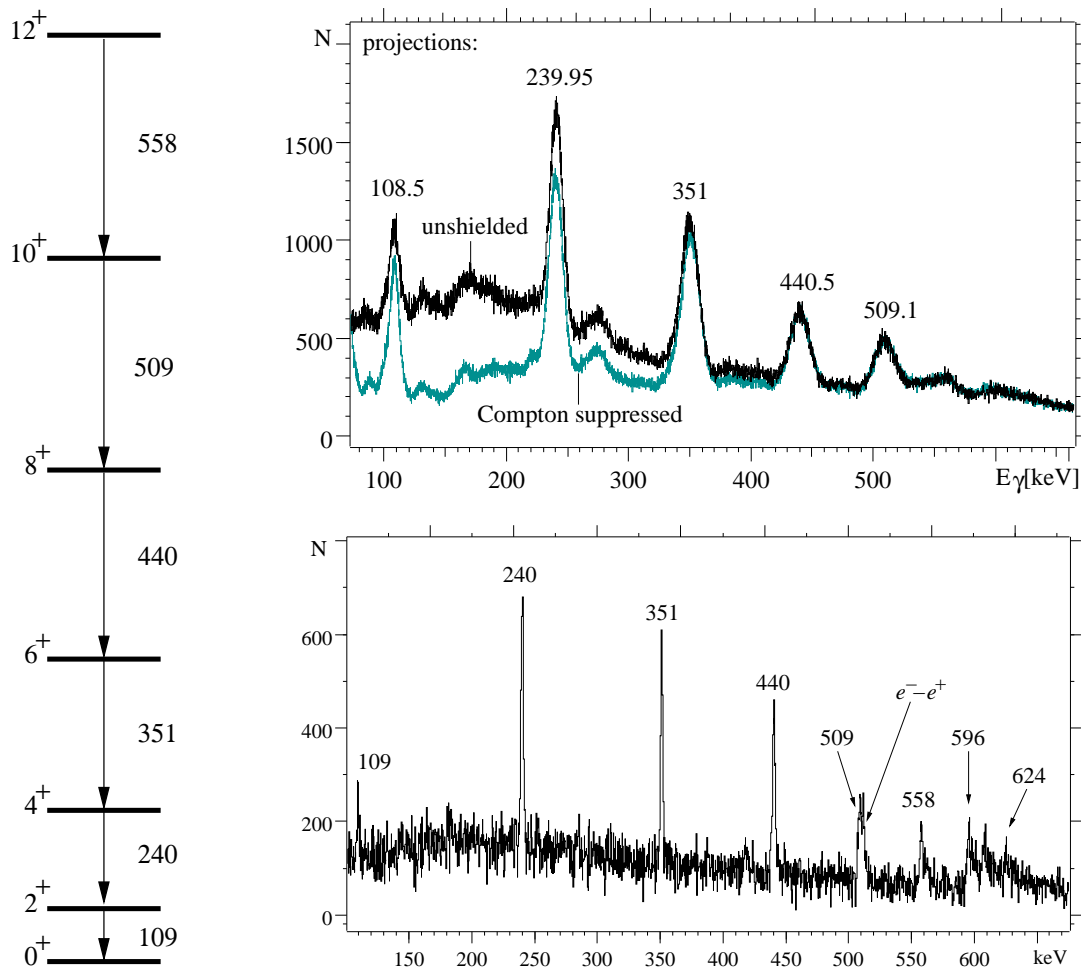


Figure 5.4: Ground-state yrast band in ^{176}W .

Figure 5.5: a: In-beam (singles gated) γ -ray spectra of ^{176}W obtained using the unshielded LaBr₃(Ce) detector [91] and by using active BGO shielding, respectively. Note the effective background reduction at low energies. b: Summed high resolution HPGe coincidence γ -ray spectrum obtained by gating the LaBr₃(Ce) detectors on the 240 keV, 351 keV and 440 keV transitions.

An additional high purity germanium (HPGe) detector was installed in order to investigate for possible unresolved contaminants in the $\text{LaBr}_3(\text{Ce})$ γ -ray spectrum and the result is shown in Fig. 5.5b. Except the annihilation γ -rays of 511 keV which contaminate the 509 keV γ -rays of the ($10_1^+ \rightarrow 8_1^+$) transition in ^{176}W , the spectrum of the ^{176}W isotope is very clean.

For fast timing measurements, the standard anode timing circuitry using two CFDs and one TAC was installed. To provide good time resolution especially for the 108 keV ($2_1^+ \rightarrow 0_1^+$) γ -ray transition of the ^{176}W isotope, the PMT voltages were set to about -1200 V. A shaping delay time of 8 ns was used for both CFDs of the fast timing setup.

For picosecond lifetime measurements, the PRD curve of the setup was measured using the ^{152}Eu γ -ray source. The source was placed precisely at the position of the target's beam spot. The result of the 36 hour PRD calibration measurement is presented in Fig. 5.6. The derived PRDs were fitted using Eq. (4.13) with resulting total uncertainty of only 7 ps (3σ deviation). The fit parameters obtained are:

$$\begin{aligned}
 a &= (-12690.1 \pm 630.9) && \text{ps}\sqrt{\text{keV}} && (5.0\%) \\
 b &= (-100.145 \pm 5.652) && \text{keV} && (5.7\%) \\
 c &= (0.496442 \pm 0.019702) && \text{ps/keV} && (4.0\%) \\
 d &= (734.4 \pm 39.0) && \text{ps} && (5.3\%).
 \end{aligned}$$

For three γ -ray transitions (reference energies) depopulating the 4_1^+ , 6_1^+ and 8_1^+ states in ^{176}W , the centroid differences for different energy combinations were measured. As shown in Fig. 5.8, also γ -rays feeding states above the level of the interest were used for the MSCD analysis. For the 8_1^+ state ($E_{\text{ref.}} = 440$ keV), no significant shift of the data points is observed. The data point at 558 keV also indicates the lifetime of the 10_1^+ state to be prompt (not measurable lifetime). Taking uncertainties into account, an upper limit of $\tau(8_1^+) < 4$ ps is assigned by this measurement. Significant shifts are obtained for the 4_1^+ and the 6_1^+ states. Fig. 5.9 shows the PRD corrected data of the MSCD analysis. The value of the corrected data then corresponds to twice the lifetime of the considered excited state. The results for the 6_1^+ state derived from the 351 keV gated centroid differences are all consistent (Fig. 5.9b). This confirms the previously obtained results for the 8_1^+ and 10_1^+ states. For evaluation of the lifetime $\tau(6_1^+) = 12(4)$ ps, only the result due to the directly feeding transition at 440 keV was taken into account, as derived from Fig. 5.7b. The same procedure was applied to the 4_1^+ state (Fig. 5.9a). The data points belonging to transitions above the 6_1^+ state are shifted compared with the directly feeding transition at 351 keV (derived from Fig. 5.7a). This shift is due to the lifetime of the intermediate 6_1^+ state. The mean shift from the assigned value of $2\tau(4_1^+) = 134(8)$ ps indicated by the solid line is $2\tau(6_1^+) = 21(8)$ ps, which is in very good agreement with the directly measured lifetime of the 6_1^+ state.

Such MSCD analysis of subsequent transitions (series of transitions) is anal-

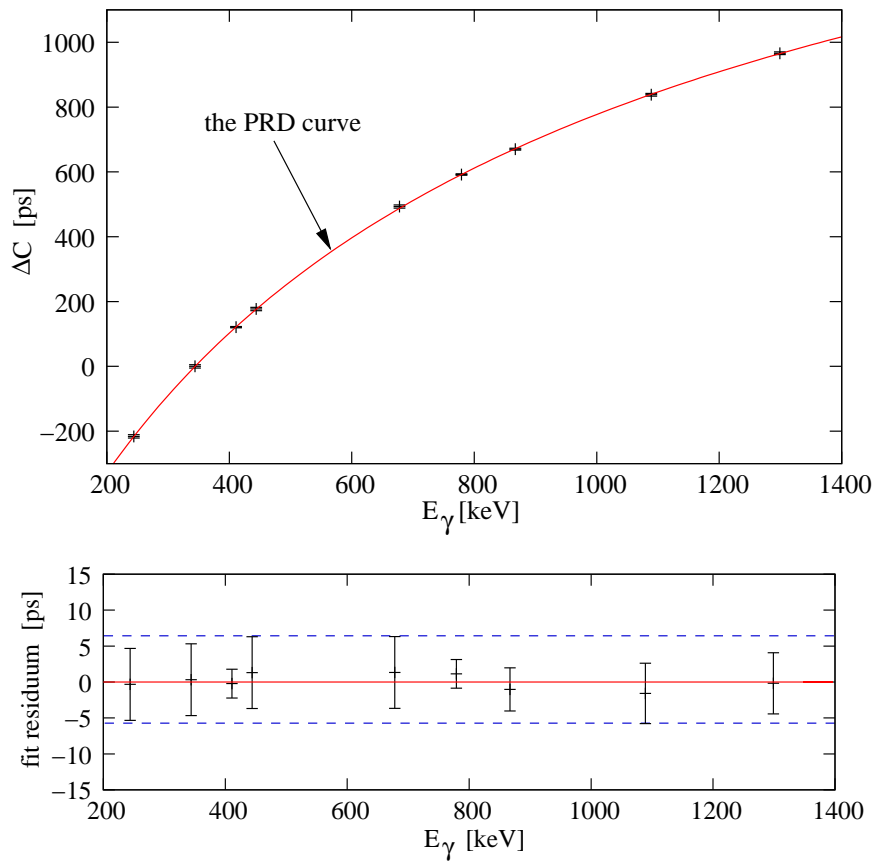


Figure 5.6: Above: The PRD curve of the experimental setup obtained using the ^{152}Eu γ -ray source and the PRD calibration procedure described in Section 4.2.1. Below: The overall accuracy (3σ deviation) of the PRD calibration is 7 ps.

ogous to the relative comparison method [14] for the standard centroid shift method. The results of this MSCD analysis are consistent and show the high sensitivity of the MSCD method. Further MSCD analyzes were performed in order to investigate the possible contribution of the background. The result of the analysis on the 240 keV transition is presented in Fig. 5.10. No significant difference between the response of the background and that of the full energy peaks can be observed, thus no correction for background contribution is needed. Similar results were obtained for the other two γ -rays (reference energies).

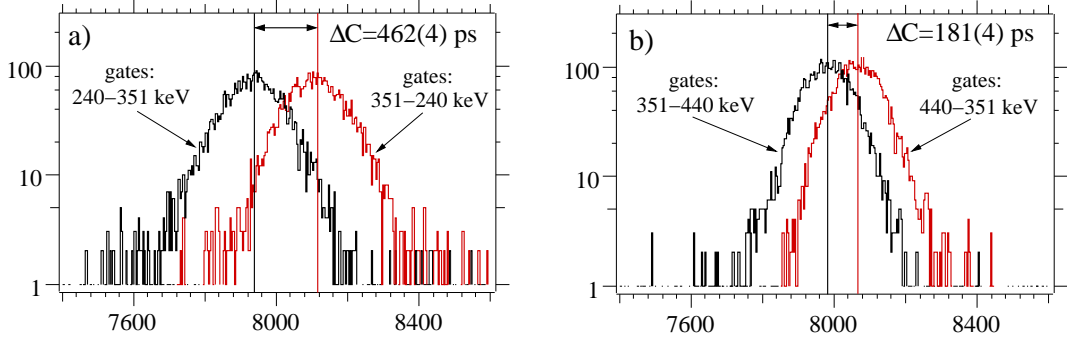


Figure 5.7: a: The centroid difference of the two γ - γ time spectra for the 351 keV \rightarrow 240 keV cascade connecting the 4_1^+ state in ^{176}W . For this energy combination, the FWHM \approx 410 ps corresponds to a time resolution of $\delta t \approx$ 300 ps. The time spectrum calibration is 2.2 ps/chn. b: MSCD analysis of the 6_1^+ state using the 440 keV \rightarrow 351 keV cascade (FWHM \approx 330 ps; $\delta t \approx$ 235 ps).

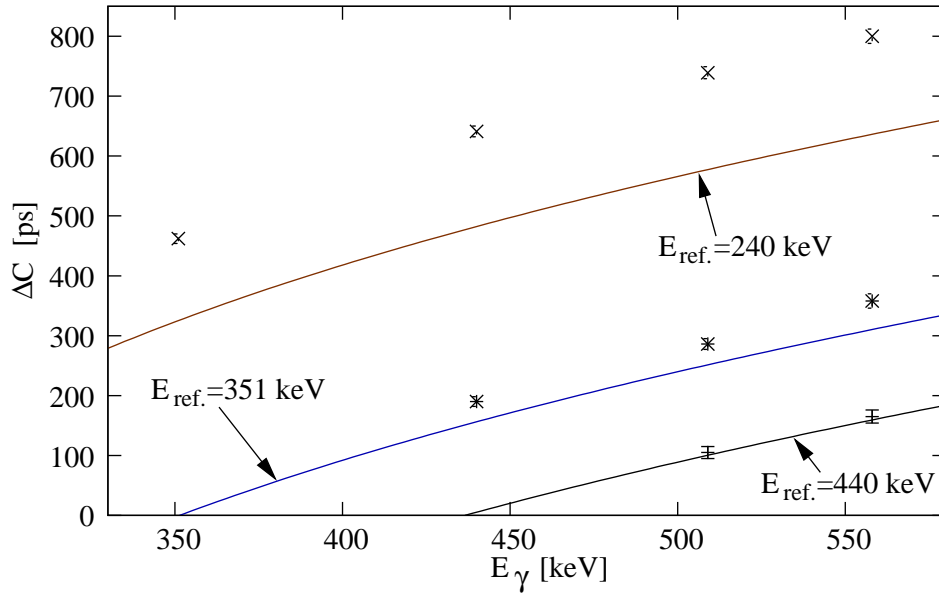


Figure 5.8: Experimental centroid differences of all possible energy combinations in ^{176}W corresponding to combinations of transitions within the yrast band shown in Fig. 5.4. For comparison, the PRD curve is adjusted for the reference energy of the common data points. The significant upward shift of the data points indicate measurable picosecond lifetimes.

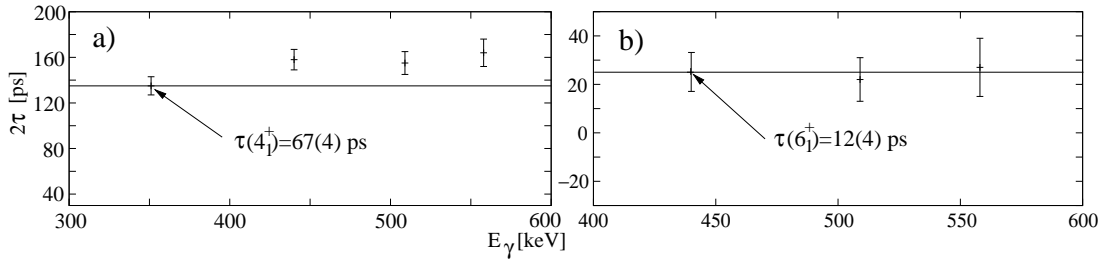


Figure 5.9: a: Centroid differences of the 240 keV transition depopulating the 4_1^+ state in ^{176}W corrected for the corresponding PRDs. b: The same analysis for the 351 keV transition depopulating the 6_1^+ state. The results are discussed in the text.

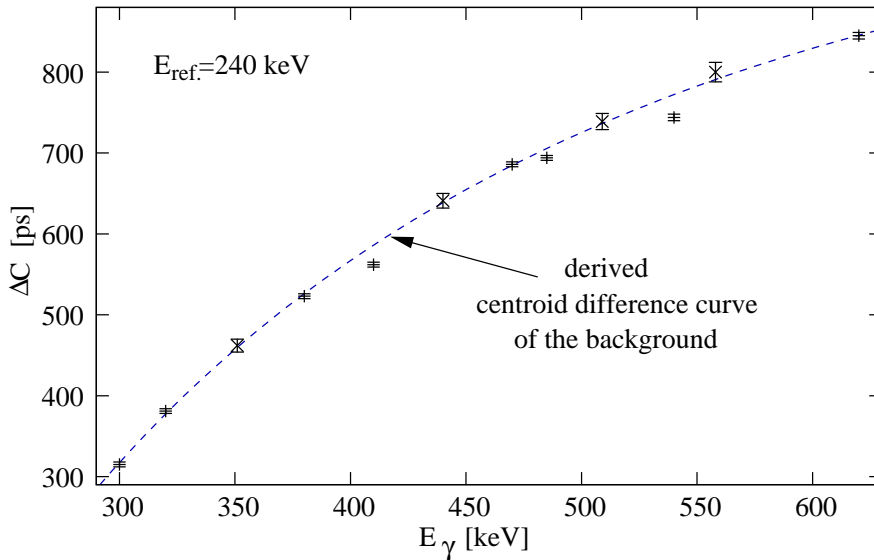


Figure 5.10: Centroid differences of the 240 keV transition in combination with background gates compared with the full energy centroid differences of cascades in ^{176}W marked as crosses.

The lifetime of the 2_1^+ was already measured in a previous experiment [91], where two unshielded $\text{LaBr}_3(\text{Ce})$ detectors were installed to perform γ - γ coincidences. This first time in-beam γ - γ timing experiment with $\text{LaBr}_3(\text{Ce})$ detectors at the IKP was performed in order to test the capability of lifetime measurements in the low-energy region. Fig. 5.11 shows the coincidence γ -ray spectrum obtained by gating on the directly feeding 240 keV transition compared with that obtained from the experiment presented in this work using active BGO shielding. The results of the lifetime measurements of the first 2^+ state in ^{176}W derived from the two different γ - γ experiments are presented in Figs. 5.12 and 5.13. As already observed, the low-energy background is largely delayed, as can be seen in Fig. 5.12b. Due to a poor peak-to-background ratio of about 1 for the unshielded case, a two component time distribution has been obtained. In this case (Fig. 5.12a),

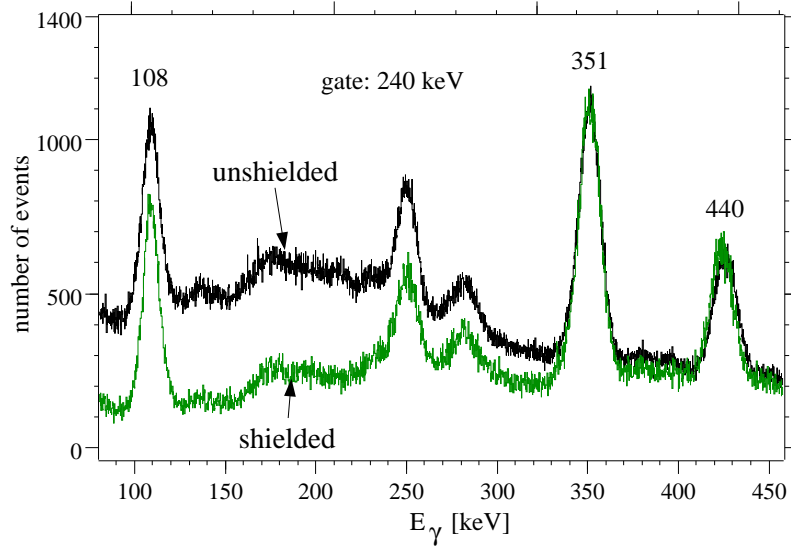


Figure 5.11: Coincidence γ -ray spectra of ^{176}W obtained by gating on the 240 keV transition. Using active shielding, the peak-to-background ratio of the 108 keV ground-state transition is drastically improved by factor of ≈ 3 .

only few data points with low statistics can be used for lifetime determination using the slope method. This can easily lead to systematically overestimate the measured lifetime. No accurate procedure to subtract the background contribution could be developed. The main problem is that the delay of the background time spectra is energy dependent and cannot be accurately interpolated from the data.

The advantage of using active background suppression is depicted in Fig. 5.13. The largely reduced background contribution is more prompt like, thus almost the complete delayed background is suppressed. This results in a more accurate lifetime determination, as much more data points with good statistics can be used compared with the unshielded case. For the evaluation of the lifetime of the 2_1^+ state, the weighted average of the two results obtained from the two shielded detectors yields $\tau(2_1^+) = 1.44(4)$ ns. No further errors have to be taken into account, as by combining the two results, the electronic drift is canceled. Also, by choosing data points well outside the region outspreaded by the background time spectrum where only random coincidences are contributing to the time spectrum, only the statistics contributes to the error.

In a later high precision e^- - γ fast timing experiment [19], the lifetime of the first 2^+ state in ^{176}W was re-measured to be $\tau = 1.43(2)$ ns which is in excellent agreement with the result presented in this work. The lifetime was measured using the IKP Orange spectrometer with energy resolution of 1% in combination with the IKP $\text{LaBr}_3(\text{Ce})$ detector. This was the first lifetime measurement of this kind reported in literature. Furthermore, an e^- - e^- lifetime measurement of the same state has delivered the result of $\tau = 1.43(2)$ ns [92].

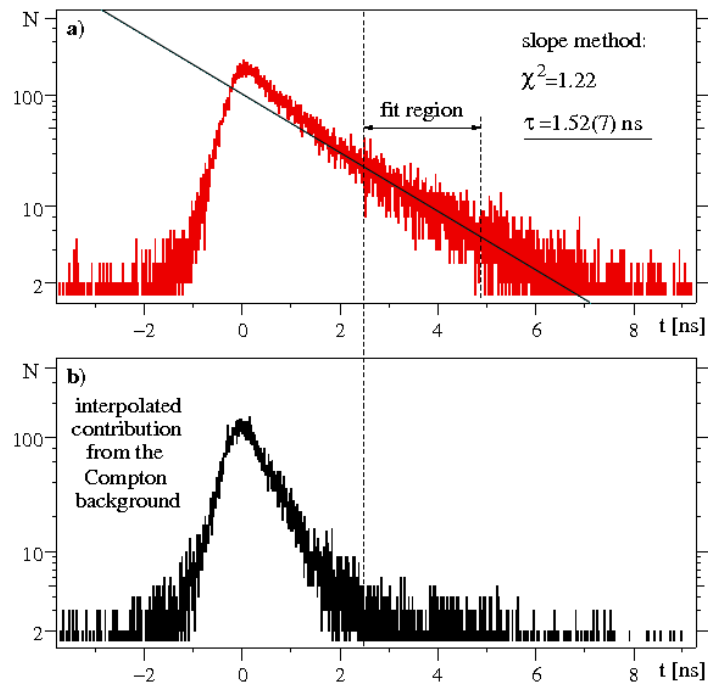


Figure 5.12: a: Time distribution of the 240 keV \rightarrow 108 keV cascade connecting the first 2^+ state in ^{176}W . The spectrum was measured in a previous experiment without the use of background suppression [91]. b: The largely delayed background time spectrum was obtained by gating the detectors on the 240 keV transition and on the background at 140 keV.

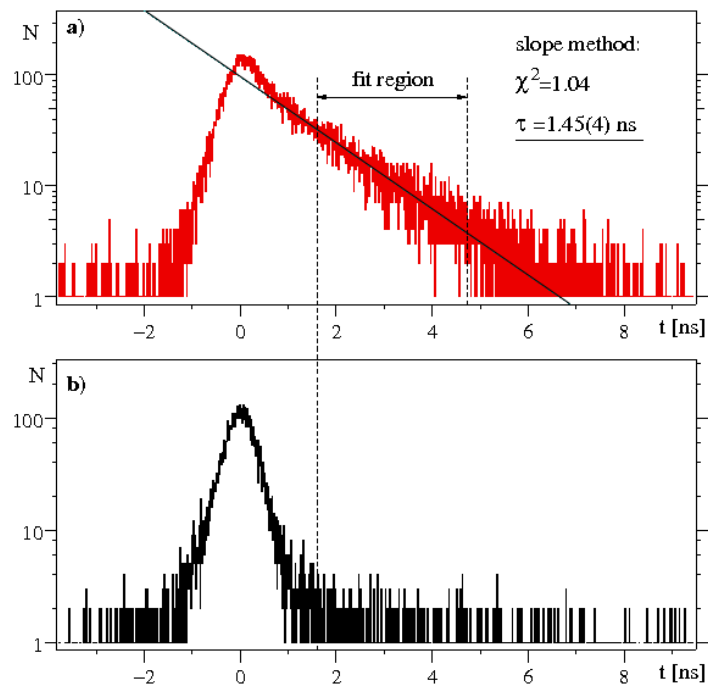


Figure 5.13: a: Time distribution of the 240 keV \rightarrow 108 keV cascade in ^{176}W obtained using active background suppression. b: The background at 140 keV is more prompt in contrast to the unshielded case shown in Fig. 5.12b.

The results presented in this Section show the high reliability and accuracy of the lifetime determination using the high resolution ultra fast $\text{LaBr}_3(\text{Ce})$ detectors for γ -ray spectroscopy. A summary of the lifetime results measured is given in the following Section. The results also demonstrate the necessity of using active background suppression when performing lifetime measurements in the γ -ray energy region lower than about 300 keV. The use of high resolution γ -ray monitoring in coincidence mode is also highly recommended in order to ensure the absence of possible contaminants.

5.2.2 The lifetimes of the yrast-states in ^{176}W

For a nuclear structure analysis of the ^{176}W isotope, calculations were performed using the rigid rotor model, the IBA-1 and the dynamical symmetries of the IBA-1 corresponding to the geometric analogues of axially symmetric deformed and γ -unstable rotors. The U(5) limit is excluded, as $R_{4/2}(^{176}\text{W}) = 3.21$. However, as this value is not far from the value of 2.9 for the critical symmetry X(5), which describes the shape phase transition between the limits U(5)-SU(3), also the X(5) model was used for analysis.

An IBA fit has been performed using the CQF Hamiltonian of Eq. (5.21). For the fit, the energies of the ground band up to spin 12^+ , the γ band and the $K = 0$ band, as far as they are known were used. No transition strengths were taken into account for the fit. The resulting fit parameters are:

$$c = 1.478 \text{ MeV}, \quad \zeta = 0.599, \quad \chi = -0.946. \quad (5.26)$$

Fig. 5.14 shows the IBA generated spectrum of ^{176}W compared with the experimental data. For the ground band and the γ band, the IBA agrees well with the empirical data. Only the energy spacing between the states of the first $K = 0$ band are not well reproduced, which is a well-known structural issue of the IBA [74].

Also shown is the spectrum of the ground band assuming the rigid rotor model. In this case the energy of the first excited state of the ground yrast band was used to determine the moment of inertia, according to Eq. (5.7). Obviously, the energy spacing between the states of the ground yrast band in ^{176}W is not rigid in the moment of inertia, i.e. in the deformation parameter β . This can be explained by a spin dependent ‘‘centrifugal stretching’’ of the deformation parameter [93]. A more accurate approach was found in the effective Variable Moment of Inertia (VMI) model [94].

$B(E2)$ values of the ground band yrast states of ^{176}W up to spin 8_1^+ were determined using Eq. (5.12) and the measured lifetimes, as listed in Tab. 5.1. According to Eqs. (5.9-5.10) with $K = 0$, the quadrupole moments $Q(J_i)$ were derived from the spectrometric ones. Those are compared with the values obtained as a result of the IBA fit using the $E2$ transition operator $\mathbf{T}(E2) = e_B \mathbf{Q}$ with \mathbf{Q} of Eq. (5.22), χ as given in Eq. (5.27) and $e_B = 0.139 \text{ eb}$ as obtained by normalization on the experimental $B(E2 : 2_1^+ \rightarrow 0_1^+)$ value. The quadrupole moments

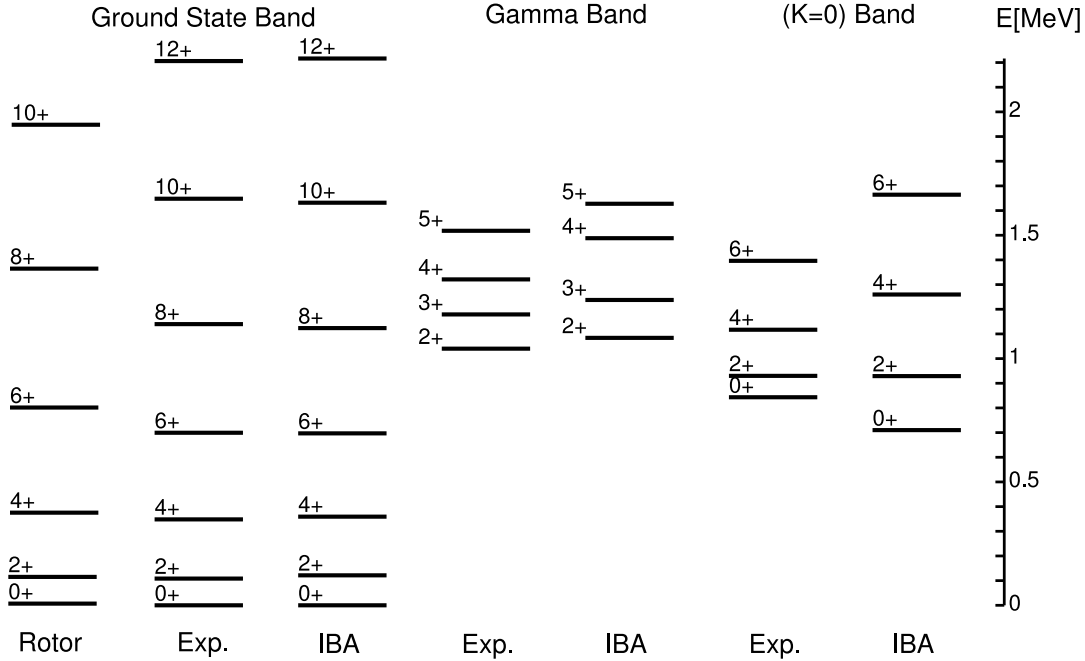


Figure 5.14: IBA spectrum of ^{176}W obtained by a fit of the energy eigenvalues of the CQF Hamiltonian to the experimental data shown for comparison. The typical $J(J+1)$ spacing of the rigid rotor model is also presented for the ground band.

within the limits of the IBA were calculated using Eqs. (5.19) and (5.20) again normalized on the experimental $B(E2 : 2_1^+ \rightarrow 0_1^+)$ value with resulting effective boson charge of 0.1064 eb for SU(3) and 0.14 eb for O(6). The quadrupole moments for the X(5) critical symmetry were deduced from the $B(E2)$ values given in Fig. 2 of Ref. [81]. The results listed in Tab. 5.1 are presented graphically in Fig. 5.15.

There is an evidence for the deformed shape of the ^{176}W isotope. The X(5) model for the U(5)-SU(3) shape phase coexistence does not agree with the experiment and can be excluded. Tentatively, a location of the ^{176}W isotope in the O(6)-SU(3) region can be interpreted from the results with a trend towards the SU(3) limit of the IBA (see also Fig. 5.4 in Section 5.4). This conclusion would also be drawn geometrically when considering the ratio of transition strengths $B_{4/2}(^{176}\text{W}) = B(E2 : 4_1^+ \rightarrow 2_1^+)/B(E2 : 2_1^+ \rightarrow 0_1^+) = 1.33$ which is close to the Alaga value of $10/7 = 1.43$ for the rigid rotor model [Eq. (5.13)].

Table 5.1: The quadrupole moments $Q(J_i)$ of the yrast states in ^{176}W obtained from the measured lifetimes $\tau(J_i)$ and deduced transitions strengths $B(E2)$ compared with the calculated model dependent ones.

$J_i \rightarrow J_f$	$\tau(J_i)$ [ps]	$B(E2)$ [W.u.]	$B(E2)$ [(eb) 2]	$Q(J_i)$ [eb]	Q_{IBA} [eb]	$Q_{\text{SU}(3)}$ [eb]	$Q_{\text{X}(5)}$ [eb]	$Q_{\text{O}(6)}$ [eb]
$2 \rightarrow 0$	1430(20)	168	0.983(21)	7.03(8)	7.03	7.03	7.03	7.03
$4 \rightarrow 2$	67(4)	224	1.312(79)	6.84(20)	7.23	7.04	7.44	6.98
$6 \rightarrow 4$	12(4)	208	1.216(406)	6.23(115)	7.30	6.91	7.88	7.07
$8 \rightarrow 6$	≤ 4	≥ 206	≥ 1.207	≥ 6.07	7.35	6.81	8.25	7.10

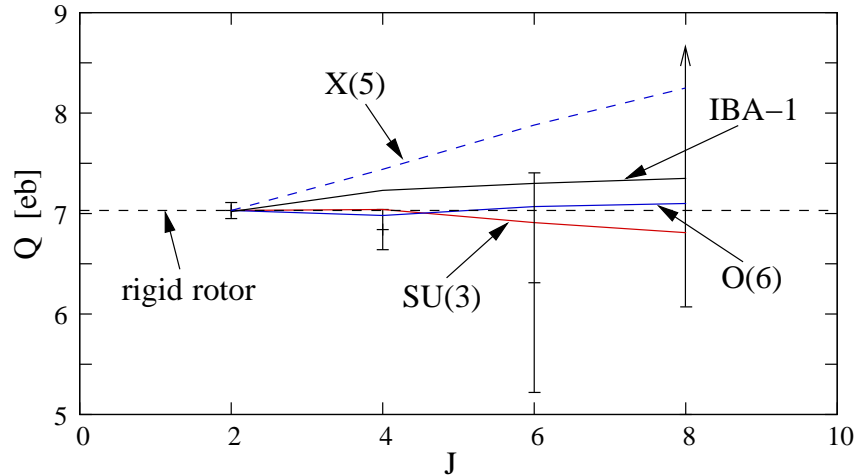


Figure 5.15: Graphical presentation of the experimental ground band quadrupole moments in ^{176}W (data points with error bar) in comparison to theoretical predictions using collective models. The lines are connecting the values of corresponding models, this is just to guide the eye. The results are interpreted in the text.

5.3 The lifetime of the 2_1^+ state in ^{172}Hf

The here presented experiment was part of a conversion electron e^-e^- fast timing campaign performed in February 2009 using the IKP Double Orange Spectrometer. During two weeks of beam time, the important lifetime of the first 2^+ state in four even-even rare earth isotopes have been measured or re-measured, respectively [19, 67]. The literature value for the lifetime of the 2_1^+ state in ^{172}Hf , $\tau(2_1^+) = 2.24(15)$ ns, dates back to 1967 and relies on γ - γ coincidences using

plastic scintillators [95] with extremely bad energy resolution of about 20%. The resulting $B(E2)$ strength has the largest error compared with neighboring even-even Hf isotopes. Also, the $B(E2)$ strength seems not to follow the smooth trend of the data from neighboring Hf isotopes.

To provide accurate lifetime of the 2_1^+ state in ^{172}Hf for nuclear structure analysis, this lifetime was re-measured using the high precision Double Orange Spectrometer. The e^-e^- timing technique is analogous to the $\gamma\text{-}\gamma$ timing technique while measuring the time difference of two coincident conversion electrons, corresponding to nuclear transitions populating and depopulating the state of the interest. The working principle and characteristics of the toroidal orange type magnetic electron spectrometer are described in details in Refs. [19, 21]. Therefore, only the results of the e^-e^- fast timing experiment on ^{172}Hf is reported here, which has not been published yet. The experimental Double Orange Spectrometer fast timing setup as described in Ref. [19] was shown to deliver highly reliable nanosecond lifetimes with absolute accuracy of only 20 ps. This setup was also used to measure the lifetime of the 2_1^+ state in ^{172}Hf . The nuclear excited states were produced by the $^{169}\text{Tm}(^6\text{Li},3\text{n})^{172}\text{Hf}$ fusion evaporation reaction at a beam energy of 34 MeV on a thin 0.2 mg/cm^2 self-supporting natural Tm foil as the target located precisely in the middle of the symmetry axis interconnecting the two Orange spectrometers.

In a first step, conversion electron spectra were generated using both the “big” and the “small” Orange spectrometers. This is done by integrating the events in a window centered onto the electron peak of the plastic scintillator detector spectrum obtained with the current I applied to the Orange spectrometer coils. The measurement were performed in 0.3 A steps each for a measurement time of 10 s. The conversion electron kinetic energy and thus the transition energy is obtained from the relativistic electron momentum which is directly proportional to the current I . This procedure is needed to determine the current positions of the transitions of the interest. In addition, the procedure provides the best test of the experimental setup. As can be seen in Fig. 5.16, no significant deviation between the electron images obtained from the two Orange spectrometers is observed. This is a strong indication that no outside magnetic field is disturbing the setup. This is very important for lifetime measurements, as the earth’s magnetic field distorts the induced toroidal magnetic field which cause a systematic deviation of the lifetime determination due to changes in the path lengths, i.e. the electron time-of-flight (TOF). The disturbing earth’s magnetic field is compensated by using a set of orthogonal Helmholtz-coils. Due to small instabilities in the procedure of compensating the earth’s magnetic field, a possible systematic error < 15 ps has been determined for lifetime measurements using the Orange spectrometer [19]. It should be noted that the direction of the two toroidal magnetic fields point in opposite direction. A significant deviation of the electron images is observed, if the compensation is not well adjusted or even fails.

In analogy to $\gamma\text{-}\gamma$ coincidences, the lifetime measurement is performed by fixing the currents of the two Orange spectrometers on two conversion electron transitions connecting the state of the interest. Fig. 5.17 shows the time distribution of the 2_1^+ state in ^{172}Hf which was measured using K-conversion electrons

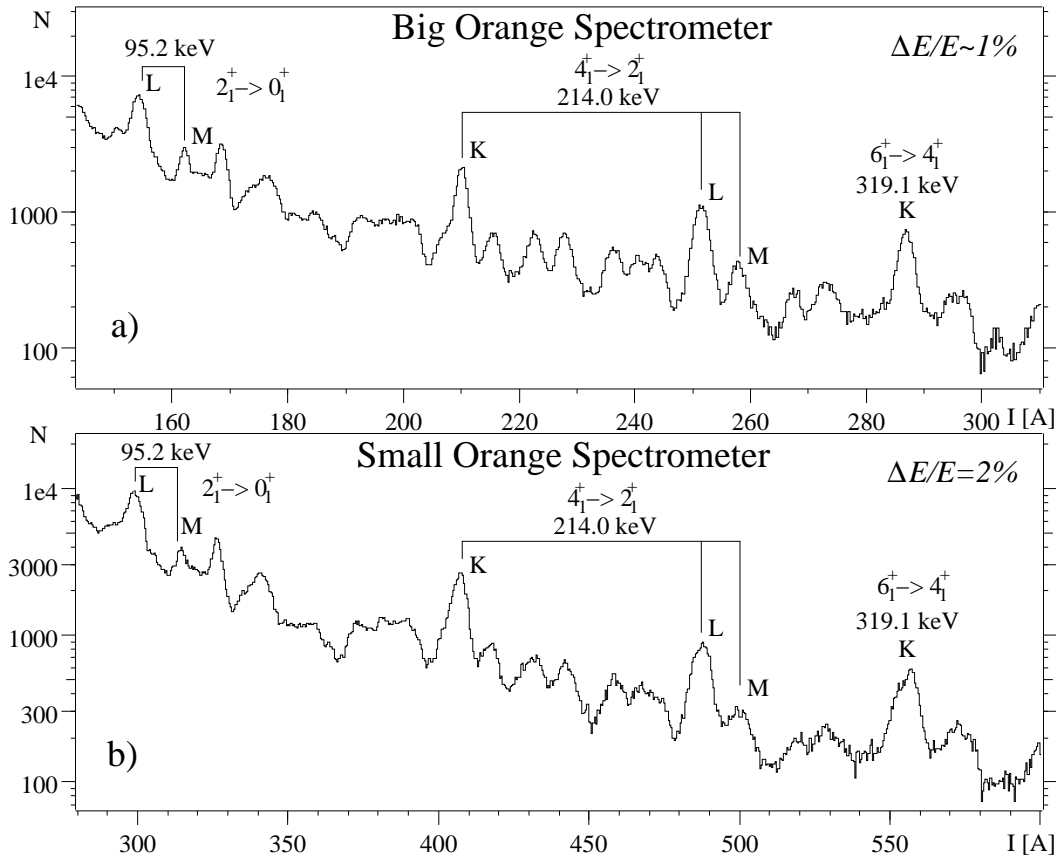


Figure 5.16: Conversion electron spectra of ^{172}Hf obtained using the IKP Orange spectrometers and the same configuration of the compensation of the earth's magnetic field. The background decreasing exponentially with energy (current I) mainly consists of secondary δ -electrons generated in the target or the surrounding material, respectively. b: The slightly worse energy resolution of the small Orange spectrometer is mainly due to reduced number of coils used to produce the toroidal magnetic field (30 compared with 60 for the big Orange spectrometer).

of the directly populating 214 keV transition and the M electrons of the 95.2 keV decay transition, the latter selected by the big Orange spectrometer. Using gates centered onto the electron peaks of the plastic scintillator spectra, the existence of contributions due to time correlated background is hardly verifiable. Fig. 5.18 shows two further results obtained using the L electrons of the 95.2 keV transition and by gating both Orange spectrometers in the two possible ways, analogously to the MSCD method. The time distributions seem to be mirror symmetric. By using the deconvolution method, the lifetimes derived are consistent within the statistical errors of about 20 ps. This result also strongly indicates the effective compensation of the earth's magnetic field.

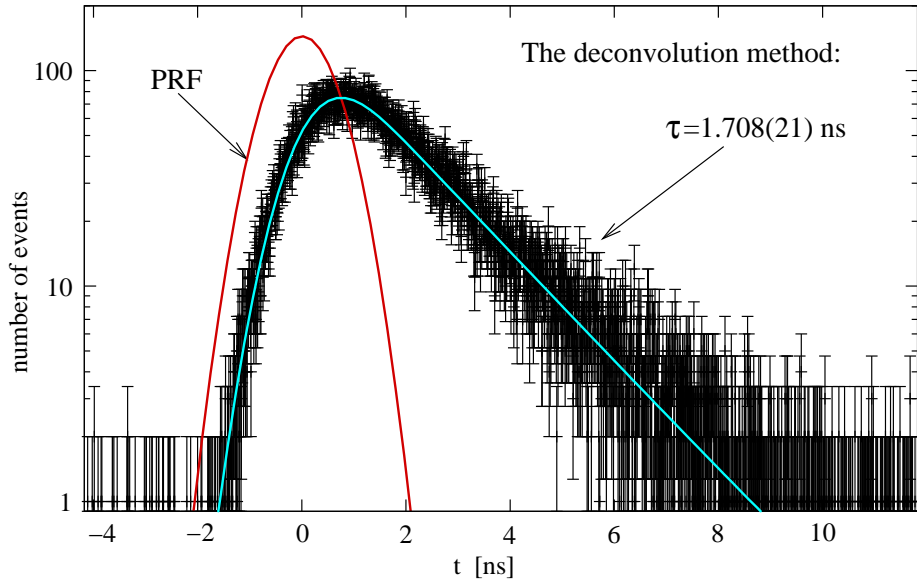


Figure 5.17: e^-e^- time spectrum of the 214 keV (K) \rightarrow 95 keV (M) cascade in ^{172}Hf . The data points are presented with their statistical error bars corresponding to $\Delta N = \sqrt{N}$. Note the extremely smooth distribution of the data which is almost identical to the pure convolution of a Gaussian distribution, the PRF, with an exponential decay [Eq. (2.1)]. Events due to the δ -electron background are uniformly distributed as random coincidence background, as no time correlation is given between the δ -electrons and nuclear transitions. Also, the electron detector situated at 55 cm from the target is shielded against direct γ -ray irradiation from the target using a massive lead cone mounted on the symmetry axis of the spectrometer. Thus, practically no Compton events are detected.

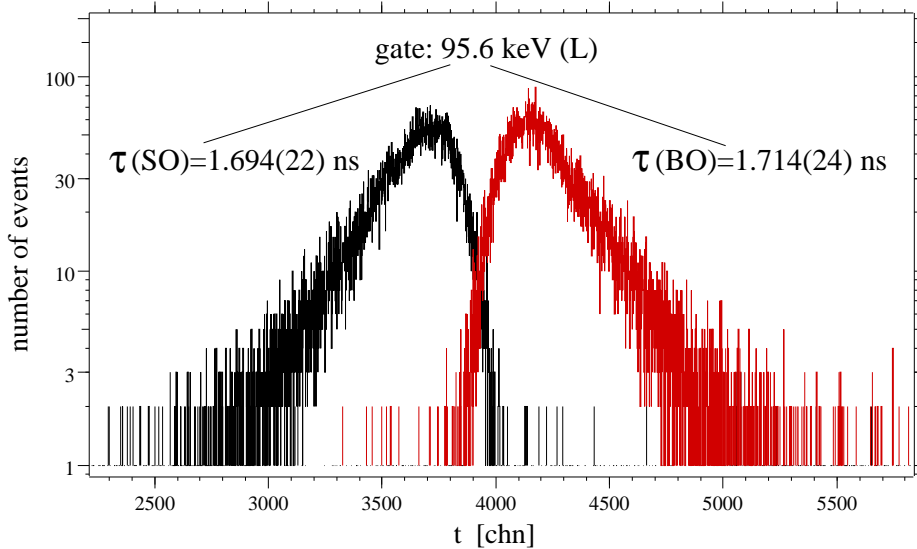


Figure 5.18: e^-e^- time spectra of the 214 keV (K) \rightarrow 95 keV (L) cascade in ^{172}Hf obtained by gating the depopulating 95 keV (L) electron once with the small Orange spectrometer (SO) and once with big Orange spectrometer (BO). Note the nearly mirror symmetric time distributions. It should be noted that the timing of the two spectrometers is strongly asymmetric due to different average path lengths (electron TOF) in the two spectrometers as a result of the different sizes of the spectrometers. Also the time resolution is slightly worse for the small Orange spectrometer due to its slightly worse energy resolution (due to dispersion and focusing defects [19]).

The final result of the lifetime determination for the 2_1^+ state in ^{172}Hf is $\tau(2_1^+) = 1.70(2)$ ns and corresponds to the weighted average of the three results presented in Figs. 5.17 and 5.18 including the possible systematic error of 15 ps as discussed before. The possible time shift due to electronic drifts is neglected, as each result was obtained after only 3-5 hours of measurement and the electronic drift is typically of the order of 10 ps per day [18]. The result of this experiment illustrates the eminent capabilities of the unique Double Orange Spectrometer. It could also be demonstrated that the MSCD method is applicable for picosecond lifetime measurements using the Double Orange Spectrometer [19]. In a pulsed beam experiment, the prompt curves of both spectrometers can be measured separately to be combined for determination of the PRD curve, of which one then obtains the PRD for any energy combination.

5.4 $B(E2)$ systematics in the W and Hf isotopic chains

The $B(E2)$ value of the first excited 2_1^+ state in even-even nuclei is a testing value for nuclear models. In the simple SU(3) limit of the IBA, the $B(E2)$ value increases approximately quadratically with the number of valence bosons. Investigations on the evolution of $E2$ transition strengths within isotopic or isotonic chains provide important information on nuclear structure and potential nuclear shape phase transitions. During the last 50 years, many lifetimes of the first excited 2_1^+ state in even-even nuclei have been measured. However, many of those lifetimes are reported with bad accuracy (e.g., in ^{172}Hf [95]) or with conflicting values (e.g., for ^{174}Hf [95, 96]). This is observed especially for lifetimes which were measured more than 20 years ago. Most of those lifetimes were measured via γ - γ coincidences using Ge-detectors with bad time resolution or using NaI(Tl), BaF₂ and plastic scintillators with bad energy resolution.

In collaboration with several groups, high precision fast timing experiments have been performed to measure two unknown 2_1^+ lifetimes in $^{176,178}\text{W}$ and to improve the accuracy of several $B(E2)$ values in even-even W and Hf isotopes [19, 67, 68]. In Tab. 5.2, lifetimes of first excited 2_1^+ states measured under my participation or by myself (marked with *) are listed with resulting $B(E2)$ values obtained using Eq. (5.12). The highly precise results were obtained using the IKP Double Orange Spectrometer or the γ - γ timing technique with LaBr₃(Ce) detectors, as both presented in this work. The result for ^{176}W is assigned from the e^- - γ timing experiment which was also performed at the IKP, as described in Ref. [19]. Three of five already measured lifetimes could be corrected significantly, in the case of ^{172}Hf by more than 30%. In any case, the relative uncertainty of the lifetimes is merely 2%-3% for the region of about 1 ns. The results demonstrate that many “older” lifetimes are probably incorrect due to experimental limitations at those times and should be re-measured using the now available high-resolution and ultra fast timing techniques, as described in Sections 5.2 and 5.3 and in Ref. [19].

Table 5.2: Lifetimes τ_{exp} of first excited 2_1^+ states in W and Hf isotopes. The results were obtained during my three years of work in collaboration with several groups at the IKP and the Wright Nuclear Structure Laboratory (WNSL) of the Yale University. Results marked with * were determined by myself. RDM is the Recoil Distance Doppler Shift Method and Coul. ex. stands for Coulomb excitation experiments.

nucleus	$\tau_{\text{Lit.}}$ [ns]	technique & reference	τ_{exp} [ns]	$B(E2)$ [(eb) ²]	technique & reference
¹⁷² W	1.06(10)	RDM, [97]	0.97(3)	1.08(3)	e^-e^- , [67]
¹⁷⁴ W	1.64(10)	RDM, [98]	1.34(2)	0.96(2)	$\gamma\text{-}\gamma$, LaBr ₃ (Ce), [68]
¹⁷⁶ W	-	-	1.43(2)*	0.98(2)	e^-e^- , LaBr ₃ (Ce), [19]
¹⁷⁸ W	-	-	1.64(2)	0.91(2)	e^-e^- , [67]
¹⁶⁸ Hf	1.28(8)	RDM, [99]	1.24(2)	0.88(2)	$\gamma\text{-}\gamma$, LaBr ₃ (Ce), [68]
¹⁷² Hf	2.23(15)	$\gamma\text{-}\gamma$ (plastic), [95]	1.70(2)*	1.15(2)	e^-e^- , this work
¹⁷⁴ Hf	2.37(15)	$\gamma\text{-}\gamma$ (plastic), [95]	1.79(2)*	1.18(2)	e^-e^- , [19]
	1.99(13)	Coul. ex., [96]			

In Fig. 5.19, the deduced W and Hf $B(E2)$ values are plotted against the neutron number N (not the boson number N). Experimental $B(E2)$ values of isotopes other than those given in Tab. 5.2 are taken from Ref. [43]. For the Hf isotopes, a smooth evolution of the $B(E2)$ value with increasing N is observed. However, the peaking at N=102 is in disagreement with the collective picture where the peak should be at N=104. Except for the data point at N=98, this same shape is seen in the W isotopic chain. The similarity is remarkable, though ¹⁷²W with N=98 does not fit the systematics.

Theoretical transition strengths were calculated using the SU(3) limit of the IBA and for most cases using the CQF fit parameters (indicated with IBA-1) taken from Refs. [67, 78]. The boson effective charge was derived from the experimental $B(E2)$ value at N=102. For the calculations, $e_B = 0.139$ eb for W and $e_B = 0.142$ eb for Hf were kept constant, assuming e_B does not change substantially over the range of considered nuclei. In contrary to the quadratic increase of transition strength predicted by the IBA, the slope of the $B(E2)$ values towards mid-shell decreases to become flat around mid-shell, as can be seen in Fig. 5.19. This ‘‘saturation effect’’ was recently identified by Z. Berant et al. [100]. The saturation is explained by a reduction of the average proton-neutron interaction [101], which was found at the middle of the rare earth region [102]. Within the IBA, J. Zhang et al. performed calculations by effectively reducing the number of ‘‘active’’ valence bosons [101]. The effective boson number is calculated as follows [101]:

$$N_{\text{eff}}^\iota = N^\iota(1 - fN^\iota), \quad \iota = (\pi, \nu), \quad (5.27)$$

$$N_{\text{eff}} = N_{\text{eff}}^\pi + N_{\text{eff}}^\nu. \quad (5.28)$$

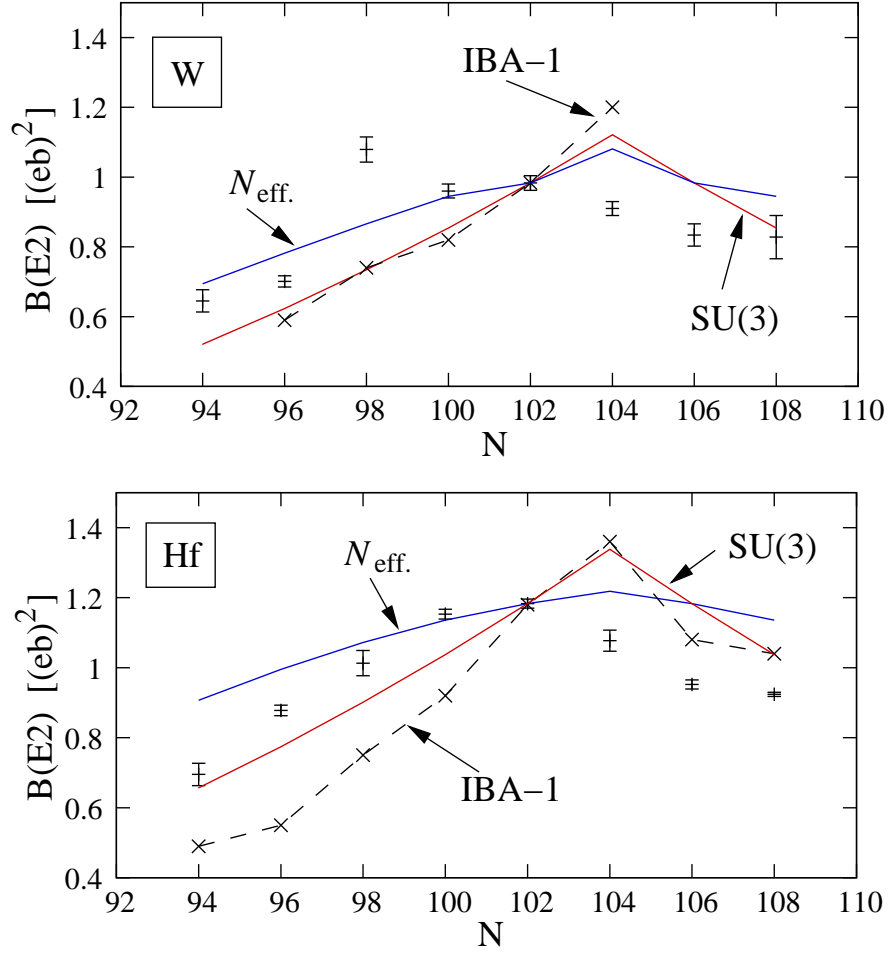


Figure 5.19: Evolution of experimental $B(E2; 2_1^+ \rightarrow 0_1^+)$ values (data points with error bar) of even-even W and Hf isotopes around neutron mid-shell with $N=104$. To guide the eye, the lines connect the calculated values using different models, as indicated. The results are interpreted in the text.

The $B(E2)$ value corresponds to the SU(3) limit and is expressed as [101]:

$$B(E2) = \left(\frac{2N_{\text{eff.}} + 3}{N_{\text{eff.}}} \right) (e_{\pi} N_{\text{eff.}}^{\pi} + e_{\nu} N_{\text{eff.}}^{\nu})^2, \quad (5.29)$$

where $e_{\pi} = 0.18$ and $e_{\nu} = 0.153$ are the effective charges of the proton and neutron bosons [101]. For $f = 0.04$, the observed flattening trend is well reproduced, but due to quadratic dependence on the effective boson number, the peaking is still at $N=104$. The data show much more detailed sub-structure, which should be tested using more microscopic approaches. Especially the large $E2$ ground state transition strength of ^{172}W cannot be described by the IBA. In the geometric model, this deviation can be explained by a contribution due to hexadecapole deformation [103]. For ^{182}W , the hexadecapole deformation parameter β_4 was measured and the corrected $B(E2)$ value again fits to a smooth evolution of the $B(E2)$ values with neutron number [104]. Therefore, it is proposed to determine

β_4 of ^{172}W experimentally [67].

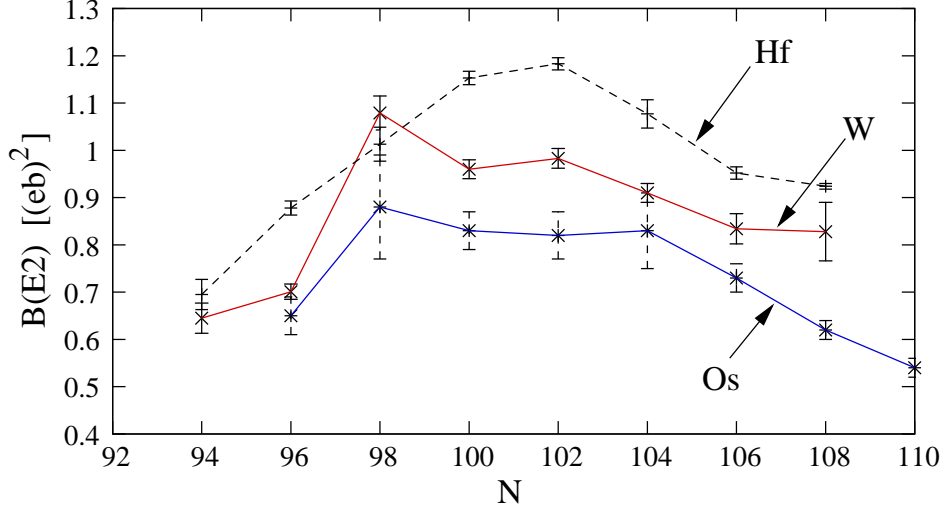


Figure 5.20: Experimental $B(E2 : 2_1^+ \rightarrow 0_1^+)$ systematics around $N=104$ (neutron mid-shell) by increasing the proton boson number N_π from 3 (Os) to 5 (Hf). The data for the Os isotopes are taken from Ref. [43], except for ^{176}Os ($N=100$) [88] and ^{178}Os [89].

For further investigations on $B(E2)$ systematics, the $B(E2)$ values of the Os isotopic chain has also been evaluated, as presented in Fig. 5.20. The previously unknown value for ^{176}Os ($N=100$) has recently been measured by B. Melon [88], so that now the complete Os isotopic chain for $96 \leq N \leq 110$ can be evaluated. It is remarkable that the maximum $B(E2)$ value for Os isotopes seems to be at $N=98$, exactly the same value as for the W isotopes. Also, the Os $B(E2)$ systematics seems to be similar to W and Hf, again when excepting the data point at $N=98$. However, most of the Os $B(E2)$ values have large uncertainties, especially at $N=98$ and $N=104$. Lastly, it is striking that by increasing the proton boson number N_π from three to five, thus going away from closed shell with $Z=82$, a nearly linear increase of the now available experimental $B(E2)$ values independent of the neutron number is observed. This is reproduced by the IBA-1 and also by the IBA-2, where neutron-proton boson symmetry is broken [74].

Further information on the evolution of nuclear structure can be obtained using the Casten triangle of the IBA, as shown in Fig. 5.21. The data points for the Hf and Dy isotopes are taken from Ref. [78], where an extended CQF fit has been performed taking into account more nuclear key observable, as energy ratios, $B(E2)$ ratios as well as the branching ratio $B(E2; 2_2^+ \rightarrow 0_1^+)/B(E2; 2_2^+ \rightarrow 2_1^+)$. In contrast, the W data including ^{176}W taken from Ref. [67] were fitted only on the basis of energy ratios.

In general, starting at neutron closed shell with $N=82$ U(5) like nuclei are expected. As observed by E. A. McCutchan et al. [78], the trajectories of individual isotopic chains from $Z=64$ (Gd) at mid-shell to $Z=72$ (Hf) breaks into two distinct trajectories. Gd, Dy and Er with $64 \leq Z \leq 68$ forming one group and

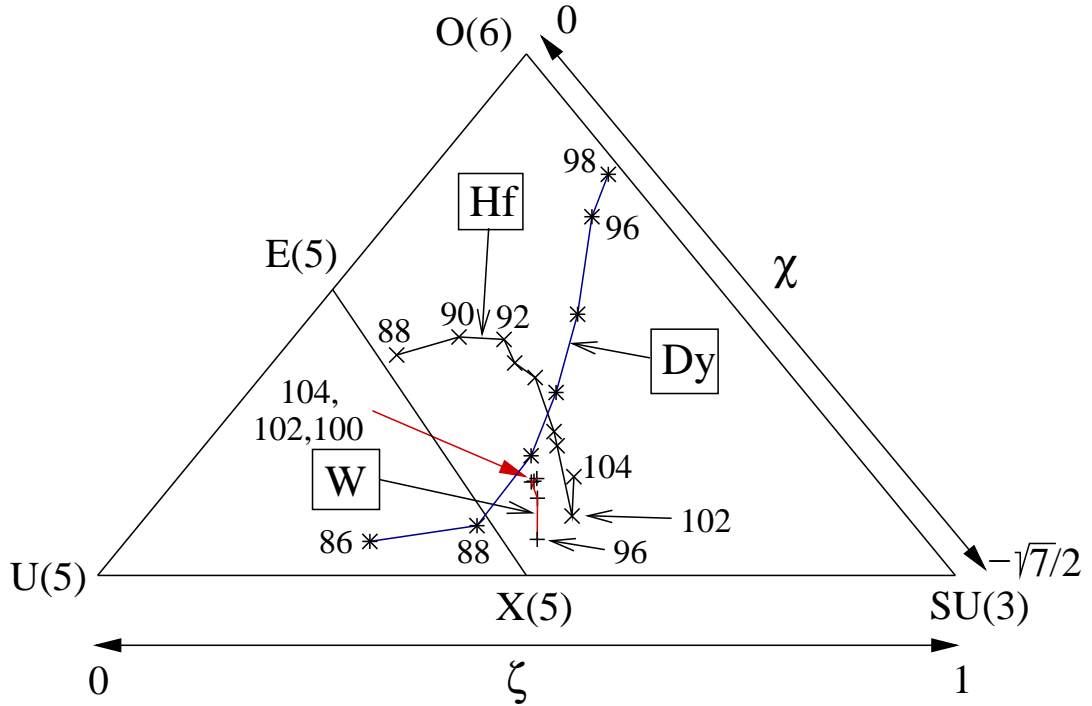


Figure 5.21: Evolution of nuclear structure in the IBA symmetry triangle for the Dy ($Z=66$), Hf ($Z=72$) and W ($Z=74$) isotopic chains. The numerics at the data points indicate the neutron number N . The doubles (ζ, χ) are from Ref. [78] for Dy and Hf; W from Ref. [67]. The results are interpreted in the text.

Yb ($Z=70$) and Hf ($Z=72$) forming the other group. These two groups are represented by the Dy and Hf isotopic chains shown in Fig. 5.21. Near the shape phase transitional region, γ -softness increases with larger Z . Past the phase transition, Dy moves towards the $O(6)$ limit, thus becomes more γ -soft, while Hf becomes more γ -stiff. The W isotopes ($Z=74$), where the parameters of M. Rudigier et al. [67] were used for this analysis, show an unexpected behavior. The W isotopes seem to come from near the $U(5)$ - $SU(3)$ leg and to move towards the $O(6)$ - $SU(3)$ leg, similarly to the trajectory of the Dy isotopic chain with $Z=66$. The different trajectory for Hf is explained to reflect the low-lying 0_2^+ and the high-lying 2_2^+ states in heavier isotopes in contrast to Dy, where the situation is reversed [78]. This statement can not be confirmed by this work. The band head energies in the W isotopes are similar to the Hf isotopes, only energy is reduced for both band heads by about 100 keV.

Recently, a more accurate extended CQF fit taking branching ratios into account has been performed by E. A. McCutchan and N. V. Zamfir for the light W, Os and Pt isotopes [105]. Their results are in agreement with the results presented here. Moreover, the trajectories of the Os ($Z=76$) and Pt ($Z=78$) isotopic chains were found to be similar to W, as shown in Fig. 5.22. The W, Os and Pt isotopes lie rather compact in the center of the Casten triangle and close to shape phase transition region of the IBA.

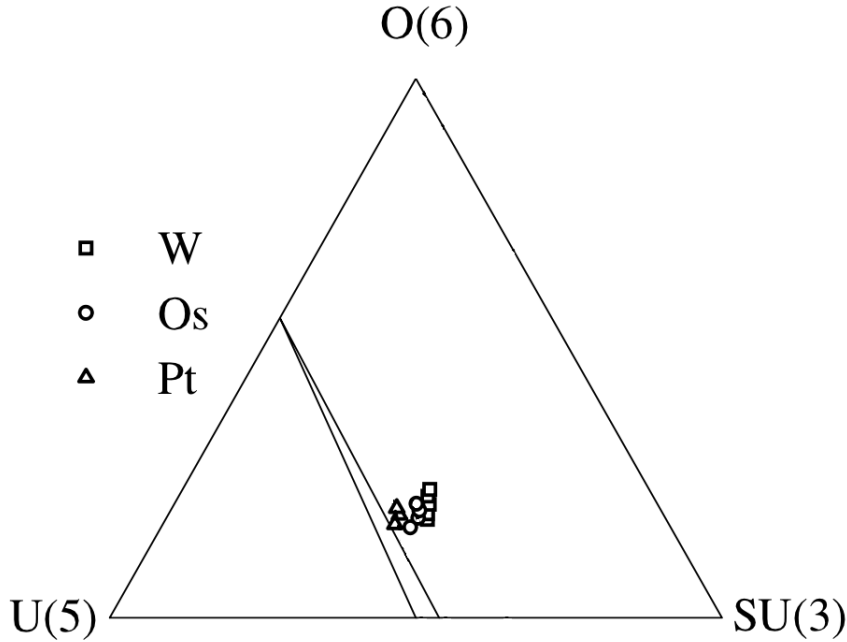


Figure 5.22: Trajectories for the W ($Z=74$, $N=96-104$), Os ($Z=76$, $N=98-104$) and Pt ($Z=78$, $N=100-104$) isotopic chains as derived in Ref. [105]. In any case, the isotopes move towards γ instability when increasing the neutron number. The slanting lines identify the region of X(5) shape phase coexistence for boson number $N = 11$. The figure taken from Ref. [105] is slightly modified.

As observed in Fig. 5.20, the evolution of Os $B(E2)$ values seems to have the same shape of W. Maybe, there is a correlation between the “abnormal” $B(E2)$ peak at $N=98$ and the sudden change of nuclear structure evolution when removing one and more proton bosons (holes) from the Hf isotope. This might be a hint on a possible evolution of sub-shell structure as the major shell is filled with protons, similarly to the Nilsson model for deformed odd A nuclei [106]. Another interesting observation in the structural evolution of Hf is the sudden change of the trajectory direction at $N=102$. This is also observed for the W isotopic chain albeit not that strong. However, the data point belonging to ^{174}Hf ($N=102$) was obtained by using the “old” and false $B(E2; 2_1^+ \rightarrow 0_1^+)$ value, which could be corrected by more than 20%. Hence, a re-evaluation of the CQF fits using the now available corrected and highly accurate $B(E2)$ values for W and Hf should be performed in order to see if the $B(E2)$ peak at $N=102$ is related to a change of the trajectory direction. Although the CQF Hamiltonian in Eq. (5.20) provides the simplest description of deformed nuclei, the results presented in this Section show that CQF analyzes may deliver important indications on nuclear shape evolution and shape phase transitions.

Chapter 6

Conclusions and outlook

This work provides a complete theoretical and experimental description of the fast timing technique. Extended fast timing measurements have been performed at the IKP and also at different institutes of nuclear physics around the world. Few of the experiments are published so far and also briefly reported in this work. The overall properties of the $\text{LaBr}_3(\text{Ce})$ scintillator, the XP2020 and XP20D0 PMTs and the standard CFD (model ortec 584 and 935) have been investigated. The work reports on impressive agreements between the experimental data and the theories on fast timing. For the first time, the prompt curve of a fast timing setup is identified with the CFD time-walk characteristics independent of the scintillator material and the PMT used. This provides a universal fast timing calibration function for cases in which a CFD is used for timing. Using the $\text{LaBr}_3(\text{Ce})$ and the non-linear XP20D0 PMT as detector assembly, lifetime measurements in the energy region $50 \text{ keV} < E_\gamma < 1510 \text{ keV}$ with absolute time resolving power of $\Delta\tau \approx 4 \text{ ps}$ are feasible. Compared with the XP2020, the XP20D0 PMT provides better time jitter by factor of up to 1.2. However, a linear PMT response in a large range of operation voltages would provide better time-walk characteristics and therefore, one should test other PMTs.

The identification of the time-walk characteristics has brought forth a new favorable method for analyzes of time distributions from a two detector timing system detecting two coincident nuclear transitions. The MSCD method substantially simplifies the analysis by just measuring the centroid difference of a cascade. Compared with the prompt curve determination of a single detector, the MSCD method cancels the possible systematic errors of timing asymmetries, electronic drifts and in γ - γ timing also from the geometrical point of view. Therefore, lonesome investigations on these problems are dropped out. A highly precise procedure to calibrate the PRD curve of the setup has been introduced. Due to imperative mirror symmetry of the MSCD method, additional data points are obtained for a more precise PRD calibration. Using the ^{152}Eu γ -ray source, the PRD curve for $240 \text{ keV} < E_\gamma < 1300 \text{ keV}$ is calibrated very precisely. This energy region often equates to the region of the interest. For lower energies, the ^{133}Ba source or, more accurately due to better peak-to-background ratio, the ^{226}Ra source can be used to provide a PRD at 53 keV.

Indeed, the only possible error that can be induced in MSCD analyzes using γ -rays is due to background contributions to the time spectra. For the first time, the origin of the background obtained in γ -ray spectroscopy with scintillators has been identified. For $E_\gamma > 350$ keV, the background mainly consist of the Compton continuum of higher energy γ -rays. It is shown that the time response of the full energy events is delayed relative to Compton events as a result of a contribution of multiple Compton interactions in creation of the full energy event. In contrast, the low-energy background for $E_\gamma < 350$ keV results from coincident γ -rays, but which were generated after a primary interaction in the surrounding material and includes the cross-talk events. It is shown that this extremely delayed (relative to full energy events) low-energy background is considerably reduced by using active BGO shielding. This can become the essential for fast timing in the low-energy region.

This work reports on high precision determination of nine lifetimes in five isotopes, five lifetimes were determined for the first time. Previously published assumptions on the structure of ^{214}Po and ^{214}Bi could be confirmed due to improved experimental accuracy. In collaboration with several groups, further four important 2_1^+ lifetimes in four rare earth isotopes have also been measured or re-measured, respectively. In total seven 2_1^+ lifetimes were determined with relative accuracy of only 2%-3%. These lifetimes allowed for a simplified analysis of nuclear shape evolution in the $170 \leq A \leq 180$ mass region. Overall, and in agreement with the IBA, a smooth evolution of $B(E2)$ values with peaking around neutron mid-shell is observed. The $B(E2)$ value increases nearly linearly with the proton boson number. However, there is evidence for sub-structures which manifest by $B(E2)$ peaks at $N=98$ and $N=102$, not at neutron mid-shell with $N=104$ as expected from the simple collective model. The deviations from smooth evolution may be a hint for a change of the sub-shell structure. It would be interesting to analyze the sub-structure with regard on the Nilson model for neighboring deformed odd- A nuclei. The evolution of nuclear shape observed in the symmetry triangle of the IBA seems to provide some kind of a new structural signatures. A change of the nuclear shape evolution trajectory direction is observed for the W and Hf isotopic chains at $N=102$. Both, experimental transition strengths and IBA calculations using the CQF for nuclear shape evolution analysis show changes at $N=102$. Also, a sudden change of shape evolution between the neighboring W and Hf isotopic chains is observed. This might be related to the ‘‘abnormal’’ $B(E2)$ peak at $N=98$ for W and Os, which both follow similar evolution trajectories in the Casten triangle. These preliminary observations should be investigated in more detail using different approaches within the CQF fit, e.g. using only energy ratios. Some 2_1^+ lifetimes in the light even-even Os and Pt isotopes should be measured or re-measured in order to provide accurate $B(E2; 2_1^+ \rightarrow 0_1^+)$ values for a more qualitative exploration of $B(E2)$ systematics.

The transition energy of the first excited 2^+ state in well deformed nuclei of the rare earth region is typically in the range of 100 keV and the lifetime is typically in the range of 1 nanosecond. The unique IKP Double Orange Spectrometer is ideally suited for lifetime determination in this energy and time domain. Virtually, no background contribute to the time distribution of the e^-e^- coincidence mode.

Especially for low energy transitions, the e^-e^- timing technique is effective due to high electron transmission of 10%-20% per Orange spectrometer and the rapid increase of internal conversion with decreasing transition energy. It is scheduled to perform high precision e^-e^- fast timing experiments for determination of unknown and uncertain 2_1^+ lifetimes in the rare earth region. The $e^- \gamma$ timing technique is promising, as in parallel $\gamma\text{-}\gamma$ coincidences can be analyzed using the MSCD method. This is important for high-energy transitions, as internal conversion decreases with $E_\gamma^{-(l+3/2)}$, l being the transition multipolarity. Thus, the $e^- \gamma$ timing technique combines the particular advantages of the Orange spectrometer and the LaBr₃(Ce) detectors and furthermore improves the peak-to-background ratio in the γ -ray spectra by factor 2. Using additional active background suppression, the $e^- \gamma$ time spectra will be very clean. For complex decay schemes, as observed in heavy odd-A and odd-odd nuclei, the big Orange spectrometer can be used as an additional trigger to perform $e^- \gamma \gamma$ triple coincidences. The absolute limitation of the lifetime determination using the Orange spectrometers is actually about 20 ps. This limit can be reduced to about 5 ps using the $\gamma\text{-}\gamma$ timing technique in combination with the MSCD method.

Appendix A

The background correction procedure of the MSCD method

In γ -ray spectroscopy the full energy peaks of interest are sitting on background, as shown in Fig. A.1. Mainly, the background consists of the Compton continuum which are caused by γ -rays of higher energies. Using a compact detector array, also cross-talk events and scattered γ -rays from the surrounding can play a role. Using active Compton shielding, the background is remarkably reduced, but still some amount of background is obtained, as part of this background is generated from coincident γ -rays.

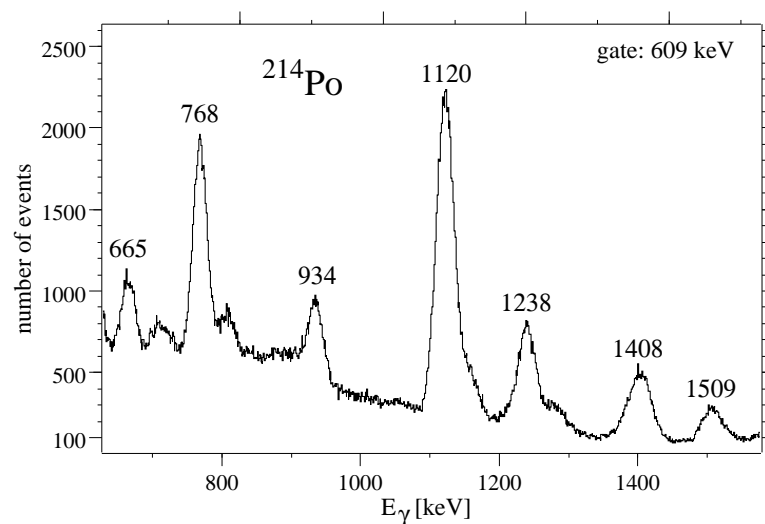


Figure A.1: Coincidence γ -ray spectrum of the 609 keV ground state transition in ^{214}Po . Note the large Compton background for energies below 1000 keV.

The measured time distribution is a superposition of the time spectra due to full energy events and due to Compton events of same energy, i.e. the background underneath the full energy peak. The Compton time distribution of the interest can be interpolated by the measurements of Compton time spectra at different energies in the region around the transition of interest [12, 14]. For the MSCD method, the procedure is analogous, but the centroid difference of the two Compton time distributions obtained from each branch for a certain energy combination is measured instead. Such an analysis is presented in Fig. A.2, where the 609 keV full energy peak of ^{214}Po was used as the reference energy gate and the Compton gates were varied in the range of 630-1450 keV.

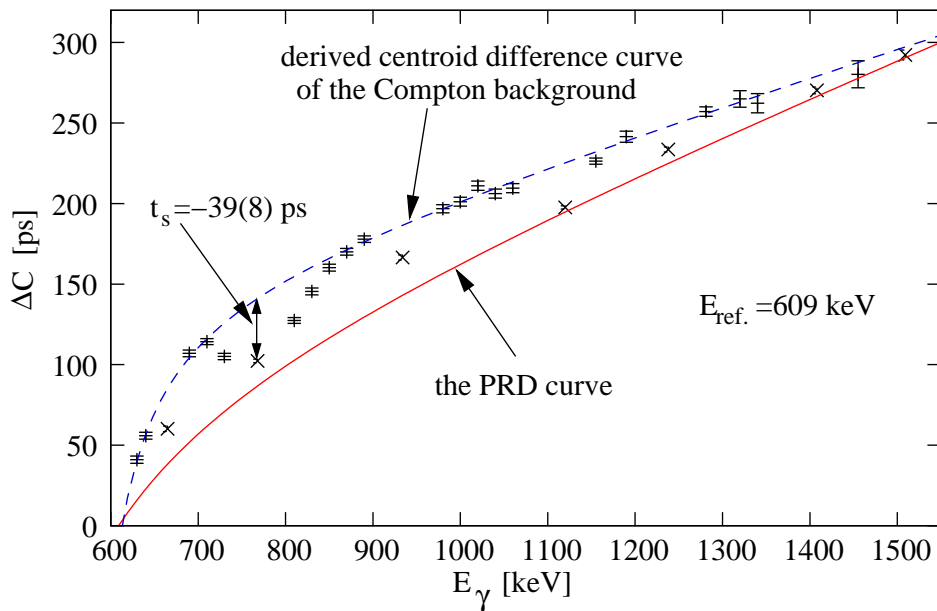


Figure A.2: 609 keV gated Compton centroid differences compared with the full energy 609 keV gated centroid differences of the 2_1^+ state in ^{214}Po indicated by crosses. The PRD curve for the reference energy of 609 keV is also shown.

The overall behavior the Compton centroid differences is quite smooth. The structure is due to contributions of the full energy events. Therefore, only the Compton data points located outside the complete full energy peaks were fitted, as can be seen in Fig. A.2. As one example, the interpolated shift $t_s = \Delta C_T - \Delta C_C$ between the (total) full energy centroid difference and the Compton centroid difference curve at $E_\gamma = 768$ keV is $t_s = -39(8)$ ps. As a linear combination of centroids, the total centroid difference ΔC_T can be written as the sum of the true delayed (or prompt) centroid difference ΔC_D and the Compton centroid difference ΔC_C :

$$\Delta C_T = \frac{\Delta C_D + \alpha \Delta C_C}{1 + \alpha} = \Delta C_D + t_c, \quad (\text{A.1})$$

where α is the relative background intensity or the background-to-peak ratio, respectively. Eq. (A.1) is only valid, if the two timing branches have the same peak-to-background ratio, which was approximately the case in this experiment. The mean value obtained from the two timing branches is used and an adopted systematic error of 10% which is overestimated is taken into account. To obtain the correction term t_c , Eq. (A.1) is equivalent to:

$$\begin{aligned}
 t_c = \Delta C_T - \Delta C_D &= -\alpha(\Delta C_T - \Delta C_C) = -\alpha t_s \\
 \iff \Delta C_D &= \Delta C_T + \alpha t_s.
 \end{aligned}
 \tag{A.2}$$

The background-to-peak ratio of the 768 keV transition is obtained from the 609 keV gated coincidence spectrum using the same gates as for timing measurements. Due to background-to-peak ratio of $\alpha = 0.3$, the value of the total centroid difference ΔC_T for the combination 768-609 keV has to be corrected by $-11.7(2.6)$ ps to obtain the true centroid difference ΔC_D . Analogous studies were made for all γ -rays involved in lifetime determination for this work. For very good peak-to-background ratios of more than 10, the resulting additional error is smaller than 1 ps, thus negligibly small.

Bibliography

- [1] W. Crookes, Certain Properties of the Emanations of Radium. Chemical News; Vol. 87, 241 (1903).
- [2] S. Curran, Scintillation counter, theory and application, Accademic Press New York (1949).
- [3] W. E. Stephens, A Pulsed Mass Spectrometer with Time Dispersion, Phys. Rev. 69, 691 (1946).
- [4] W. H. Sweet; G. L. Brownell, Localization of brain tumors with positron emitters, Nucleonics 11, 40 (1953).
- [5] E. R. Bell in: Kai Siegbahn, Editor, Beta and Gamma Ray Spectroscopy, North-Holland Publishing Co, Amsterdam (1955).
- [6] A. Schwarzschild, A survey of the latest developments in delayed coincidence measurements, Nucl. Instrum. Methods 21 (1963).
- [7] R. Hofstadter, The Detection of Gamma-rays with Thallium-Activated Sodium Iodid Crystals, Phys. Rev. 75, 796 (1949).
- [8] F. Lynch, Improved timing with NaI(Tl), IEEE Trans. Nucl. Sci. NS-13, no. 3, 140 (1966).
- [9] J. Burde and S. G. Cohen, Determination of the Lifetime of the 40-keV Excited State of $^{81}\text{Tl}^{208}$ Following Alpha Decay Using Recoil Shifts of the Conversion Electrons, Phys. Rev. 104, 1093 (1956).
- [10] M. S. El-Nesr and E. Bashandy, Lifetime measurement of the 84 keV transition in ^{170}Yb , Zeitschrift für Physik 168, 349 (1962).
- [11] R. L. Chase, Pulse timing system for use with gamma rays on Ge(Li) detectors, Rev. Sci. Instrum. 39, 1318 (1968).
- [12] H. Mach et al., A method for picosencond lifetime measurements for neutron rich nuclei (1), Nucl. Instrum. Methods A280, 49 (1989).
- [13] M. Moszyński et al., A method for picosencond lifetime measurements for neutron rich nuclei (2), Nucl. Instrum. Methods A277, 407 (1989).

- [14] H. Mach et al., Retardation of $B(E2; 2_1^+ \rightarrow 0_1^+)$ rates in $^{90-96}\text{Sr}$ and strong subshell closure effects in the A 100 region, *Nucl. Phys. A* 523, 197 (1991).
- [15] E. V. D. van Loef et al., Scintillation Properties of $\text{LaBr}_3:\text{Ce}^{3+}$ Crystals: Fast, Efficient, and High-Energy Resolution Scintillators, *Nucl. Instrum. Methods Phys. Res. A* 486, 254 (2002).
- [16] A. Iltis et al., Lanthanum halide scintillators: Properties and applications, *Nucl. Instrum. Methods Phys. Res. A* 563, 359 (2006).
- [17] M. Moszyński et al., New Photonis XP20D0 photomultiplier for fast timing in nuclear medicine, *Nucl. Instrum. Methods Phys. Res. A* 567, 31 (2007).
- [18] J.-M. Régis et al., The mirror symmetric centroid difference method for picosecond lifetime measurements via γ - γ coincidences using very fast $\text{LaBr}_3(\text{Ce})$ scintillator detectors, *Nucl. Instrum. Methods Phys. Res. A* 622, 81 (2010).
- [19] J.-M. Régis et al., Sub-Nanosecond Lifetime Measurements using the Double Orange Spectrometer at the Cologne 10 MV Tandem Accelerator, *Nucl. Instrum. Methods Phys. Res. A* 606, 466 (2009).
- [20] L. Bettermann et al., Lifetime measurement of excited states in the shape-phase-transitional nucleus ^{98}Zr , *Phys. Rev. C* 82, 044310 (2010).
- [21] J.-M. Régis et al., Improvement of the intrinsic time resolving power of the Cologne iron-free Orange type electron spectrometers, *Rev. Sci. Instrum.* 81, 113505 (2010).
- [22] E. R. White et al., Lifetime measurement of the 167.1 keV state in ^{41}Ar , *Phys. Rev. C* 76, 057303 (2007).
- [23] L. G. Hyman et al., Study of high speed photomultiplier systems, *Rev. Sci. Instrum.* 35, 393 (1964).
- [24] L. G. Hyman, Time resolution of photomultiplier systems, *Rev. Sci. Instrum.* 36, 193 (1965).
- [25] “Experimental techniques in high-energy nuclear and particle physics” by T. Ferble, World Scientific Publishing, Singapor (1991).
- [26] W. R. Leo, *Techniques for nuclear and particle physics experiments*, Springer (1987).
- [27] K. S. Shah et al., $\text{LaBr}_3:\text{Ce}$ Scintillators for Gamma Ray Spectroscopy, *IEEE Trans. Nucl. Sci.* 50, 2410 (2003).
- [28] P. B. Lyons and J. Stevens, Time response of plastic scintillators, *Nucl. Instrum. Methods* 114, 313 (1974).
- [29] C. A. Parker and C. G. Hatchard, Delayed Fluorescence from Solutions of Anthracene and Phenanthrene, *Proc. Roy. Soc. A* 269, 574 (1962).

- [30] M. Laval et al., Barium fluoride - Inorganic scintillator for subnanosecond timing, *Nucl. Instrum. Methods* 206, 169 (1983).
- [31] P. Dorenbos, J. T. M. de Haas and C. W. E. van Eijk, Non-Proportionality in the Scintillation Response and the Energy Resolution Obtainable with Scintillation Crystals, *IEEE Trans. Nucl. Sci.*, vol 42, 2190 (1995).
- [32] M. Conti et al., Comparison of fast scintillators with TOF PET potential, *IEEE Trans. Nucl. Sci.*, vol 56, 926 (2009).
- [33] *Photomultiplier Tubes; Basics and Applications*, edited by Hamamatsu Photonics K. K., 138 (2006).
- [34] B. Leskovar and C.C. Lo, Single photoelectron time spread measurement of fast photomultipliers, *Nucl. Instrum. and Methods* 123, 145 (1975).
- [35] C. R. Kerns, Photomultiplier single-electron time-spread measurements, *IEEE Trans. Nucl. Sci. NS-14* (1), 449 (1967).
- [36] B. Bengston and M. Moszyński, Timing improved by the use of dynode signals studied with different scintillators and photomultipliers, *Nucl. Instrum. and Methods* 204, 129 (1982).
- [37] F. Calligaris et al., Wavelength dependence of timing properties of the XP2020 photomultiplier, *Nucl. Instrum. and Methods* 157, 611 (1978).
- [38] J. Glodo et al., Effects of Ce concentration on scintillation properties of LaBr₃:Ce, *IEEE Trans. Nucl. Sci.*, vol 52, 1805 (2005).
- [39] M. Moszyński, Timing properties of Philips XP2020UR photomultiplier, *Nucl. Instrum. Methods Phys. Res. A* 324, 269 (1993).
- [40] T. J. Paulus, Timing electronics and fast timing methods with scintillation detectors, *IEEE Trans. Nucl. Sci. NS-32/3*, 1242 (1985).
- [41] H. Spieler, Fast timing methods for semiconductor detectors, *IEEE Trans. Nucl. Sci. NS-29/3*, 1142 (1982).
- [42] Z. Bay, Calculations of decay times from coincidence experiments, *Phys. Rev.* 77, 419 (1950).
- [43] National Nuclear Data Center, <www.nndc.bnl.gov>.
- [44] J. B. Birks, *The theory and practice of scintillation counting*, Pergamon Press, 662 (1964).
- [45] N. Mărginean et al., In-beam measurements of sub-nanosecond nuclear lifetimes with a mixed array of HPGe and LaBr₃:Ce detectors, *Eur. Phys. J. A* 46, 329 (2010).

- [46] Z. Berant et al., Spectroscopy of ^{214}Bi and systematics of $^{210,212,214}\text{Pb}(0^+) \xrightarrow{\beta^-} ^{210,212,214}\text{Bi}(0^-)$, Phys. Rev. C 43, 1639 (1991).
- [47] J. B. McGrory and T. T. S. Kuo, Shell model calculations of two to four identical-”particle” systems near ^{208}Pb , Nucl. Phys. A 247, 283 (1975).
- [48] P. F. A. Klinkenberg, Tables of Nuclear Shell Structure, Rev. Mod. Phys. 24, 63 (1952).
- [49] R. D. Woods and D. S. Saxon, Diffuse Surface Optical Model for Nucleon-Nuclei Scattering, Phys. Rev. 95, 577 (1954).
- [50] C. Ellegaard et al., Experimental evidence for particle-vibration coupling in ^{209}Pb , Phys. Lett. 25B, 512 (1967).
- [51] N. Auerbach and N. Stein, Single-Particle Structure in the Lead Region, Phys. Lett. 28B, 628 (1969).
- [52] E. Caurier et al., Large-scale shell model calculations for the N=126 isotones Po-Pu, Phys. Rev. C 67, 054310 (2003).
- [53] E. K. Warburton, Mesonic enhancement of the weak axial-vector current evaluated from β decay in the lead region, Phys. Rev. Lett. 66, 1823 (1991).
- [54] E. Caurier, Full pf shell model study of A=48 nuclei, Phys. Rev. C 50, 225 (1994).
- [55] T. T. S. Kuo, Particle-hole multiplets in ^{208}Bi , Nucl. Phys. A 122, 325 (1968).
- [56] T. T. S. Kuo and G. H. Herling, NRL Memorandum Report No. 2258 (1971).
- [57] I. Talmi in Interacting Bosons in Nuclear Physics, edited by F. Iachello, Plenum, New-York (1979).
- [58] H. W. Taylor et al., Mixing parameters of gamma transitions in ^{214}Po , Phys. Rev. C 34, 2322 (1986).
- [59] H. W. Taylor and B. Singh, Evidence for collective structure in ^{214}Po , Phys. Rev. C 40, 449 (1989).
- [60] G. Scharff-Goldhaber and J. Weneser, Systems of Even-Even Nuclei, Phys. Rev. 98, 212 (1955).
- [61] A. Arima and F. Iachello, Interacting boson model of collective states I. The vibrational limit, Ann. Phys. 99, 253 (1976).
- [62] S. T. Ahmad et al., Mixed symmetry states and structure of ^{200}Hg , J. Phys. G; Nucl. Part. Phys. 15, 93 (1989).
- [63] K. Kumar and M. Baranger, Nuclear deformations in the pairing-plus-quadrupole model: (V). Energy levels and electromagnetic moments of the W, Os and Pt nuclei, Nucl. Phys. A 122, 273 (1968).

- [64] R. F. Casten and J. A. Cizewski, The $O(6) \rightarrow$ rotor transition in the Pt-Os nuclei, *Nucl. Phys. A* 309, 477 (1978).
- [65] R. F. Casten, $N_p N_n$ systematics in heavy nuclei, *Nucl. Phys. A* 443, 1 (1985).
- [66] C. Y. Wu et al., Quadrupole collectivity and shapes of Os-Pt nuclei, *Nucl. Phys. A* 607, 178 (1996).
- [67] M. Rudigier et al., Lifetime of the first 2^+ state in ^{172}W and ^{178}W , *Nucl. Phys. A* 847, 89 (2010).
- [68] V. Werner et al., Excited State Lifetime Measurements in Rare Earth Nuclei with Fast Electronics, INPC2010, accepted (2010).
- [69] A. Bohr and B. Mottelson, Report of the International Physics Conference, Copenhagen, June, 1952; *Kgl. Danske Vid. Selsk. Mat. Fys. Medd.* 27, 16 (1953).
- [70] A. Arima and F. Iachello, Collective Nuclear States as Representations of a $SU(6)$ Group, *Phys. Rev. Lett.* 35, 1069 (1975).
- [71] F. Iachello and A. Arima, *The Interacting Boson Model*, Cambridge University Press (1987).
- [72] G. Andersson et al., Nuclear shell structure at very high angular momentum, *Nucl. Phys. A* 268, 205 (1976).
- [73] G. Gneuss and W. Greiner, Collective potential energy surfaces and nuclear structure, *Nucl. Phys. A* 171, 449 (1971).
- [74] R. F. Casten, *Nuclear structure from a simple perspective*, Oxford University Press Inc. (2000).
- [75] H. Morinaga and T Yamazaki, In *beam Gamma-ray Spectroscopy*, North Holland Publishing (1976).
- [76] G. Alaga et al., Intensity rules for β and γ transitions to nuclear rotational states, *Danske Vid. Selsk. Mat. Fys. Medd.* 29, 16 (1955).
- [77] D. D. Warner and R. F. Casten, Revised Formulation of the Phenomenological Interacting Boson Approximation, *Phys. Rec. Lett.* 48, 1395 (1982).
- [78] E. A. McCutchan et al., Mapping the interacting boson approximation symmetry triangle: New trajectories of structural evolution of rare-earth nuclei, *Phys. Rev. C* 69, 064306 (2004).
- [79] A. E. L. Dieperink et al., Classical limit of the Interacting-Boson model, *Phys. Rec. Lett.* 44, 1747 (1980).
- [80] F. Iachello, Dynamical Symmetries at the Critical Point, *Phys. Rev. Lett.* 85, 3580 (2000).

- [81] F. Iachello, Analytical description of Critical Point Nuclei in a Spherical - Axially Deformed Shape Phase Transition, *Phys. Rev. Lett.* 87, 052502 (2001).
- [82] L. Landau, *Collected Papers of Landau*, Pergamon Press, Oxford (1965).
- [83] J. Jolie et al., Triple Point of Nuclear Deformations, *Phys. Rev. Lett.* 89, 182502 (2002).
- [84] M. A. Caprio and F. Iachello, Analytic Descriptions for Transitional Nuclei near the Critical point, *Nucl. Phys. A* 781, 26 (2007).
- [85] V. Werner et al., Singular character of critical points in nuclei, *Phys. Lett. B* 527, 55 (2002).
- [86] R. Krücken et al., B(E2) Values in ^{150}Nd and the Critical Point Symmetry X(5), *Phys. Rev. Lett.* 88, 232501 (2002).
- [87] D. Tonev et al., Transition probabilities in ^{154}Gd : Evidence for X(5) critical point symmetry, *Phys. Rev. C* 69, 034334 (2004).
- [88] B. Melon, PhD thesis, University of Cologne (2011).
- [89] A. Dewald et al., Test of the critical point symmetry X(5) in the mass A=180 region, *J. Phys. G. : Nucl. Part. Phys.* 31, S1427 (2005).
- [90] R. F. Casten and N. V. Zamfir, Evidence for a Possible E(5) Symmetry in ^{134}Ba , *Phys. Rev. Lett.* 85, 3584 (2000).
- [91] A. Dewald et al., privat communication.
- [92] J.-M. Régis et al., Nuclear structure analysis using the Orange Spectrometer, *AIP CP* 1090, 112 (2008).
- [93] R. M. Diamond et al., Centrifugal Stretching of Nuclei, *Phys. Rev. Lett.* 11, 315 (1964).
- [94] M. A. J. Mariscotti et al., Phenomenological Analysis of Ground-state Bands in Even-Even Nuclei, *Phys. Rev.* 178, 1864 (1969).
- [95] H. Abou-Leila, Determination des Moments d'Inertie et des Deformations a Partir des Mesures des Perodes Courtes dans les Noyaux Pair-Pair Deformes, *Ann. Phys. (Paris)* 2, 181 (1967).
- [96] H. Ejiri and G. B. Hagemann, Electromagnetic transitions from levels in the beta-vibrational band of ^{174}Hf , *Nucl. Phys. A* 161, 449 (1971).
- [97] F. K. McGowan et al., Transition quadrupole moments of high-spin states in ^{172}W and their implications for the interpretation of band crossings in the light isotopes of W to Pt, *Nucl. Phys. A* 530, 490 (1991).
- [98] J. Gascon et al., Shape variation of ^{174}W below the $i_{13/2}$ backbend, *Nucl. Phys. A* 472, 558 (1987).

- [99] B. Bochev et al., Feeding and lifetimes of yrast levels in Hf nuclei, Nucl. Phys. A 282, 159 (1977).
- [100] Z. Berant et al, g-factor of the 2_1^+ state of ^{164}Yb , Phys. Rev. C 69, 034320 (2004).
- [101] J. Zhang et al., Consistent interpretation of $B(E2)$ values and g factors in deformed nuclei, Phys. Rev C 73, 037301 (2006).
- [102] R. B. Cakirli et al., Proton-Neutron Interactions and the New Atomic Masses, Phys. Rev. Lett. 94, 092501 (2005).
- [103] N. V. Zamfir et al., Hexadecapole deformations in actinide and trans-actinide nuclei, Phys. Lett. B 357, 515 (1995).
- [104] C. E. Bemis et al., Interference Between Direct Nuclear Reactions and Coulomb Excitation with Alpha Particles on ^{154}Sm , ^{166}Er , and ^{182}W , Phys. Rev. C 8, 1934 (1973).
- [105] E. A. McCutchan and N. V. Zamfir, Simple description of light W, Os and Pt nuclei in the interacting boson model, Phy. Rev. C 71, 054306 (2005).
- [106] S. G. Nilsson, Binding States of Individual Nucleons in Strongly Deformed Nuclei, Mat. Fys. Medd. Dan Vid. Selsk. 29 No. 16 (1955).

Publications

S. Kisiov, S. Lalkovski, N. Mărginean, D. Bucurescu, L. Atanasova, D. L. Balabanski, Gh. Cata-Danil, I. Cata-Danil, J.-M. Daugas, D. Deleanu, P. Detistov, D. Filipescu, G. Georgiev, D. Ghita, T. Glodariu, J. Jolie, D. S. Judson, R. Lozeva, R. Marginean, C. Mihai, A. Negret, S. Pascu, D. Radulov, J.-M. Régis, M. Rudigier, T. Sava, L. Stroe, G. Suliman, N. V. Zamfir, K. O. Zell and M. Zhekova, *In-beam fast-timing measurements and the structure of the $7/2_1^+$ and $11/2_1^+$ states in $^{103,105,107}\text{Cd}$* , to be submitted.

M. G. Procter, D. M. Cullen, C. Scholey, P. T. Greenlees, J. Hirvonen, U. Jakobsson, P. Jones, R. Julin, S. Juutinen, S. Ketelhut, M. Leino, N. M. Lumley, P. J. R. Mason, P. Nieminen, M. Nyman, A. Puurunen, P. Peura, P. Rahkila, J.-M. Régis, P. Ruotsalainen, J. Sar, Y. Shi, J. Sorri, S. Stolze, J. Uusitalo, and F. R. Xu, *High-K four-quasiparticle states in ^{138}Gd* , to be submitted.

T. Thomas, C. Bernards, J.-M. Régis, M. Albers, C. Fransen, S. Heinze, J. Jolie, D. Radeck, and K.-O. Zell, *Bose-Fermi Symmetry in ^{193}Au* , submitted to Phys. Rev. C (2011).

J.-M. Régis, Th. Materna, G. Pascovici, S. Christen, A. Dewald, C. Fransen, J. Jolie, P. Petkov and K. O. Zell, *Improvement of the intrinsic time resolving power of the Cologne iron-free Orange type electron spectrometers*, Rev. Sci. Instrum. 81, 113505 (2010).

L. Bettermann, J.-M. Régis, Th. Materna, J. Jolie, U. Köster, K. Moschner and D. Radeck, *Lifetime measurement of excited states in the shape-phase-transitional nucleus ^{98}Zr* , Phys. Rev. C 82, 044310 (2010).

J.-M. Régis, G. Pascovici, J. Jolie and M. Rudigier, *The mirror symmetric centroid difference method for picosecond lifetime measurements via γ - γ coincidences using very fast $\text{LaBr}_3(\text{Ce})$ scintillator detectors*, Nucl. Instrum. Methods Phys. Res. A 622, 81 (2010).

M. Rudigier, J.-M. Régis, J. Jolie, C. Fransen and K. O. Zell, *Lifetime of the first 2^+ state in ^{172}W and ^{178}W* , Nucl. Phys. A 847, 89 (2010).

J.-M. Régis, Th. Materna, S. Christen, C. Bernards, N. Braun, G. Breuer, C. Fransen, S. Heinze, J. Jolie, T. Meersschant, G. Pascovici, M. Rudigier, L. Steinert, S. Thiel, N. Warr and K. O. Zell, *Sub-nanosecond lifetime measurements using the Double Orange Spectrometer at the Cologne 10 MV Tandem accelerator*, Nucl. Instrum. Methods Phys. Res. A 606, 466 (2009).

P. E. Garrett, W. D. Kulp, J. L. Wood, D. Bandyopadhyay, S. Christen, S. Choudry, A. Dewald, A. Fitzler, C. Fransen, K. Jessen, J. Jolie, A. Kloezer, P. Kudejova, A. Kumar, S. R. Lesher, A. Linnemann, A. Lisetskiy, D. Martin, M. Masur, M. T. McEllistrem, O. Möller, M. Mynk, J. N. Orce, P. Pejovic, T. Pissulla, J.-M. Régis, A. Schiller, D. Tonev and S. W. Yates, *Octupole and hexadecapole bands in ^{152}Sm* , J. Phys. G: Nucl. Part. Phys. 31 S1855 (2005).

Conference proceedings

V. Werner, N. Cooper, M. Bonett-Matiz, E. Williams, J.-M. Régis, M. Rudigier, T. Ahn, V. Anagnostatou, Z. Berant, M. Bunce, M. Elvers, A. Heinz, G. Ilie, J. Jolie, D. Radeck, D. Savran and M. Smith, *Excited State Lifetime Measurements in Rare Earth Nuclei with Fast Electronics*, INPC 2010, in press.

J.-M. Régis, G. Pascovici, Th. Materna, S. Christen, T. Meersschout, C. Bernards, C. Fransen, A. Dewald, N. Braun, S. Heinze, S. Thiel and J. Jolie, *Nuclear structure analysis using the Orange Spectrometer*, AIP CP 1090, 112 (2008).

P. E. Garrett, W. D. Kulp, J. L. Wood, J. M. Allmond, B. Bandyopadhyay, S. Christen, S. N. Choudry, D. Cline, D. Dashdorj, A. Dewald, A. Fitzler, C. Fransen, A. B. Hayes, H. Hua, K. Jessen, J. Jolie, A. Kloezer, P. Kudejova, A. Kumar, S. R. Lesher, A. Linnemann, A. Lisetskiy, D. Martin, M. Masur, M. T. McEllistrem, O. Möller, M. G. Mynk, C. J. McKay, J. N. Orce, P. Pejovic, T. Pissulla, J.-M. Régis, A. Schiller, R. Teng, D. Tonev, C. Y. Wu and S. W. Yates, *Investigation of ^{152}Sm by Complementary Reactions*, AIP CP 1090, 391 (2008).

Acknowledgments

The author would like to express his sincere gratitude to the director of the IKP and my PhD supervisor *Prof. Dr. Jan Jolie*. I am deeply grateful for his patience and trustfulness concerning the installation of the now best working Double Orange Spectrometer. Many thanks for the trust in periods where experiments have failed. Thank you very much for your absolute confidence in my work on the fast timing technique.

Special thanks are expressed to my assistant *Dipl. Phys. Mathias Rudigier* for proactive cooperation and his aid when installing and performing fast timing experiments at the IKP and elsewhere. Thank you very much for the code creating automatically the “shift files” with “tv” which simplifies the analysis.

Many thanks to all members of the IKP of the Cologne University. Thank you sincerely *Dr. Gheorghe Pascovici*, *Dr. Pavel Petkov*, *Dr. Andrey Blazhev* and especially *Dr. Nigel Warr* (“just call it: PRD”) for valuable discussions and for proofreading my articles and partly this PhD thesis. Thank you very much *Priv. Doz. Dr. Alfred Dewald* for suggesting to perform the experiment on ^{176}W at the HORUS cube spectrometer. Special thanks to *Dr. Christoph Fransen* for irreplaceable help on the adjustment of the IKP multi channel analysator and for cordial and successful cooperation at the IKP and the ILL. Many thanks to *Dr. Karl Oscar Zell* for the best target material I have ever received. Sincere thanks to *Prof. Dr. Peter von Brentano* for the fruitful criticism concerning my first attempt to describe the MSCD method. Many thanks to *Dipl. Phys. Désirée Radeck*, *Dipl. Phys. Sandra Christen*, *Dipl. Phys. Norbert Braun*, *Dipl. Phys. Tim Thomas*, *Dipl. Phys. Linus Bettermann*, *Dipl. Phys. Christian Bernards*, *Dipl. Phys. Tim Meerschaut*, *Dipl. Phys. Michael Albers*, *Dipl. Phys. Benedikt Birckenbach*, *Dipl. Phys. Wolfram Rother*, *Dipl. Phys. Gunnar Friesner*, *Dipl. Phys. Mathias Hackstein*, *Dipl. Phys. Kevin Moschner*, *Dipl. Phys. Thomas Pissulla*, *Michael Pfeiffer* and *Moritz Dannhoff* for very kind cooperation and assistance in the survey of nearly all the experiments performed at the IKP and the ILL. The author would like to thank the IKP group around *Prof. Dr. Andreas Zilges*, namely *Dr. Jens Hasper*, *Dr. Janis Endres*, *Dipl. Phys. Michael Elvers* and *Dipl. Phys. Marc Büssing* for very kind and active cooperation in the experiment on ^{176}W performed at the HORUS cube spectrometer. Special thanks to the group around *Dipl. Ing. Stefan Thiel* of the IKP fine mechanics workshop and to the group around *Dipl. Ing. Christoph Görden* of the IKP electronics workshop for the excellent installation of infrastructure facilities for the Double Orange Spectrometer setup. Also many thanks to the IKP Tandem accelerator operators *Dipl. Ing. Lothar Steinert*, *Uwe Werner* and *Otto Rudolf* for providing the best beam conditions for more than a dozen of experiments.

I would like to thank the leader of the “Ultra Fast Timing Collaboration” *Dr. Henryk Mach* for valuable discussions on the fast timing technique. You were the first scientist who recognized and appreciated the results of my work on fast timing with the Orange spectrometers and especially with the $\text{LaBr}_3(\text{Ce})$ detectors. This was important for my mind, because extremely few people have your knowledge on fast timing with scintillators. Thank you very much for making me sensitive to the definition of the “total error”.

Special thanks to the group “LOHENGRIN” (PN1) at the Institut Laue Langevin (ILL) in Grenoble, France. Thank you very much *Dr. Thomas Matera* for many experimental experiences at the IKP and at the LOHENGRIN spectrometer of the ILL for more than 5 years now. Many thanks also to the leader *Dr. Herbert Faust* and to *Dr. Ulli Köster* for generative cooperation and collaboration with the IKP. I would like to thank *Dr. Gary Simpson* from the LSPC of Grenoble also for perfect cooperation at LOHENGRIN and for valuable discussions. Thank you all very much for recognition of my work on fast timing.

I would like to thank the group around *Ass. Prof. Volker Werner* of the Yale University WNSL at New-Haven, Connecticut, United States of America. Thank you very much also *Dr. Elisabeth Williams*, *Nathan Cooper* and *Mario Bonetti-Matiz* for pleasant 2 weeks of scientific and experimental collaboration which was exceptionally successful and introduced the $\text{LaBr}_3(\text{Ce})$ scintillators in the United States.

Sincere thanks to the “Balkan Collaboration” of the NIPNE in Bucarest, Romania and the INRNE in Sofia, Bulgaria. Special thanks to *Dr. Nicu Mărginean*, *Dr. Dan Ghita* and *Dr. Stefan Lalkovski* for very nice times at different places of our small world.

Many thanks to the group around *Dr. Dave Cullen* for the very nice experience of 24 hours of daylight at the Department of Physics of the University of Jyväskylä, Finland. I have exquisitely enjoyed the stay and the finnish fish dishes.

Thank you *Dr. Luis Fraile* for the nice experience at the ISOLDE facility of the CERN in Geneva, Switzerland. Maybe, in future we will work together many times. I am ready and looking forward to an ongoing kind and effective cooperation.

Merci infiniment pour la femme qui m’a mise au monde des humains *Madame Myriam Maassen*. Merci beaucoup pour ton soutien sincère et pour ton aide financière dans les temps où je n’avais pas assez d’argent pour financer les études.

Vielen Dank auch an den Lebensgefährten meiner Mutter *Herrn Gerd Ranke* für das liebe und äußerst gastfreundliche Empfangen bei meinen seltenen Besuchen. Auch dir danke ich sehr für die aufrichtige moralische Unterstützung während meines Studiums.

Erklärung

Ich versichere, daß ich die von mir vorgelegte Dissertation selbständig angefertigt, die benutzten Quellen und Hilfsmittel vollständig angegeben und die Stellen der Arbeit - einschließlich Tabellen, Karten und Abbildungen - , die anderen Werken im Wortlaut oder dem Sinn nach entnommen sind, in jedem Einzelfall als Entlehnung kenntlich gemacht habe; daß die Dissertation noch keiner anderen Fakultät oder Universität zur Prüfung vorgelegen hat; daß sie - abgesehen von unten angegebenen Teilpublikationen - noch nicht veröffentlicht worden ist, sowie, daß ich eine solche Veröffentlichung vor dem Abschluß des Promotionsverfahrens nicht vornehmen werde. Die Bestimmungen dieser Promotionsordnung sind mir bekannt. Die von mir vorgelegte Dissertation ist von Professor Dr. Jan Jolie betreut worden.

Jean-Marc Régis

Teilpublikationen

Teile der Kapitel 2, 3 und 5 wurden veröffentlicht in:

V. Werner, N. Cooper, M. Bonett-Matiz, E. Williams, J.-M. Régis, M. Rudigier, T. Ahn, V. Anagnostatou, Z. Berant, M. Bunce, M. Elvers, A. Heinz, G. Ilie, J. Jolie, D. Radeck, D. Savran and M. Smith, *Excited State Lifetime Measurements in Rare Earth Nuclei with Fast Electronics*, INPC 2010, in press.

J.-M. Régis, Th. Materna, G. Pascovici, S. Christen, A. Dewald, C. Fransen, J. Jolie, P. Petkov and K. O. Zell, *Improvement of the intrinsic time resolving power of the Cologne iron-free Orange type electron spectrometers*, Rev. Sci. Instrum. 81, 113505 (2010).

J.-M. Régis, G. Pascovici, J. Jolie and M. Rudigier, *The mirror symmetric centroid difference method for picosecond lifetime measurements via γ - γ coincidences using very fast $\text{LaBr}_3(\text{Ce})$ scintillator detectors*, Nucl. Instrum. Methods Phys. Res. A 622, 81 (2010).

M. Rudigier, J.-M. Régis, J. Jolie, C. Fransen and K. O. Zell, *Lifetime of the first 2^+ state in ^{172}W and ^{178}W* , Nucl. Phys. A 847, 89 (2010).

Lebenslauf

Familienname Régis
Vorname Jean-Marc
Geburtsdatum 19.02.1970
Staatsangehörigkeit Frankreich
Eltern Myriam Maassen und Michel Régis

Schul Ausbildung:

Grundschule: 1977-1981 Eupen, Belgien
Realschule: 1981-1985 Erftstadt
Hauptschule: 1985-1987 Weilerswist
Mittlere Reife: 07.1987

Pflichtwehrdienst: 08.1988-07.1990, Französische Streitkräfte in Deutschland

Berufsausbildung:

Hotelfachmann: 09.1990-08.1993, Rheinhof Dreesen in Bonn Bad Godesberg
Berufstätigkeit: 1993-1997 in Köln

Zweiter Bildungsweg:

Kolleg: 1997-2000 Köln-Kolleg, Köln
Abitur: 05.2000

Hochschulstudium:

Imatrikulation: WS 2000/01, Studium an der Universität zu Köln, Studienfach Physik Diplom
Diplomarbeit: 02.2007, Thema: "Feasibility study of lifetime measurements using the Double Orange Spectrometer"

Arbeitsverhältnisse am Institut für Kernphysik der Universität zu Köln:

10.2001-02.2005 Studentische Aushilfskraft
03.2005-02.2007 Studentische Hilfskraft
seit 04.2007 Wissenschaftlicher Mitarbeiter